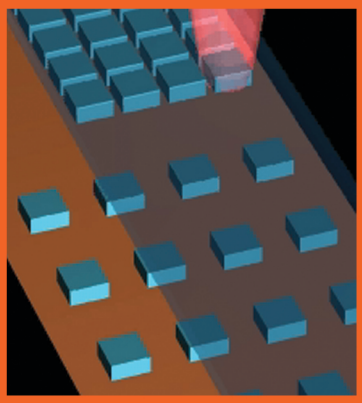
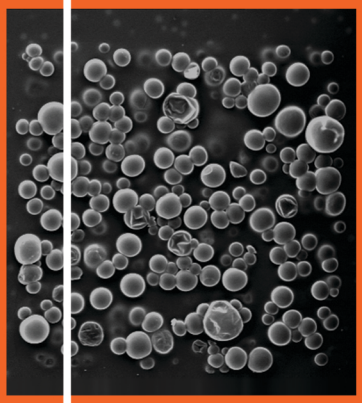
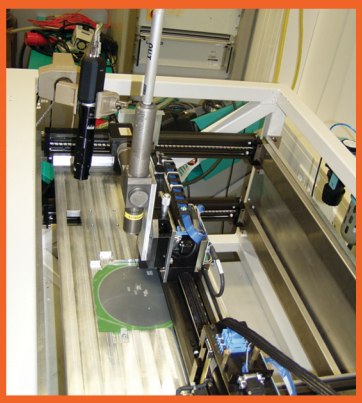

# LASER DIE TRANSFER:

## Laser-induced transfer of microcomponents

Natallia Karlitskaya

# LASER DIE TRANSFER:

# LASER-INDUCED TRANSFER OF MICROCOMPONENTS

The research was performed at the Chair of Applied Laser Technology of the faculty of Engineering Technology of the University Twente and was financially supported by the Innovation Oriented Research Program (Innovatiegerichte Onderzoeksprogramma), Dutch Ministry of Economic Affairs SenterNovem Agency.

Ph.D. Thesis, Laser Die Transfer: laser-induced transfer of microcomponents by Natallia Karlitskaya, University of Twente, Enschede, The Netherlands, 2011. With ref.
ISBN:978-90-365-3260-0


Printed by Drukkerij Gildeprint, Enschede, The Netherlands.

# LASER DIE TRANSFER: LASER-INDUCED TRANSFER OF MICROCOMPONENTS

**DISSERTATION**

to obtain
the doctor's degree at the University of Twente,
on the authority of the rector magnificus,
prof. dr. H. Brinksma,
on account of the decision of the graduation committee,
to be publicly defended
on Friday, 16th December 2011 at 14.45

by

**Natallia Karlitskaya**

born on 24.12.1975

in Orscha, Belarus

This dissertation has been approved by,
Promotor: Prof. dr. ir. J. Meijer
Assistant Promotor: Prof. dr. ir. D.F. De Lange

# Preface

The work presented in this thesis was conducted at Philips Applied Technologies (Apptech) under supervision of prof. dr. ir. J. Meijer, the University of Twente, Faculty of Engineering Technology, Chair of Applied Laser Technology. The "Laser Die Transfer" project was sponsored by the Innovatiegericht Onderzoeksprogramma (IOP), which was initiated by the Dutch Department of Social and Economic Affairs. Goal of this project was to develop a new contact-free technique for high speed assembly of miniature electronic components and to build a prototype which demonstrates the process capabilities.

The process is protected by a patent "Method suitable for transferring a component supported by a carrier to a desired position on a substrate, and a device designed for this", published as US2006081572(A1), 2006-04-20.

## List of publications

Parts of the work described in this thesis were published in:

- N. S. Karlitskaya, D. F. de Lange, R. Sanders, J. Meijer (2004) *Study of laser die release by Q-switched Nd:YAG laser pulses.* Proc. SPIE Vol. 5448, p. 935-943, High-Power Laser Ablation V; Claude R. Phipps; Ed.

- N.S. Karlitskaya, J. Meijer, D.F. de Lange, R. Sanders, (2005) *Laser-induced transfer process for die assembly*, Proc. The third International WLT-conference on Laser in Manufacturing, Ed. E. Beyer, F. Dausinger, A. Ostendorf, A. Otto (ISBN 3-00-016402-2) Munich, Germany, AT-Fachverlag GmbH, Stuttgart pp. 669-672

- N. S. Karlitskaya, J. Meijer, D. F. de Lange, H. Kettelarij (2006) *Laser propulsion of microelectronic components: releasing mechanism investigation.* Proc. SPIE Vol. 6261, 62612P High-Power Laser Ablation VI, Claude R. Phipps; Ed.

- N. S. Karlitskaya, J. Meijer, D. F. de Lange, H. Kettelarij (2006) *Laser-assisted micro-components assembly: releasing control and placement accuracy improvement investigation* Online Proc. of the 4th International Congress of Laser Advanced Material Processing (LAMP), Kyoto, Japan, all publications are represented on the website http://www.jlps.gr.jp/en/proc/lamp/06/

# Acknowledgements

First of all I would like to express my gratitude to professor Johan Meijer, my supervisor. Thank you, Johan, for guiding me through all these years, for teaching me how to work systematically and for challenging and supporting me. I have learned more from you than from anyone else. I'd like to thank professor Bert Huis in 't Veld and dr. Gert-Willem Römer for motivating me to finish the work and for giving me the opportunity to establish the PhD thesis. I would like to thank professor Frits de Lange for his help in FEMLAB modeling. Frits, thank you. I really appreciate all your support, all your suggestions and endless e-mail discussions. Without you the modeling chapter would not have been finished.

I would like to thank former AppTech colleagues, especially Willem Hoving, Rene Sanders and Henk Kettelarij for valuable comments, productive discussions, interesting ideas and hands-on assistance with set-ups. I would like to thank Wessel Wesseling for his interest and active contribution to the prototype design and implementation. Many thanks to IOP committee members for giving me directions and coming to meet every half a year to discuss the progress.

I want to thank all students who were involved in the project over the years: to Kyriakos D. Kyrkis who was involved in ablation experiments, to Alexander Egenraam who built the accurate targeting system and Walter Loch who made a mechanical design of the prototype and developed the future Laser Direct Die Feeder.

I would like to thank my friends, just because they were there for me: Julia Nazarenko, Alena Kryvinchanka, Anastasia Andreadaki and Svetlana Sinitsuna.

I thank my husband Alexey, who has supported me all these years, who was busy with the kids when I was finishing my thesis who believed in me. I would also like to thank my mum Tatyana and my mother in law Zinaida for their support and love.

# Nomenclature

## Symbols

| *Symbol* | *Unit* | *Description* |
|---|---|---|
| $b_{x,y}$ | [rad] | Amplitude of the grating phase variation |
| $c$ | [mol/m$^3$] | Gas concentration |
| $c_0$ | [mol/m$^3$] | Initial gas concentration |
| $C_cal$ | [J/mol] | Amount of heat generated for the production of one unit of gas |
| $c_p$ | [J/(kg K)] | Specific heat at constant pressure |
| $D$ | [m] | Total displacement |
| $Di$ | [m$^2$/s] | Diffusion coefficient |
| $E_G$ | [J] | Band-gap energy |
| $E_{in}$ | [J] | Incident energy |
| $E_{krotat}$ | [J] | Kinetic energy of rotation |
| $E_{thr}$ | [J] | Releasing threshold energy |
| $f$ | [mm] | Focal length of optical element |
| $F$ | [N] | Force |
| $G_f$ | - | Gas fraction |
| $G_n$ | - | New gas fraction |
| $h$ | [m$^2$kg/s] | Plank's constant $6 \cdot 10^{-34}$ |
| $h$ | [m] | Thickness |
| $H(T)$ | [J/kg] | Enthalpy as function of the temperature |
| $I$ | [J s/m$^2$] | Intensity |
| $I_0$ | [J s/m$^2$] | Incident intensity |
| $J$ | [kg m$^2$] | Rotation inertia |
| $K$ | [W/(m K)] | Thermal conductivity |
| $k_B$ | [J/K] | Boltzmann's constant, $(1.38 \cdot 10^{-23})$ |
| $l$ | [m] | Length |
| $l_{alpha}$ | [m] | Optical absorbtion length |
| $L_v$ | [J/kg] | latent heat for vaporisation |
| $M$ | [N m] | Moment of rotation |
| $m$ | [kg] | Mass |
| $p_a$ | [Pa] | Atmospheric pressure |
| $p$ | [Pa] | Pressure |
| $p_r$ | [Pa] | Recoil pressure |
| $q$ | [W/m$^3$] | Volume heat source |
| $q_v$ | [W/m$^2$] | Evaporation heat flux |
| $R$ | - | Reflectivity |

(continued from previous page)

| *Symbol* | *Unit* | *Description* |
|---|---|---|
| $r_c$ | [mol/m$^3$ s] | Proportional reaction coefficient |
| $R_c$ | [mol K/m$^3$ s] | General reaction coefficient |
| $r_e$ | - | Exponential reaction coefficient |
| $R_p$ | [mol/m$^3$ s] | Production rate |
| $R_u$ | [J/(mol K)] | Universal gas constant 8.314 |
| $T$ | [K] | Temperature |
| $t$ | [s] | Time |
| $T_b$ | [K] | Boiling temperature at normal pressure |
| $V$ | [m$^3$] | Volume |
| $x$ | [m] | Coordinate |
| $Y$ | [Pa] | Young's modulus |
| $y$ | [m] | Coordinate |

# Greek Symbols

| *Symbol* | *Unit* | *Description* |
|---|---|---|
| $\alpha$ | [1/m] | Linear optical absorbtion coefficient |
| $\alpha_{FCA}$ | [1/m] | Free-carrier absorbtion coefficient |
| $\alpha_L$ | [1/m] | Lattice absorbtion coefficient |
| $\delta$ | [m] | Optical penetration depth |
| $\eta$ | - | Fraction of the energy transformation |
| $\theta$ | [rad] | Angle of rotation |
| $\lambda$ | [m] | Wavelength of laser source |
| $\nu$ | [J/$cm^2$] | Fluence |
| $\rho$ | [kg/$m^3$] | Mass density |
| $\tau$ | [sec] | Pulse duration |
| $\upsilon$ | [m/sec] | Velocity |
| $\upsilon_f$ | - | Final velocity |
| $\varepsilon$ | [m/sec] | Local strain |
| $\phi_e$ | [kg/sec] | Evaporated mass flux |
| $\omega$ | [deg/sec] | Angular velocity |

# Acronyms and Abbreviations

| | |
|---|---|
| CCD | **C**harged **C**oupled **D**evice |
| CW | **C**ontinuous **W**ave |
| DDF | **D**irect **D**ie **F**eeder |
| DOE | **D**iffractive **O**ptical **E**lement |
| FCA | **F**ree **C**arrier **A**bsorbtion |
| FEM | **F**inite **E**lement **M**ethod |
| FFT | **F**ast **F**ourier **T**ransform |
| FWHM | **F**ull **W**idth at **H**alf **M**aximum |
| IC | **I**ntegrated **C**ircuit |
| IR | **I**nfra-**R**ed |
| LDT | **L**aser **D**ie **T**ransfer |
| LED | **L**ight- **E**mitting **D**iode |
| LIFT | **L**aser **I**nduced **F**orward **T**ransfer |
| MAPLE-DW | **M**atrix **A**ssisted **P**ulsed **L**aser **E**vaporation **D**irect **W**rite |
| Nd:YAG | **N**eodymium-doped **Y**ttrium **A**luminium **G**arnet |
| PC | **P**ersonal **C**omputer |
| PCB | **P**rinted **C**ircuit **B**oard |
| PET | **P**oly**E**thylene **T**erephthalate |
| PICA | **P**arallel **I**ntegrated **C**hip**A**ssembly |
| PMMA | **P**oly(methyl methacrylate) |
| PLD | **P**ulsed **L**aser **D**eposition |
| PVC | **P**oly -**V**inil- **C**hloride |
| RFID | **R**adio **F**requency **I**dentification |
| SEM | **S**canning **E**lectron **M**icroscope |
| SMT | **S**urface **M**ount **T**echnology |
| SWT | **S**emiconductor **W**afer processing **T**ape |
| TTL | **T**ransistor **T**ransistor **L**ogic |
| UV | **U**ltra**V**iolet |

# Contents

**Nomenclature** **vii**

**1 Introduction** **1**
1.1 Micro-components Assembly in the Modern World . . . . . 1
1.2 The Principles of Laser-induced Die Transfer . . . . . 4
1.3 Problem definition . . . . . 6
1.4 Overview . . . . . 6

**2 The State-of-the-art in the Micro-Component Assembly Processes** **9**
2.1 General Requirements for Micro-Component Assembly . . . . . 9
2.2 New Technologies in Microassembly . . . . . 11
2.3 Stochastic Assembly . . . . . 12
2.3.1 Fluidic Self-Assembly . . . . . 12
2.3.2 Dry Self-Assembly . . . . . 15
2.4 New Developments Based on Conventional Equipment . . . . . 18
2.4.1 PICA: Parallel Integrated Chip Assembly . . . . . 18
2.4.2 Ultrathin Silicon Assembly . . . . . 18
2.5 Laser Die Transfer: Assembly requirements . . . . . 19
2.6 Summary . . . . . 20

**3 Laser-induced Transfer Methods** **23**
3.1 Pulsed Laser Deposition . . . . . 23
3.2 Laser Induced Forward Transfer Process . . . . . 23
3.3 Matrix Assisted Pulsed Laser Evaporation (MAPLE) and MAPLE Direct Write . . . . . 26
3.4 Laser Propulsion . . . . . 28
3.4.1 Laser micro-propulsion . . . . . 29
3.5 Summary . . . . . 30

**4 Ablation-induced release experiments** **33**
4.1 Introduction . . . . . 33
4.2 Experimental equipment and set-up . . . . . 33
4.2.1 The monitoring system . . . . . 34
4.2.2 The target . . . . . 35
4.2.3 The laser source . . . . . 38
4.3 Study of the gold-coated crystalline silicon dies detachment from the Nitto SWT blue tape . . . . . 41

4.4 Study of die detachment from the Nitto SWT carrier tape . . . . . 45
4.5 Discussion . . . . . 49

**5 Thermal-induced release experiments 51**
5.1 Introduction . . . . . 51
5.2 Experimental equipment and set-up for thermal-induced release using 1064 nm wavelength . . . . . 51
5.3 Study of the thermal-induced release crystalline silicon dies from the Revalpha tape using 1064 nm wavelength . . . . . 55
5.3.1 Placement accuracy investigation . . . . . 58
5.4 Experimental equipment and set-up for thermal-induced release experiments using 532 nm wavelength . . . . . 66
5.5 Study of the thermal-induced release crystalline silicon dies from Revalpha tape using 532 nm wavelength . . . . . 67
5.6 Discussion . . . . . 69

**6 Modeling 71**
6.1 Introduction . . . . . 71
6.2 Radiation . . . . . 71
6.2.1 Absorption mechanisms in silicon . . . . . 71
6.2.2 Implementation in the simulation model . . . . . 73
6.3 Heat transfer . . . . . 74
6.3.1 Silicon evaporation . . . . . 75
6.3.2 Gas formation in the glue layer . . . . . 76
6.4 Release dynamics . . . . . 78
6.5 Model implementation . . . . . 82
6.6 Simulation results . . . . . 83
6.6.1 Simulation results with the ablative release model . . . . . 83
6.6.2 Simulation results with a thermal release model . . . . . 90

**7 Diffractive Optical Element 113**
7.1 Introduction . . . . . 113
7.2 Beam shaping . . . . . 113
7.3 Discussion . . . . . 115

**8 Demonstrator 117**
8.1 Introduction . . . . . 117
8.2 Surface Mount Technology and Direct Die Feeding . . . . . 118
8.3 Prototype 'Laser Die Transfer' . . . . . 119
8.3.1 Process changes for LDT . . . . . 119
8.3.2 Description of the demonstrator . . . . . 120
8.4 Results and conclusions . . . . . 125
8.5 Recommendations and future development . . . . . 126

**9 Conclusions 129**

**Summary 131**

**Samenvatting 133**

# Chapter 1

# Introduction

## 1.1 Micro-components Assembly in the Modern World

As we step into the 21st century, electronic devices are everywhere in our lives. From domestic consumer products to military and space devices. The current trend in the electronics industry is to make products more compact while increasing their functionality.

Semiconductors are the basic building blocks used to create an increasing variety of electronic products and systems. The manufacturing process involves two distinct phases: wafer processing (commonly referred to as "front-end") and assembly/test operations (including die attach bonding, packaging, plating and testing functions, commonly referred to as "back-end"). Wafer processing involves thousands of complex steps applied to a silicon wafer to form millions of circuits on the wafer comprising a large number of chips. In the semiconductor assembly process the individual chips or a "die" are separated from the wafer first and then each die is attached to a plated metal leadframe or a multilayer substrate. In first-level packaging, the chip electrically communicates with the packaging substrate through input/output (I/O) connections, which are commonly performed by one of the two common technologies, wire bonding or flip chip bonding, see Figure 1.1.

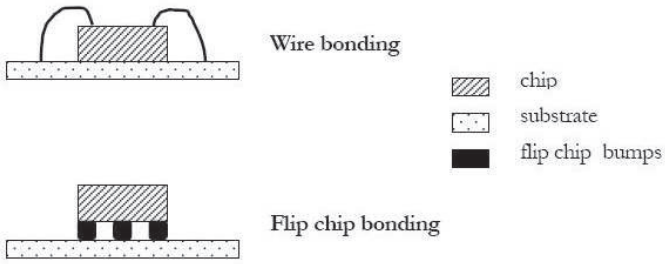


Figure 1.1: I/O connection structures.

In the wire bonding process, a fine metal wire (gold or aluminum, typically 20-25 $\mu$m in diameter) connects a chip pad to a corresponding substrate pad. The wire is connected to the pads at each end by the bonding process. This process is time-consuming, since each individual connection between a chip and a board is made sequentially. For chips containing many I/O's, the bonding time for each chip can become unacceptably long. In flip chip bonding, the active side of the chip is face-down and is connected to bonding pads on the packaging substrate via conductive

bumps. The bonds at numerous bump sites are achieved simultaneously, which saves a considerable amount of time for chips with many I/O's. The main advantage of this technique is that chip mounting and the creation of the electrical connection are done simultaneously within a single step.

In both wire-bonding and flip chip placement, the first step is to release the component from the carrier. The carrier is a polymer tape (or foil) on which the wafer with the components were placed prior to the dicing process, see Figure 1.2, a). Because these tapes are used to support the components during dicing, they are referred to as "dicing tapes". The die is removed from the dicing tape through the use of single or multiple ejector pins or pushing needles, which push up from under the tape and release the die by applying pressure to the backside. The flip unit (vacuum nozzle #1 in the Figure 1.2: b)) picks up the ejected die and flips it 180°: c). Afterwards, the pick-and-place unit (vacuum nozzle #2) picks up the flipped die, d) aligns it and places it into the substrate with deposited adhesive material, e). In the final step of the bonding process, heat and pressure are applied to bond the die on the substrate.

The speed of the flip-chip pick-and-place process is typically 2500 to 8000 chips (depending on chip size and required mounting accuracy) per hour (max. 2 chips per second) for most applications. Increasing this speed is very important, because the cost per attached die has a major impact on the total cost.

In the semiconductor industry and among manufacturers of integrated circuits (IC's) and other semiconductor devices there is a trend to create and process components that are increasingly small. Existing technologies, however, are a limiting factor in this trend toward small dies; the common pick-and-place machines cannot handle dies smaller than 1 mm, the smallest die dimension that can be handled by pick-and-place equipment currently is 170 $\mu$m. One of the limitations is that, for components of less than 100 $\mu$m, adhesive capillary forces dominate gravitational forces. This makes it difficult to release the components from the end-effector of a robotic manipulator [Fea95]. The size of many existing electronic systems could be reduced by several orders of magnitudes if micro-components could be assembled and interconnected effectively.

Another important trend is towards thin and flexible packages, driven by different industrial applications. The motivation to use ultra-thin silicon comes from the following advantages:

- Thin chips have lower electrical resistance to substrate - lower power dissipation;
- Thin chips have lower thermal resistance to substrate;
- A smaller package;
- Advantages for hand-held / battery-powered devices / thin smart cards and flexible smart labels;
- Mechanically flexible silicon chips (if circuit wafers are thinned down to 30 $\mu$m) are ideally suited for cost-effective assembly on flexible substrates.

Therefore, the availability of equipment that is able to work with ultra-thin dies is an important issue for the broad industrial use of silicon. The minimum die thickness that can be handled today by conventional equipment is about 100 $\mu$m.

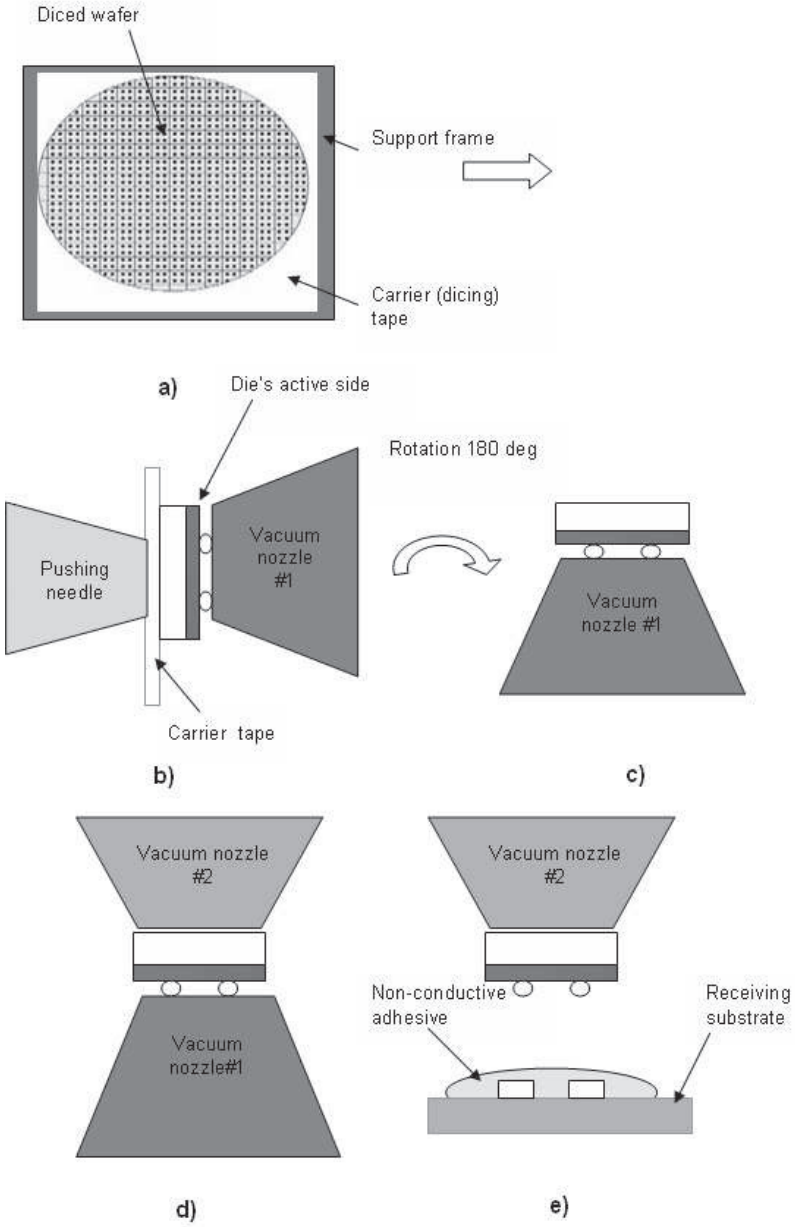


Figure 1.2: Illustration of the flip chip process.

At a chip thickness of approximately 50 $\mu$m, the eject process normally applied to die release is not feasible anymore. Generally, the carrier tape is penetrated by one or more needles, the die is lifted and is taken up by a vacuum tool. Using thin IC's, of 50 $\mu$m or less, this would lead to mechanical damage or breaking of the die by the needles. Furthermore, one has to keep in mind that such thin chips are flexible. Therefore, peeling-off of a chip from the carrier tape, which normally starts at the corners of the chip, will not occur.

In summary, the need for new advanced solutions to improve the process of die transferring (higher speed, handling small and ultra-thin silicon dies) is driven by the need for portable electronics, heat dissipation, flexible electronic assemblies that can improve existing products, and totally new applications. Finding alternative techniques and improving the existing ones is one of the main issues for the semiconductor industry nowadays. General requirements of the process and new developments that have recently emerged in microelectronics assembly will be described in Chapter 2.

## 1.2 The Principles of Laser-induced Die Transfer

Since about 1998, laser-based processes have been investigated as a tool to release the materials from the carriers and propel them to the receiving substrate [Hol98], [Gre04], [Zha04], [Mat06]. Ideas and principles of the release and propulsion using laser irradiation can be divided based on the propulsion material used:

- The dies are mounted on a transparent carrier via a "sacrificial layer" between the carrier and the die. Using short laser pulses, this sacrificial layer is ablated and it generates a propulsion force to release the die from its carrier, and propel it towards the receiving substrate.
- A pulsed laser beam impinges on a die affixed to an optically transparent carrier. Laser absorption occurs in a thin layer of the die at this interface, rapidly causing the material (and the carrier material near the interface as well) to vaporize. Gas expansion accelerates the die off the carrier at high velocity.

These processes have the advantage of very high transfer speeds. Furthermore, the fact that laser assisted transfer is a contactless process opens up the route for the transfer of ultra-thin and small components. An overview of the laser-induced transfer techniques will be presented in Chapter 3.

Laser-induced die transfer is an innovative technique that provides high speed (up to 100 dies per second) assembly of micro-dies. The considered structure is a sample from the semiconductor wafer that consists of a carrier polymer tape and a diced silicon wafer attached to this tape via a glue layer. The first step of the assembly process is the release of the die from its carrier.

The laser beam irradiates the interface between the die and the glue. Then, the targeted die becomes detached, as shown in Figure 1.3. The driving force for the die is gas formation and, consequently, the pressure build-up between the glue layer and the die due to the rise in temperature induced by the absorbed laser energy.

The developed approaches of the die-release process are based on the kind of carrier used and the laser parameters. Two distinct processes are categorized here:

1. The dies are placed on a pressure-sensitive adhesive tape and the interface is irradiated by a laser beam with high power densities.

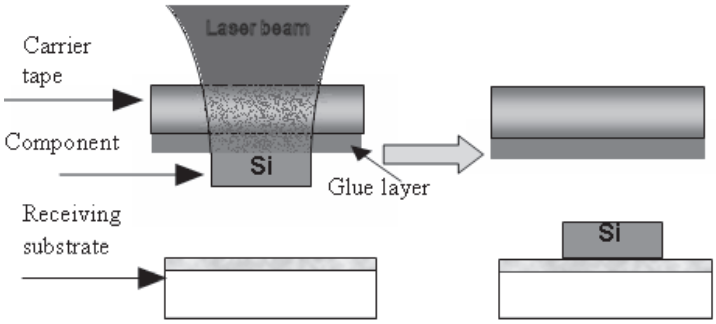


Figure 1.3: Basic laser-induced transfer process.

2. Using a carrier that loses its adhesive properties upon heating above a threshold temperature, the interface is heated at low laser densities.

The chosen transfer process will depend on how smooth, stable and controllable the component's release is. The difference between these approaches is based on the optical properties of the silicon, characteristics of the carrier tape and phenomena that take place in the whole system. The similarity between these processes is that the carrier tape is transparent with regard to the laser irradiation; light absorption takes place in the silicon component itself. These two different approaches of the release and propulsion processes are referred to here as ablation-induced release and thermal-induced release.

In order to understand phenomena associated with laser-induced release, it is necessary to accurately know the optical properties of the materials involved, because these properties determine how the laser radiation is absorbed by the material. This is true for all materials, but it is particularly significant for indirect-gap semiconductors such as silicon, the optical properties of which strongly change with temperature over an extended range of wavelengths. Therefore, the theoretical explanation of the laser material interactions and silicon absorption mechanisms are presented in Chapter 6.

**Ablation-induced release**

In the case of ablation-induced release, the detachment of the micro-dies from the adhesive carrier is caused by the ablation of the carrier-die interface. The ablation process takes place in a confined geometry, i.e. the gas generated by the decomposition of the interface is confined in volume by the carrier and the moving die. Thus, the gas does not expand freely, and builds up pressure at the interface. This also means that an extra complexity enters the analysis, for the theoretical modeling of the process.

Ablation causes high release velocities of the die, due to the high pressure. The process is investigated in detail in Chapter 4 and the results are assessed based on the application. The theoretical explanation of the process and process simulation are represented in Chapter 6.

**Thermal-induced release**

With thermal-induced release, the properties of the carrier act in such a way that when a temperature threshold is reached upon heating, gas bubbles which are present in the carrier material start to expand, push and accelerate the die. Eventually the die velocity become high enough to overcome the carrier adhesive force which result in the die release from the carrier with some initial velocity.

With this approach the release takes place under lower irradiation and the die is released at lower speed. This process avoids the undesirable effects of high power density laser irradiation. Details are presented and discussed in Chapter 5. The simulation of the process is represented in Chapter 6.

## 1.3 Problem definition

The laser die transfer technique has significant potential for the high speed assembly of micro-sized and ultra-thin components.

The aim of this thesis is to investigate experimentally and theoretically the laser-induced release and placement processes involved.

The main steps to achieve this goal are:

- Study of laser interactions with polymers and silicon;
- Study of the dynamics of die release by means of laser irradiation using a high speed camera;
- Investigation of the placement accuracy;
- Finding the factors responsible for the placement accuracy and optimization of the assembly;
- Designing, building and testing a demonstrator for the Laser Die Transfer process.

IOP committee members including the Dutch organizations Philips, Besi, Assembléon and TNO have defined the industrial requirements for the Laser Die Transfer process:

- Placement accuracy should be 35 $\mu$m for 300 $\mu$m sized square dies (no specification on the yield was defined at that stage; however, the results of the experimentally achieved yield will be presented);
- Temperature of the active layer of the IC should not exceed 700 K;
- The process should be faster than 10 dies per second.

## 1.4 Overview

This thesis consists of nine chapters (including this introduction).

Chapter 2 is dedicated to the general requirements for assembly and new techniques in the area of mass assembly of micro and ultra thin dies.

A literature overview of the laser-induced material transfer procewsses is presented in Chapter 3. This Chapter summarizes innovative techniques which use laser light to transfer material from its support and deposit it into a suitable substrate.

The ablation-induced release approach of the laser die transfer process is described in Chapter 4. The device, materials and sample preparation procedures used in the investigation are presented, including the design and implementation of the experimental set-up and experiment flow description.

The second approach, thermal-induced release is presented in Chapter 5. In this Chapter, the experimental set-up is described in detail and the release process is investigated for various laser sources. The assembly results and statistical analysis of the placement are investigated.

In Chapter 6 a theoretical description of the ablative and thermal release processes is represented. This is followed by a temperature distribution calculations and the component's release dynamic simulations using a Finite Element Model.

As the spatial profile of the laser beam has been found to play an important role in the die's placement accuracy improvement, a Diffractive Optical Element (DOE) is considered as a solution for equal illumination of the die by the laser beam. The design of the DOE as a beam homogenizer is presented in Chapter 7.

The Laser Die Transfer process could be applied to various assembly processes. These possible applications are described in Chapter 8. One of the applications, the Laser Direct Die Feeder demonstrator, is developed and tested in practice. This demonstrator shows excellent results in the release and transfer of thin dies from the tape carrier to the position where the die can be picked up and further used in an existing Surface Mount Technology machine. This demonstrator was built in collaboration with Assembléon B.V.

Chapter 9 contains general conclusions derived from the results of the previous chapters and recommendations.

# Chapter 2

# The State-of-the-art in the Micro-Component Assembly Processes

## 2.1 General Requirements for Micro-Component Assembly

Assembly is defined as the "fitting together of manufactured parts into a complete machine, structure, or unit of a machine", [Log91].

Robotic applications have been expanding since the introduction of robots. The identified parameters relating to a robot's positional performance are accuracy, repeatability, and resolution. Resolution is defined as the smallest incremental movement that the robot can physically produce. Repeatability is a measure of the ability of the robot to move back to the same position and orientation over and over again from the same initial position. Accuracy is defined as the ability of the robot to precisely move to a desired position in 3-D space from any position within this space. These concepts are shown graphically in Figure 2.1. Each of these characteristics is

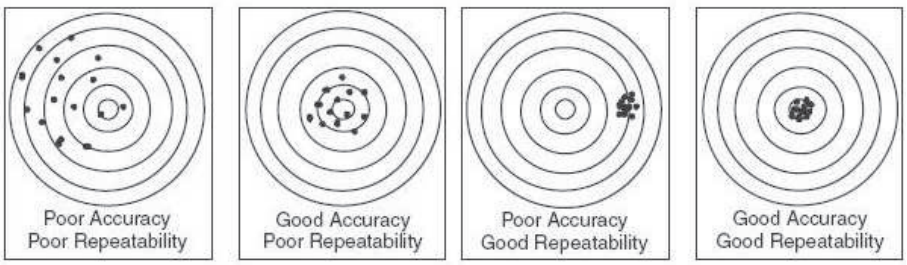


Figure 2.1: Accuracy versus repeatability.

affected by many factors that include, but are not limited to, friction, temperature, loading, and manufacturing tolerances. Of the three robot characteristics, high accuracy is the most difficult to accomplish. Different positioning principles, in practice, show significantly different capabilities in combination with their speed and accuracy: machines give high throughput compromising accuracy or high accuracy compromising throughput.

The most advanced pick-and-place systems today are specified by an x, y accuracy of $\pm 20$ $\mu$m based on a 4 Sigma quality level. The fundamental disadvantage of these systems is the limited placement speed, which is usually less than 8000 components per hour ($\sim$ 2 components per second).

High-speed placement with smaller and less demanding components (in terms of placement accuracy) is performed by the revolver (shooter) head. The placement principle is called "collect and pick-and-place". The most advanced version of such a collect-and-place system can perform the high-speed placement of 30 000 components per hour (8 components per second) with a placement accuracy of 60-100 $\mu$m based on 4 Sigma.

The typical accuracy for existing applications and the speed that is achievable for this process is represented in Figure 2.2. For future production the predicted trend is sacrificing accuracy for a higher throughput. High throughput is the main factor to achieve cost reduction in application areas such as RFID and LEDs assembly. Another

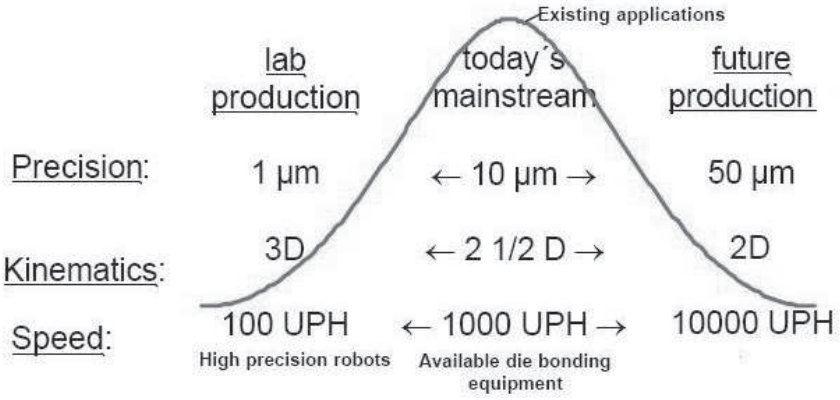


Figure 2.2: An overview of the precision and speed for existing applications and trends for future mass assembly, [Ern03].

key criterion to be considered is flexibility. Flexibility translates into the ability to handle a complete package-form range. The minimum size of components that could be handled with conventional equipment is 250 $\mu$m and thickness is 100 $\mu$m. With the tendency towards smaller and thinner components, conventional pick-and-place equipment becomes a limiting factor in component design.

Placement modules should also accept all component supply formats. The majority of the pick-and-place and collect-and-place machines are fed with matrix trays (waffle packs) or embossed tapes. This is a costly, non-value added process involving intermediate die transfer from the wafer tape on which components were separated, into a pocketed tape, surf-tape, or waffle packs prior to the placement. One of the reasons for this additional step are the difficulties brought about by direct feeding of the wafer: mechanical damage of the components by pushing needles and low speed. This intermediate process can be eliminated by using the fast and contact-free Laser Die Transfer technique.

Although a high precision, flexible microassembly station capable of handling small and thin components is needed, it is not available on the market right now.

### Placement Accuracy

The required placement accuracy is determined by a combination of the bond pad pitch and the substrate manufacturing technology. Consider, as an example, a die of 150 $\mu$m squared. The bond pads are 25 $\mu$m in diameter, their pitch is 125 $\mu$m and the component will be placed on two tracks with a pitch of 125 $\mu$m, see Figure 2.3. Considering manufacturability, it is fair to give the tracks a width of 75 $\mu$m with a spacing of 50 $\mu$m. Placing the die in the nominal position it is clear that the die can be offset by 25 $\mu$m with the bump and the track still overlapping 100%, see Figure 2.3. For larger dies this number becomes more favorable, and also making a smaller line spacing will yield a larger allowance for misplacement.

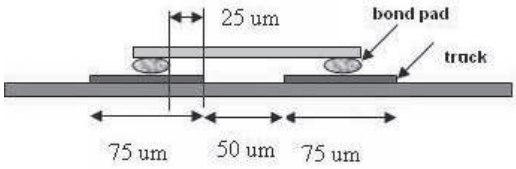


Figure 2.3: Definition of placement accuracy.

IOP committee members representing the Dutch organizations: Besi, Assembléon, Philips and TNO have defined the requirement for the placement accuracy to be 35 $\mu$m for the 300 $\mu$m squared die.

## 2.2 New Technologies in Microassembly

Ultimately, both in research and in production, achieving the goal (in its broadest sense) at minimum cost is the only objective. Costs can be measured both in time and money. There is a rapid expansion of the number of applications requiring volume assembly of dies below 1 mm, driven by RFID and LED technologies. However, because microassembly is expensive (one third of the final product cost) and quite slow (max. 2 components per second), we are looking for a new technology that will provide mass assembly with high throughput.

One possible approach towards microassembly is to improve the performance of conventional automated assembly systems. Commercial robotic systems with a resolution and repeatability of a few microns are available (e.g. from MRSI in Chelmsford, UK, or from Sysmelec in Switzerland). Prototypes of even higher precision systems have been described [Qua96], [Dan97]. However, this approach requires an increasingly sophisticated technology. It has been observed that smaller parts require larger machines to handle them. Besides, the higher the accuracy, the slower the speed of the assembly. The throughput of serial microassembly is limited by the number of manipulators in the array. The microfabrication process should yield millions of devices; a large number of the microdevices should be assembled simultaneously. This class of microassembly is called "parallel" or "mass". There are two basic approaches; one of them is based on the massively parallel transfer between wafers of arrays of microcomponents (deterministic parallel assembly) and the other one utilizes vari-

ous approaches to orient an initially random array of microparts (stochastic parallel assembly). These topics will be addressed below in separate subsections.

## 2.3 Stochastic Assembly

While conventional assembly techniques have been successfully adapted from the macro world, the molecular regime offers many examples of an efficient assembly process. Crystal growth, antibody-antigen recognition and other chemical and biological behaviors [Can80] are mediated by thermal motion and interparticle forces. In contrast to the macroscopic concepts of manipulators, a molecular system may be analyzed as an ensemble of particles evolving toward a state of minimal potential energy. The benefit of this thermodynamic approach is that when parts must be redistributed or reoriented, a single complex manipulator may be replaced with an array of defined binding sites. Such sites might consist of electrostatic traps or simply of wells etched on a substrate. Thermodynamic analysis shows the potential of a massively parallel operation, forming 10 000 000 or more elements in seconds, with the placement tolerance limited by lithographic accuracy [Coh98]. In stochastic assembly there are two main groups that could be divided according to the liquid or dry environment in which the microcomponents are situated.

### 2.3.1 Fluidic Self-Assembly

Several research groups have demonstrated the self-assembly of microscale components onto a substrate using various forces for attraction and binding: shape-directed fluidic methods that position electronic devices on planar surfaces using shape recognition and gravitational forces, [Fea95], [Smi98] liquid-solder-based self-assemblies that use the surface tension between pairs of molten solder drops to assemble functional systems, [Fea95] and capillary force-directed self-assembly that uses hydrophilic or hydrophobic surface patterns and photocurable polymers to integrate micro-optical components and semiconductor chips on silicon substrates, [Jac02], [Sri01].

The latter process emerged in 1994 when Yeh and co-workers developed a fluidic self-assembly process [Yeh94]: GaAs LEDs were placed in an array of trapezoidal pockets on a silicon wafer by a self-assembly process. The LEDs are suspended in a fluid that is dispensed over the silicon wafer. The selection mechanism is based purely on the geometry of the object and the pocket. Before evaporation of the fluid, 90% of the holes are correctly filled with LEDs. However, during evaporation, surface tension pulls some of the objects out of the holes, reducing the yield by 30% to 70% locally.

This technology has spun-off to Alien Technology of Morgan Hill, USA, a company that claims to have the capability of roll-to-roll production of RFID interposers. This method works as follows (also see Figure 2.4): after wafer fabrication, dies are separated from the wafer using wafer thinning, followed by a form of etching. The etching is carried out in such a way that the dies emerge with a trapezoidal shape referred to as Nanoblocks$^{TM}$. Meanwhile, matching trapezoidal holes are embossed into the substrate. The dies range in size from ten to several hundred microns, and are suspended in the fluid, usually an alcohol solution, from which they flow into the embossed holes in the substrate. The process promises a high yield and low costs and, also very importantly, the ability to scale to massive volumes. Once the dies

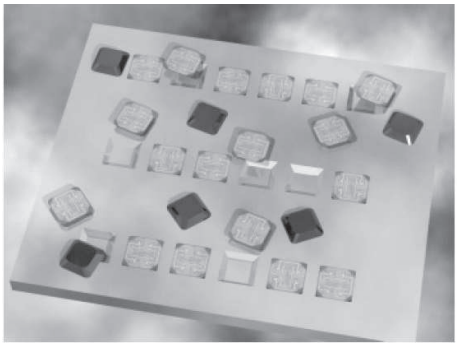

Figure 2.4: Nanoblocks falling into substrate holes. From Alien Technology Corporation (www.alientechnology.com)

are in place, interconnection-to-interposer leads can be carried out with a variety of techniques ranging from lithography to silk-screen printing.

One of the disadvantages of these methods is that identical components are predetermined. If the system consists of more than one repeating unit, this technology is difficult to use. The integration of this technology within the industry was delayed by complex process flow, low yield and the difficulty of angular-orientation control.

As an example of other self-assembly techniques, consider the cylindrical display manufacture demonstrated by Jacobs et al [Jac02]. The experimental strategy for the assembly of components onto substrates is shown in Figure 2.5. To construct a system that required electrical connectivity relevant to displays, GaAs/GaAlAs LEDs were used with a chip size of 280 $\mu$m by 280 $\mu$m by 200 $\mu$m. The chips had two contacts: a small circular cathode on the front, and a large square anode covering the back (see Figure 2.5). The purpose was to induce the LEDs to assemble into a

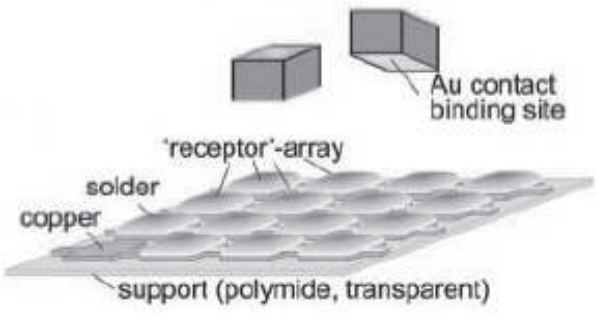


Figure 2.5: Components for display self-assembly, ( [Jac02]

well-defined array of 280 $\mu$m wide copper squares on a substrate that was coated with

a lowmelting point solder (50°C). The surface of the liquid solder wets and adheres to the gold-coated contacts on the back side of the LEDs; minimization of the free surface area of the liquid solder drives the assembly. The solder also provides the electrical connection required to operate the device and the mechanical bond required to hold the assembly together. The pattern used in the prototype incorporated 113 receptor sites (eight columns of eight receptors interleaved with seven columns of seven receptors). The prototype display element was manufactured in two steps: (i) the self-assembly of LEDs on the bottom electrode and (ii) the self-alignment of the contacts with the top electrode. Both steps were performed in water in order to reduce capillary and gravitational forces, see Figure 2.7. For the assembly of the LEDs, the bottom electrode was inserted into a cylindrical 1-ml vial with an inside diameter of 5 mm and then water and LEDs were added. The vial was placed in front

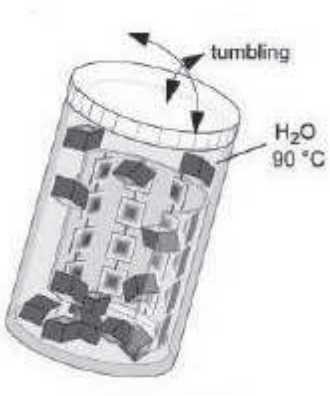


Figure 2.6: Self-assembly step

of a heat gun and the water was heated to 90°C; at this temperature, the solder was molten. The components were placed by shaking the vial manually until all receptors captured a LED (2 to 3 min.). The second step in the fabrication sequence was the self-alignment of the top electrode, Figure 2.7 The film-supported copper wires were coated with low melting point solder. The center-to-center distance between the wires was the same as the center-to-center distance between diodes. During this step, the flexible top electrode was positioned by hand in the approximately correct position to make contact with the top surfaces of the LEDs. When the entire structure was heated above the solder's melting point, the top electrode fused with the solder-coated cathodes of the LEDs, and the entire system adjusted the position of the components to minimize the overall interfacial energy. This process formed an electrical contact with each LED providing 60 $\mu$m placement accuracy with low process yield.

These methods allow the positioning of a large number of identical components in a massively parallel manner, but systems that consist of more than one repeating unit are difficult to achieve. For example, in the shape-directed fluidic self-assembly, small device components will settle by mistake into the holes designed to match the shape of larger components. Similarly, in the surface-tension driven self-assembly, the binding sites designed for one component will almost always overlap with the receptor for a different component.

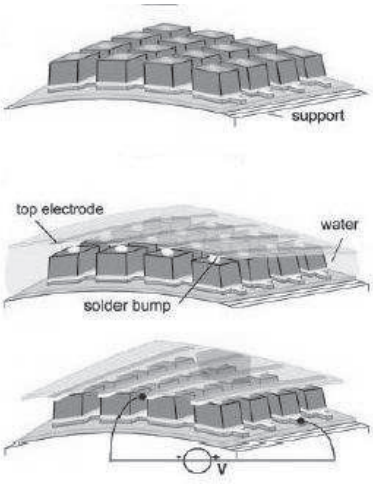


Figure 2.7: Alignment and electrical

A method that combines geometrical shape recognition, surface tension and sequential self-assembly [Zhe06] could make the self-assembly technique industrially acceptable. Up until now no industrial applications are known to the author.

### 2.3.2 Dry Self-Assembly

A typical robotic manipulation scenario is the sequence of "pick, transport, and place" operations. For parts with masses of several grams, the gravitational force will usually be larger than adhesive forces, and parts will drop when the gripper opens. For parts with the size of less than a millimeter (masses less than 1 mg), the gravitational and inertial forces become insignificant compared to adhesive forces. The latter are proportional to the surface area. When parts become very small, adhesive forces can prevent release of the part from the gripper.

Hence, it is essential to have control over adhesive forces during microassembly. A common technique to overcome adhesion is to employ vibration.

In 1991, Cohn and co-workers described stochastic assembly using vibration and gravitational forces to assemble arrays of up to 1000 silicon chips, [Coh91]. The subsequent work demonstrated the use of patterned electrodes to assemble parts. This result promises a sensitive technique for positioning of parts, as well as discriminating part orientation, shape, and other physical properties. The experimental apparatus for self-assembly with electrostatic traps is shown in Figure 2.8. A vibratory table with a gold-coated dielectric is attached to the piezoelectric actuator. The aperture in the upper electrode creates a fringing field that causes polarization in the part. The part is attached to the aperture. The attractive force to the target and the selection mechanism can also be provided with electrostatic fields. Böhringer et al. [Boh98] used a template consisting of a pair of oppositely charged planar electrodes. The upper electrode contains a multiplicity of apertures. In the vicinity of the apertures, the electric field emerges at the template surface. Dielectric material is attracted to these regions with high electric field strength. At first, the template is vibrated so strong that the objects move randomly. With time, the vibration amplitude is

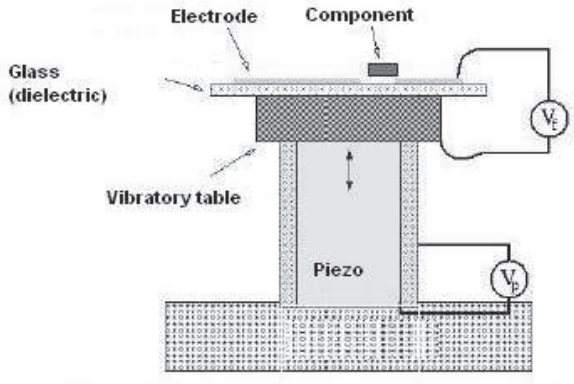


Figure 2.8: Experimental apparatus for self-assembly with electrostatic traps [Coh91]

gradually reduced and the objects are attracted to the apertures and trapped there. The particle's bottom surface is coated with a conductive film which has the same pattern as the aperture. When the particle's pattern fits the aperture, the conductive film stops the field lines at the surface, so only one particle is trapped at the aperture. Discrimination between different types of particles and orientation is obtained by the shape of the pattern. Trap of the wrong particle or bad orientation results in a smaller energy decrease than when the correct particle is trapped in the correct orientation. These local minima are avoided by slowly decreasing the vibration amplitude. An excess of particles helps to cover all sites.

By analogy with the electrostatic attraction and selection mechanism, magnetic templates can also be used [Coh94]. One method is to use a magnetic medium such as a floppy disk on which a magnetic pattern is created. The particles are then coated with a corresponding permalloy pattern. Patterns on the template may be rapidly, economically and microscopically created in arbitrary planar configurations by means of a magnetic recording head.

Note, however, that since this technique relies on the inertia of the parts, vibration becomes less efficient with decreasing part sizes, i.e., higher vibration amplitudes or frequencies are necessary for smaller parts.

Another example is assembly of a $\mu$ chip, the world's smallest (0.15x0.15 $mm^2$) radio-recognition 128-bit IC chip in use, produced by Hitachi, Japan. This ultra-thin $\mu$ chip (60-$\mu$ thick) is connected to the antenna via an anisotropic conductive film (ACF) [Usa99].The first problem is how to precisely position a chip with small surface bumps onto the metal terminals of the external antenna. A small double-surface chip could resolve this problem. Chips do not require horizontal-direction regularity for mounting and can be mounted using upside-down free positioning. Figure 2.9 shows the structure of the connection between the chip and the external antenna. The ultra-small, double-surface connection chip is placed between the antenna metals. The upper-side metal is formed using a folded thin-film metal with the same thickness as the lower-antenna film of the substrate. The double-surface electrode RFID chip can be easily connected to the antenna without precise positioning. Another advantage of having the double-surface connection is that each connection area can be designed to

be as large as the chip surface to reduce connection resistance and enhance connection reliability. Many chips, for example, 16 chips in a 4x4 matrix, can be placed using a

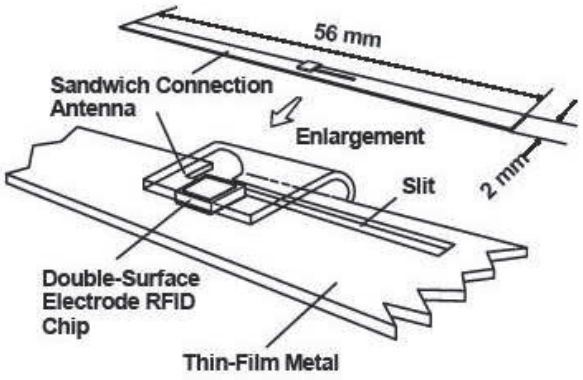


Figure 2.9: Antenna connection technology of ultra-small (0.15x0.15 mm$^2$ RFID chip, [Usa04]

rough positioning plate, Figure 2.10. Each chip is dropped slightly into each absorbing hole using vibration, and fixed using the vacuum method. The positioning plate rotates and simultaneously mounts each chip on the antenna sheet, which is folded to match a placing pitch for each chip on the plate. Another type of the $\mu$-chip is the

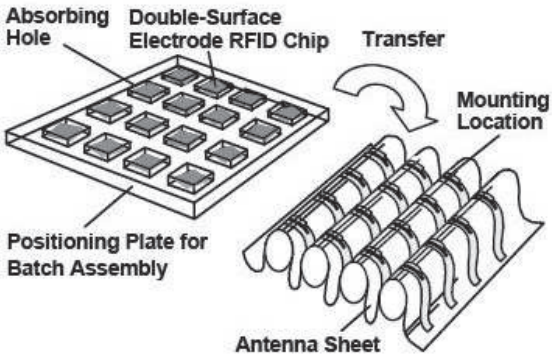


Figure 2.10: Assembling technology of ultra small RFID chip. The double-electrode chips are suitable for batch assembly [Usa04].

0.4 4×0.4 mm$^2$ chip with an embedded antenna. The scheme of the internal circuit is exactly the same as that one with an off-chip antenna. The communication area is about 3-millimeter which is a practical usage level for close-coupled RFID devices: cheap on paper and readers, e.g. money, tickets, labels in the market, smart labels, etc. The connection of an embedded chip for these applications does not require high precision and the speed of the assembly is the main factor.

These self-assembly methods look tempting because of their simplicity. However, none of them is 100% reliable which limits their practical use.

## 2.4 New Developments Based on Conventional Equipment

In this chapter the overview the existing conventional techniques which use innovative processes to reach high speed assembly of the micro-components are described.

### 2.4.1 PICA: Parallel Integrated Chip Assembly

The first prototype operating using the Parallel Integrated Chip Assembly (PICA) process was built in 2003 by Matrics, Long Beach, Calif., USA. Instead of a one-at-a-time, labor-intensive process, 8-inch-wide sheets of wafers attached to a specially designed backing (wafer) plate are loaded into the machine. The sheets will fit into any web press. While the sheets move through the first part of the machine, a quick-curing adhesive is applied. Next, the wafers move under a "bed of nails" (pin plate), pre-positioned to the pitch of the antennas and waiting to apply the die. The wafer plate has holes located exactly where the die is to be attached. The pin plate punches through the corresponding holes in the wafer plate, applying the die to the adhesive, Figure 2.11. An ultraviolet (UV) lamp is flashed to cure the adhesive in one-tenth of a second. More than three years later, PICA was still not producing RFID,

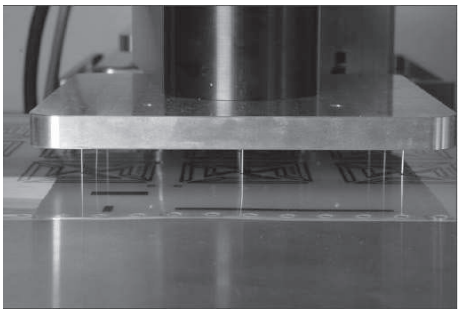

Figure 2.11: PICA assembly [Arn04]

because the machine failed to provide a high enough yield of tags that functioned properly. The main problem with the machine was precisely aligning the microchips with preprinted antennas. The root of the problem was a component that used a computer and optical sensors to control gears to shift the inlays to the left or right, or slightly forward or backward, to ensure the chip was placed precisely. Another issue involved a component that punched the microchips from a release tape down onto the antenna. The chips were not released properly.

### 2.4.2 Ultrathin Silicon Assembly

Current trends in the thin chip technology are targeting extremely low packaging heights, new sensor components, thin and flexible ICs for smart labels and highly integrated chip systems for multifunctional devices. Driven by this evolution, the wafer thinning technology has been promoted down to a silicon thickness of 20 $\mu m$ and even below. These chips are ideal for integration into thin and bendable systems.

In order to remove a single chip from its carrier (to pick-up the chip from the dicing tape), the chip must be of particular stiffness compared with that of the tape.

When the tape is bent to a particular point the chip resists the bending force and the tape begins to peel away from it.

This method of removal does not work with chips that are about 50 $\mu$m thick and thinner because they are highly flexible themselves. For these kinds of chips a new process is required. Several approaches with penetrating or nonpenetrating needles exist. The most promising technique has been developed by Fraunhofer-Institute for Reliability and Microintegration in Berlin, Germany and now studied in the Project InnoSi, founded by the European Committee.

The InnoSi research programme (Innovative production processes for new products based on thin silicon devices) has been developing a new technology for assembly and contacting of thin ICs. This process avoids the damage of thin components and is relatively fast (around 200 ms per die). The classical pick-up tape is replaced with the one with a special adhesive-coated film. At a specific temperature the adhesive completely loses its stickiness. This is achieved by a specific change of the surface characteristics.

A special heating tool is developed which allows local heating of the thermal release tape, Figure 2.12. This heating stamp replaces the needle ejector of the die

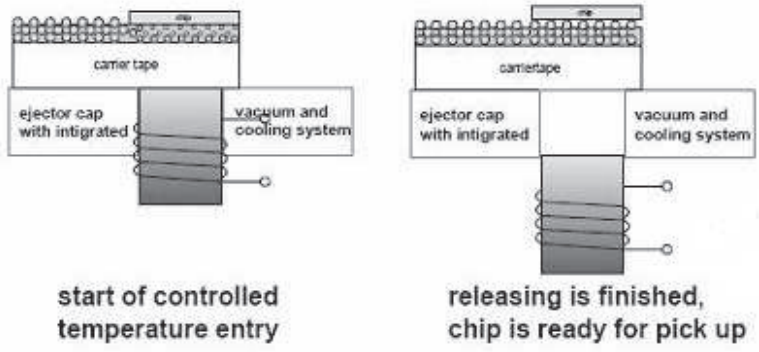


Figure 2.12: InnoSi developed process: releasing of the ultra thin components using a heating stamp and a special thermal tape, [Lan04].

bonder [Lan04].To achieve cycle times within the range of about 200 ms per die, the temperature and the size of the heating stamp have to be adapted to the characteristics of the thermal tape and to the size of the die. This makes the process quite limited to the die size and makes the stamp process very complex (integrated cooling system, high position accuracy for small dies, changing the tape thickness for increasing the process speed, etc.). The main disadvantage is the alignment issue of the heating tool with the releasing die when the size is smaller than 1 mm$^2$.

## 2.5 Laser Die Transfer: Assembly requirements

In the previous paragraphs the main requirements for the assembly processes were described and available techniques were presented. To fulfill the growing needs of

the semiconductor industry, new techniques are being developed. Some of these techniques provide high throughput, others focus on possibilities to handle thin components using the pick-and-place process. All of these systems have disadvantages, though: mass assembly techniques are non-flexible (only identical components can be placed) and have a low process yield (low assembled-non assembled ratio), whereas new pick-and-place processes are complex, suffer from bad alignment and are too slow.

The laser-based device-transfer technique which will be referred to here as "Laser Die Transfer" is an alternative to the conventional pick-and-place methods. This process will fulfill the main needs of the new assembly: assembly throughputs of 100 components per second become possible and the smallest and thinnest components can be transferred in a touchless manner, which eliminates risks associated with mechanically driven damage. Also, this process is flexible enough to transfer component sizes ranging from 0.1 to 10 $mm^2$.

The best application of this technique is flip-chip assembly. It could also be applied to the transfer of such micro-meter sized structures as semiconductor bare die and optoelectronic devices, as well as micro-electro mechanical systems (MEMS). In addition, it could be used in the wire-bonding technique with an additional process step: re-taping of the wafer which turns the die's active side toward the wafer tape. However, since the next step - wire bonding itself - is slow, the main advantage of the laser die transfer technology - its speed - is not very beneficial.

The maximum temperatures that components can handle depend on the materials which are used in the manufacture of the component itself and the method of interconnection. In most processes, the assembly is done by applying small dots of solder or conductive adhesive paste, that are fixed after assembly by soldering or curing. The temperature of the soldering is taken as the maximum allowed process temperature. To summarize the above, the main requirements for the laser transfer process are as follows:

- Release of the die from the carrier substrate without mechanical and/or thermal damage. The temperature limit is 400°C, corresponding to the maximum soldering temperature;
- Placement accuracy within 10% of the component's size;
- High process capacity - more than 100 000 units per hour;
- Mechanical connection of the component to the receiving plate;
- Flexibility. The equipment must be able to handle parts of varying dimensions.

## 2.6 Summary

Microassembly is a challenging area of research. This chapter identified the important requirements in this field. Novel techniques for the massively parallel assembly and new trends in the manipulation of the small and thin components were discussed.

None of these new techniques proved to be beneficial and reliable enough to be accepted by the industry. The disadvantages of most of the presented new mass-assembly techniques are: too low ratio of assembled/not assembled components, shape

and size limitations, and the problem of how to release thin components from the initial wafer tape. A process called InnoSi, which allows this type of release by using special thermal tape and a complex ejector head, presented. However, the speed of this machine is too low (more than 2 sec. per component), and the process is complex and not reliable due to big alignment errors.

An explanation of the requirements for placement accuracy was presented and future trends for assembly were discussed. As demonstrated, high speed is more important for new applications than high precision. An example was presented of the newest RFID $\mu$-chip assembly, where precision is less crucial than throughput.

Assembly requirements for the developed Laser Di Transfer technique, which is the topic of this thesis, were presented and explained. It was stated that, potentially, Laser Die Transfer can fulfill the main needs of the novel devices assembly: it provides high throughput and the possibility to handle ultra-thin and small components without thermal and/or mechanical damage.

# Chapter 3

# Laser-induced Transfer Methods

A variety of laser-induced material transfer techniques exist: LIFT (Laser-Induced Forward Transfer), PLD (Pulsed Laser Deposition), MAPLE-DW (Matrix-Assisted Pulsed Laser Evaporation-Direct Write), and MELD (Microstructuring by Explosive Laser Deposition). LIFT and MAPLE both use Excimer lasers with pulse lengths in the range of nanoseconds. MELD uses picosecond lasers, which decouples the expansion and heating phases of the material.

Laser-based transfer technologies are diverse in nature and are currently at different stages of development. The developers of these systems have developed processes to transfer and deposit metals and other materials from donor films to substrates [Dre79], [Chr94].

## 3.1 Pulsed Laser Deposition

Pulsed Laser Deposition (PLD) is a versatile laboratory technique for the synthesis of material prototypes in thin film form. In Pulsed Laser Deposition the ablation of material is generally performed in a set-up as shown in Figure 3.1, by a nanosecond excimer laser (KrF, ArF) operating at UV wavelengths (248 and 193 nm, respectively), or at the second harmonic of Nd:YAG laser radiation (532 nm), [Eas07]. These wavelengths are weakly absorbed by the plasma which minimizes plasma influence during the ablation process. The radiation is focused on the surface of a rotating target (e.g. silicon) an incident angle of approximately 45°. The laser radiation intensity is usually approximately $10^8$ to $10^9$ W/cm$^2$. The laser-induced plasma plume expands perpendicular to the target surface. The substrates are placed on a rotating substrate holder at some distance (usually a few centimeters) from the target. The substrate is either kept at room temperature or heated to improve the adhesion of deposited material. The deposition is carried out in the presence of inert (He, Ar) or reactive ($O_2$, $N_2$) gases, maintained at a reduced pressure (typically 0.013-27 mbar). The results of the localized heating and vaporization can either be simple vapor deposition onto a substrate or the physical transfer of a portion of the thin film, as a solid.

## 3.2 Laser Induced Forward Transfer Process

Laser-induced Forward Transfer (LIFT) involves selective forward ablation and deposition of materials using lasers. This technique usually utilizes pulsed lasers to remove a thin film of target material from a transparent supporting plate to deposit it onto a receiver substrate, see Figure 3.2. Various metals and oxides have been used in LIFT

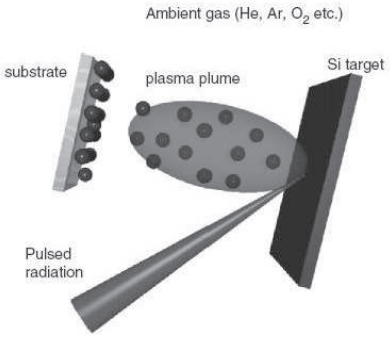


Figure 3.1: Schematic of PLD experiment for deposition of Si-based nanostructured films, [Eas07].

applications, together with a variety of laser sources, from the near infrared to the ultraviolet. In most cases, transfer of material is achieved using single laser pulses, although it has also been demonstrated by the use of continuous wave (cw) lasers.

The LIFT process was first demonstrated by Bohandy et al. [Boh86] to be capable of producing direct writing of 50 $\mu$m wide Cu and Ag lines by using single pulses of a nanosecond ArF excimer laser (193 nm) under high vacuum conditions ($10^{-6}$ mbar). This was the beginning of a systematic study on applications of LIFT in forming conductive lines such as interconnects and, further, in microelectronics.

In general, the principle of the LIFT method is outlined in Figure 3.2. The target material is deposited on a quartz wafer or another laser-transparent substrate. The distance between the target and the receiver substrate typically ranges from near contact to several micrometers. Laser light is projected at the transparent support/thin-film interface, Figure 3.2 *a*), vaporizing or ablating a fraction of the target material, Figure 3.2 *b*). The fraction which is vaporized depends on the laser wavelength, laser intensity, and the optical extinction coefficient of the target. During this process, the vapor pressure expels the remaining material at high speed, Figure 3.2 *c*). A mixture of the solid and the melt is ejected at high speed and impacts on the receiver substrate *d*). The term "pattern transfer" was often taken to be synonymous with lithography and photolithography, in micro and nanotechnologies. The limitations that photolithography now faces are based on physics of diffraction. Additionally, this method involves a large number of processing steps and is not suitable for all types of materials, since the etching and stripping process uses chemicals that can damage sensitive materials. As a result, current the non-photolithographic methods for pattern transfer are in development. There are several requirements for LIFT to produce useful patterns: the laser fluence should just exceed the threshold for removing a thin film from the transparent support. In addition, the target thin film should not be too thick - less than 500 nm, the target film should be in close contact to the substrate, and the absorption of the target should be high. Despite the advantages of LIFT, the materials are limited to metals and simple oxides [Piq02]. The vapor must have sufficient pressure to cause the film to break locally and to be detached from the support. Limit of the transferred material thickness prevents LIFT from being used

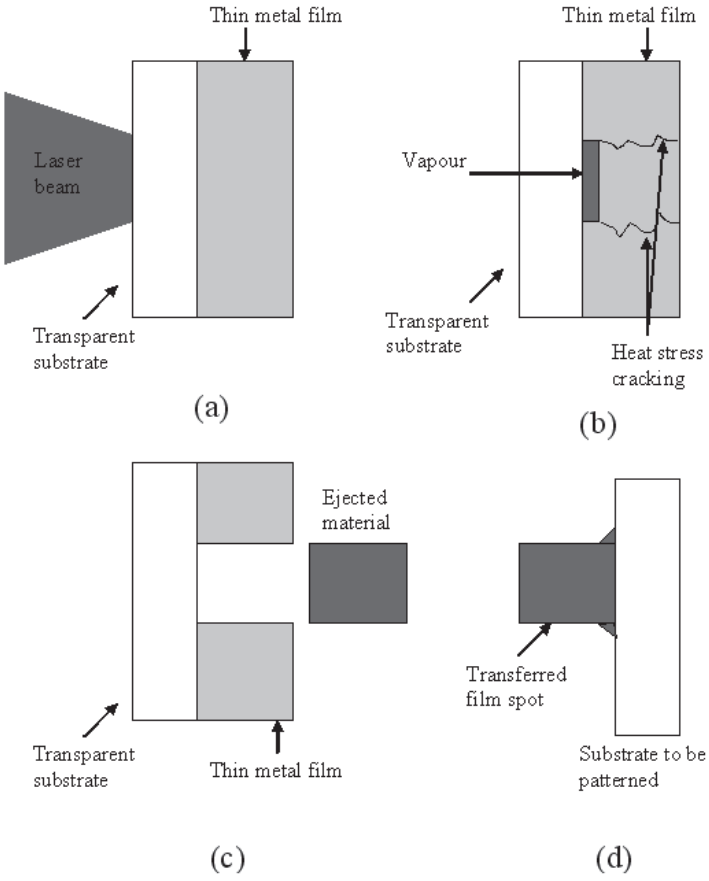


Figure 3.2: Scheme of the Laser-Induced Forward Transfer method: (a) laser beam is projected at the transparent support/thin-film interface; (b) the fraction of the film is vaporized, heat stress cracks appeared; (c) a mixture of solid and melt is ejected at high speed; (d) transferred film spot is impacts on the receiving substrate.

for most thick-film microelectronic applications.

## 3.3 Matrix Assisted Pulsed Laser Evaporation (MAPLE) and MAPLE Direct Write

Matrix-Assisted Pulsed Laser Evaporation (MAPLE) and MAPLE Direct Write are laser-based processes developed at the U.S. Naval Research Laboratory, SW Washington, USA. These two processes are capable of depositing almost any material. Both MAPLE and MAPLE-DW use inks formed by dissolving the material to be deposited in an organic matrix. In MAPLE, the ink is applied onto a support to form a 1-20 $\mu$m layer at low temperatures [Piq02]. The support is separated from the substrate by typically 5 cm and the entire process takes place in the vacuum as shown in Figure 3.3. The laser energy causes the material to be removed from the organic matrix and transferred onto the substrate. A pattern can be generated by placing a shadow mask over the substrate. The MAPLE process is similar to thin-film deposition processes with the advantage that it can deposit any material because the matrix is evaporated. In this process, the laser pulse has a lower fluence (typically

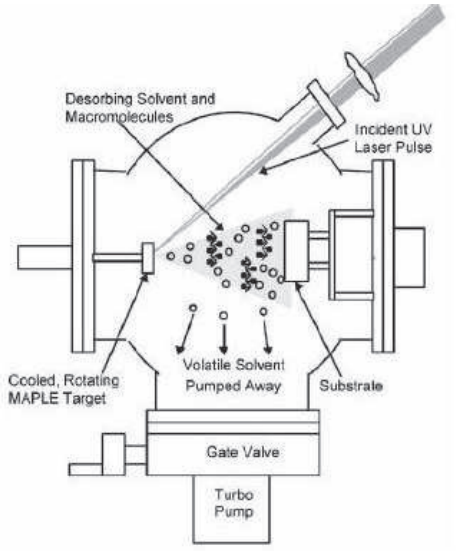


Figure 3.3: Schematic of the MAPLE deposition system from Pique et al [Piq02].

0.2 J/cm$^2$) than in conventional PLD (1.5-5 J/cm$^2$ for metals and ceramics). Unlike conventional PLD, the target is a dilute matrix, made up of solvent and organic molecules to be deposited as a solute. The matrix is typically kept at low temperatures. If tuned correctly, the laser pulse will be preferentially absorbed by the solvent molecules only. The laser-produced temperature rise is above the melting point of the solvent and below the decomposition temperature of the solute. When the MAPLE process is optimized, the solute is preferentially condensed onto the substrate, while the evaporating solvent is pumped away or it can be trapped on a cold surface for re-use.

In MAPLE-DW, a ribbon is placed in close proximity to the substrate (25-100 $\mu$m) in the forward transfer configuration, see Figure 3.4, [JFG02]. A UV laser is

focused through the transparent support onto the ink-support interface. The organic material absorbs the UV radiation and is rapidly heated and vaporized. This provides a pressure pulse which pushes the material out and deposits it onto the substrate. The substrate can be translated relative to the laser to write very precise patterns. The entire process takes place in ambient conditions and does not heat the substrate. MAPLE-DW is similar to LIFT with the exception that the transfer is much softer (lower velocity) and requires lower laser fluence. In addition, the ink can be selected so that the organic MAPLE matrix preferentially absorbs the laser energy and heating of the active material is minimized. This allows the direct writing of polymer and organic materials that otherwise would be damaged by heating during the LIFT process. A laser substrate such as a quartz disc or polyester film is coated onto one

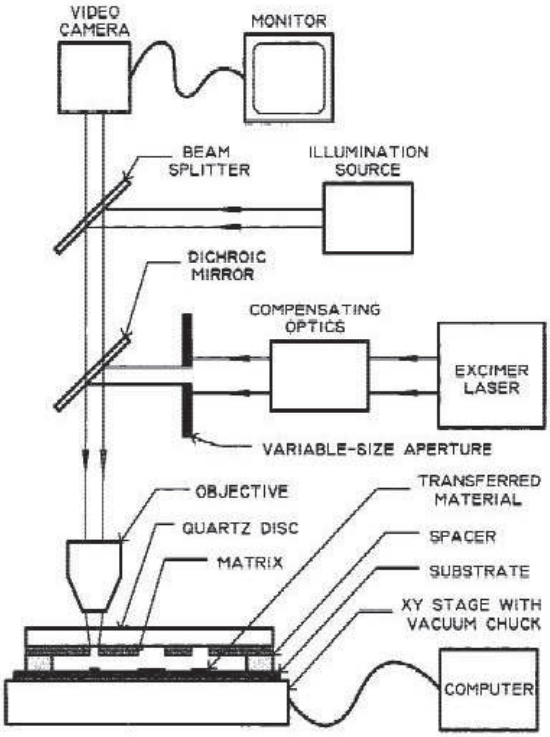


Figure 3.4: Schematic diagram of a MAPLE-DW system [JFG02].

side with a thick film of the material to be transferred, typically 1-20 microns thick depending on the material and application. The film is typically a fluid, ink or paste that consists of a dispersing fluid, polymer, or organic vehicle in combinations with powders, soluble chemicals, biological materials. The carrier plus a thick film is placed in close proximity (5 to 100 $\mu$m) to the acceptor substrate. As with LIFT, the laser is focused through the transparent substrate onto the ink layer, see Figure 3.5. When a laser pulse strikes the ink, a small portion of the ink is vaporized at the ink/carrier interface, and the vapor expansion transfers the remainder onto the acceptor substrate. During MAPLE-DW transfer the majority of the ink is not vaporized. This allows complex suspended powder materials and dissolved chemicals in the organic vehicle

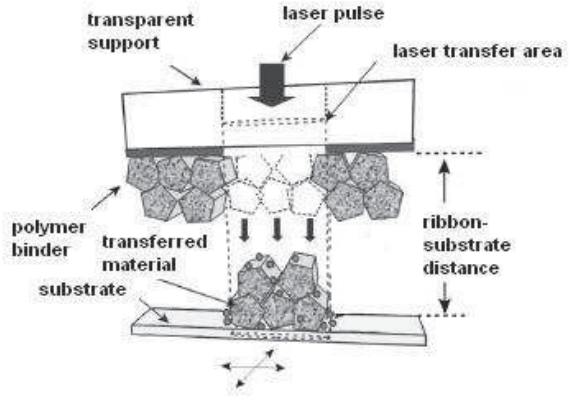


Figure 3.5: Diagram of MAPLE-DW ribbon, ink layer, and substrate during transfer [JFG02].

to be transferred without substantially modifying their predeposition properties.

## 3.4 Laser Propulsion

In the described in this thesis research the laser irradiation is used to release the component and make it fly freely towards the receiving substrate. There are several other projects which use lasers to make a large and small objects fly using laser initiated propulsion.

On the large scale the concept of Laser Propulsion is accredited to Arthur Kantrowitz [Kan72]. During the 1960s after the invention of the laser, scientists investigated the basic phenomenon of laser-induced breakdown of gases and plasma ignition which forms the fundamental basis of pulsed laser propulsion [Pir72]. During the remainder of the 1970s, much attention was directed towards conceptual design and basic research of using beamed energy from a ground based laser to assess the possibility and feasibility of laser energy for rocket propulsion. Several of these studies involved laboratory scale experimentation for proof of the concept. Three of the most promising concepts are the repetitively pulsed (RP) laser concept [Myr98], [Mea98], air-breathing RP laser launcher [Kat04] and continuous wave laser thruster [Kom02].

As an example, the air-breathing RP laser launcher concept is shown in Figure 3.6. When the laser beam is transmitted from the ground and focused by a parabolic nozzle, breakdown occurs near the focus, and plasma is formed. The plasma absorbs the following part of laser energy and expands outward generating shock waves. The shock waves reflect on the nozzle surface, generating thrust. Because the energy is provided from the ground and the atmospheric air is utilized as a propellant, neither energy source nor propellant is loaded on the vehicle.

Firstly, when the vehicle is launched from the ground, the inlet is closed to prevent the blast wave from going upstream beyond the inlet. Air is taken and exhausted from the rear side of the vehicle. This flight mode can be called a pulsejet mode. Secondly, when the vehicle is accelerated enough for the inflow air to become free from thermal

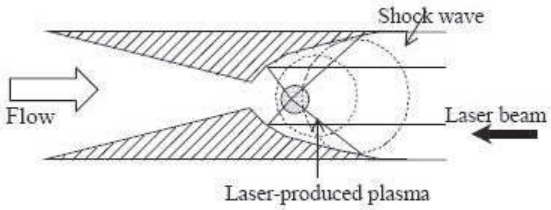


Figure 3.6: Schematic of laser jet [Kom02]

choking by laser heating, the inlet is open and the flight mode is switched to a ramjet mode. Finally, when the vehicle cannot breathe enough air at high altitude, the flight mode is switched to a rocket mode.

Full advantage of the promise of laser propulsion requires a high power pulsed laser and consequent efficient air absorption, energy confinement, and gas expansion. The real problem is a nonlinear optimization problem involving the propellant (air), the laser wavelength, the pulse duration, the pulse repetition frequency and the laser power (energy). The selection of a laser wavelength is a critical issue for laser propulsion. Most work to date has been concentrated on the 10.6 $\mu$m wavelength because of the availability of high power $CO_2$ lasers. The optimal wavelength will depend on tradeoffs between a variety of parameters, including transmission, absorption, laser efficiency, and the specific mission. Absorption favours longer wavelengths, whereas transmission through the atmosphere and optics favours shorter wavelengths. State-of-the-art $CO_2$ lasers typically reach 100 kW average power on the order of a few minutes of operation. Closed cycle designs exist which would allow for continuous operation. The developed models [Kom02] showed that for the 1 meter diameter vehicle to reach orbital velocity the minimum required specific power is 0.3 MW/kg neglecting the energy conversion and transmission losses.

### 3.4.1 Laser micro-propulsion

On a more modest scale, there are investigations that use small pulsed lasers to give thin flyers velocities of several kilometers per second or more [Tro89]. Laser accelerated thin foils (flyers) are a quantitative tool in high-pressure physics [Pai91], astrophysics [Roy95], material sciences [Asa90], and for ultrafast ignition of explosives [Wat00].

One of the applications uses the small flyers, typically a few microns thick and 1 mm in diameter, that are accelerated by this method to create a shock wave in the receiving surface to study the materials properties [Asa90]. The basic geometry under consideration is shown in Figure 3.7 and involves placing a thin film of metal onto a window or optical fiber end-surface. The laser pulse traveling through the transparent medium vaporizes the back of this material film and forms plasma that is confined by the remaining part of the sheet. There is a delay between the arrival of the laser pulse and the onset of foil motion [Tro92].

When a high-fluence laser beam ($10^8$-$10^{12}$ W/cm$^2$) interacts with a metallic target, the amount of thermal energy deposited at the metal surface depends strongly on the metal absorptivity, which is a function of temperature and laser wavelength. When

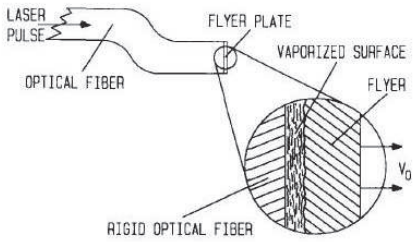


Figure 3.7: Schematic for fully tamped, laser-driven flyer configuration [Asa90].

the laser fluence becomes sufficient, vapor followed by dense high-pressure plasma appears between the metal and the confinement window. The plasma expands and pushes away the flyer at high velocity.

Because of the system's modest scale, the total laser energies are no more than several tens of millijoules. An 8 ns pulse from a Nd:YAG laser operating at 850 mJ achieves a plate velocity of 3 km/sec. Large power densities and energy losses inevitably result in high temperatures in the plasma behind the flyer, which makes it melt and rapidly vaporize. It was determined that this process of ablation accounted for 0.5 $\mu$m of the aluminum film. One means of successfully moderating such effects is to create a composite flyer with layers of metal oxide that act as thermal insulators [Tro96].

## 3.5 Summary

The process of laser transfer techniques described above, is based on local vaporization of the material or ablation and plasma formation. The material transferred is completely modified during the transfer, as in the case of Matrix-Assisted Pulsed Laser Evaporation (MAPLE) and Pulsed Laser Deposition (PLD). In the case of Laser-Induced Forward Transfer (LIFT) and MAPLE-DW material transferring is based on "sacrificial" layer evaporation, which gives the propulsion force to the transferred object. These techniques are commonly used for the transfer of ultra-small and thin layers of material (1-20 micron thick). Only MAPLE-DW provides a process that does not overheat and is suitable for a thermally sensitive rigid body such as the semiconductor die. MAPLE-DW is an extremely complex process because of the spectral ink, used in the process as a sacrificial layer and the very low temperatures during the process.

Laser propulsion is another technique developed for the propulsion of objects that are 1 mm in diameter and a few microns thick. These developments concentrate mainly on the propulsion efficiency, because the future application is the object's propulsion into space.

The two release approaches described further in this thesis have a parallel with the presented techniques. We named the first approach "ablation-induced release". This process is very similar to the laser micro-propulsion technique, because a high-intensity laser pulse is used and propulsion is based on the component material evaporation. The second approach named "thermal-induced release" is based on the special

tape properties and can be compared with the MAPLE-DW technique. The advantages of the Laser-Die Transfer technique are: manufacturable materials are available, no special environment is needed, different-sized components can be released without beam size modification and there is no need for an additional step for cleaning the component of residuals after the release.

At the 4th International Congress on Laser Advanced Materials Processing in Kyoto, Japan, in May 2006, the Laser Die Transfer process and results were discussed in person with a developer of the MAPLE-DW process from the Naval Research Laboratory, USA. About one year later, in October 2007, their developers published an article in the journal "Photonics Spectra", wherein they introduced a new laser-based devise-transfer process called "Lase-and-Place", using the same principle as Laser Die Transfer to release bare dies from the carrier material, unfortunately without any reference to our work, [SM07].

Each component is mounted onto a laser-transparent support using an intermediate polymer sacrificial layer. Upon exposure to a laser pulse the sacrificial layer is ablated, and the generated vapors release and propel the component away from the support. The samples were prepared on the quartz plate. First, the special coating material was spin-coated on the quartz. Then, the components were placed on this layer and dried at 100° C for 30 minutes. Afterwards, the remaining coating was removed using methanol, which resulted in an array of devices glued to the quartz wafer on small "pedestals" of the sacrificial material. A single pulse of excimer laser (248 nm) was used to release the device from the carrier. Components of 1 mm by 1 mm were released with the threshold fluence of 135 mJ/cm$^2$. In Figure 3.8 the schematics and photos of the process are presented.

In a) and d), the laser pulse has not yet hit the sacrificial polymer layer, and the device is still attached to the ribbon. In b) and e), the laser ablates the polymer, causing its vaporization, which results in the ejection of the device from the ribbon. The bright flash from the ablated polymer almost engulfs the substrate in e). In c) and f), the device is released and moves away from the ribbon toward the receiving substrate (not shown). No accuracy results or information about the release dynamics were disclosed.

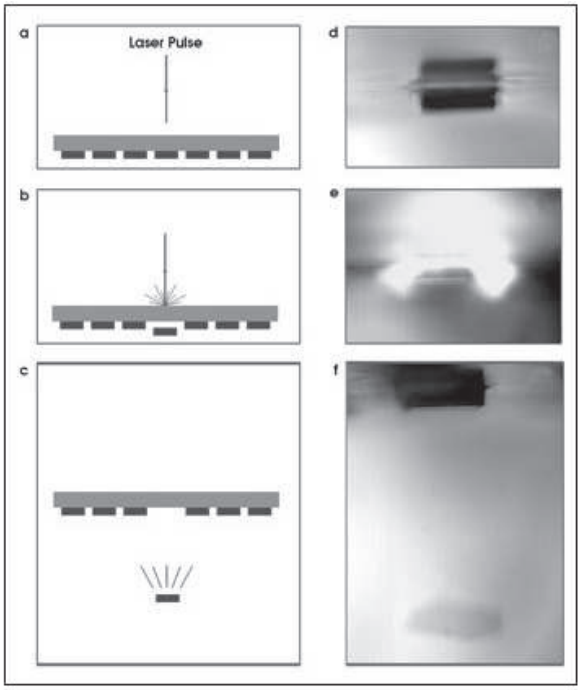


Figure 3.8: The schematics (left) and photos (right) of the Lase-and-place process [SM07].

# Chapter 4

# Ablation-induced release experiments

## 4.1 Introduction

In this Chapter the ablation-induced die release process is studied experimentally. An outline is given of the used equipment, the materials and their preparation. Finally the methods used for analysis of the result are presented.

## 4.2 Experimental equipment and set-up

A Rofin-Sinar, PowerLine D, diode pumped Nd:YAG RS.M-50D laser, operating at the fundamental wavelength (1064 nm), was used as the first investigated laser.

The scheme of the experimental setup is shown in Figure 4.1 and Figure 4.2.

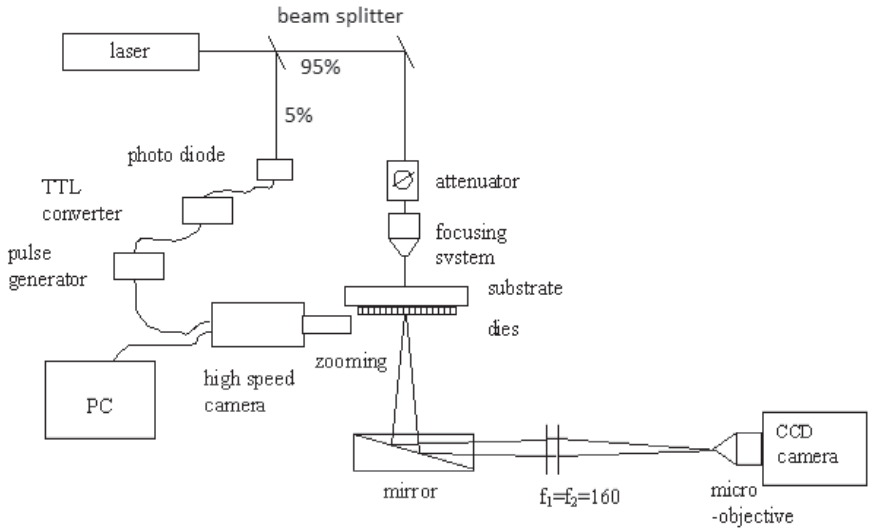


Figure 4.1: The scheme of the designed and realized experimental set-up.

The laser source creates a beam which propagates towards a beam splitter where it is split in two parts. The first part, more than 95% of the laser power, meets an attenuator which can reduce the power in steps, and then reaches the focusing unit, with focal length 160 mm. Then, the focused beam meets the target sample which is placed at the focal plain of the focusing unit. A detection camera is placed

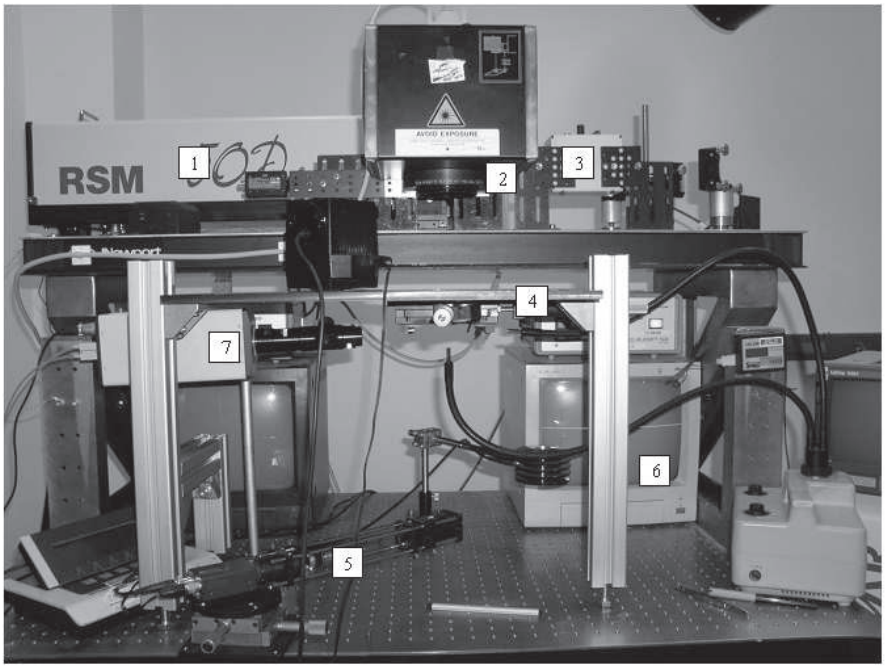


Figure 4.2: Corresponding photo of the experimental set-up: 1. laser source; 2. focusing system; 3. attenuator; 4. substrate with dies placed on the special holder; 5. targeting system (low speed camera, focusing system and mirror); 6. monitor; 7. high speed camera.

perpendicular to release direction in order to image the release process. A white light source is used for the illumination of the area investigated by the cameras.

The second part (5%) of the laser beam propagates to a silicon photodiode which converts the optical signal into an electrical pulse. This pulse is the input to a transistor-transistor logic (TTL) converter, which produces a pulse that is going to be an input to a signal generator. There a rectangular pulse is generated in order to trigger the detection camera.

A targeting system is located below the sample, so that it is possible to select by two micro-positioners a die to be irradiated. Two achromatic lenses, both with focal length of 160 mm, a 10 $\times$ objective and a CCD camera are imaging the surface of the sample on a monitor which is equipped with cross-wires. Alignment is achieved using a pilot laser (diode laser, 650 nm). An IR-filter is used in order to protect the CCD camera from infrared laser radiation.

### 4.2.1 The monitoring system

In order to obtain pictures of the dies' detachment process, a fast imaging unit was used as a detection camera: PCO.Imaging ICX085AL(SVGA) Fast-Shutter SensiCam, of Kelheim, Germany.

The SensiCam offers the ability of very fast imaging of dynamically evolved processes, based on single or multiple exposures within arbitrarily selected time durations. Triggering is achieved manually or by an external TTL pulse. The user can select the

delay between two successive exposures in the range of 0.1 $\mu$s to 1 msec, using delay time equal to zero, one can have exposures longer than 1 msec as well as the time that the shutter stays open in the range of 0.1 $\mu$s to 1 ms. The resolution is 1280 $\times$ 1024 pixels.

### 4.2.2 The target

First, the silicon wafer was diced into individual dies. The process consists of two steps, wafer mounting and wafer saw. Wafer mounting provides support to the wafer to facilitate the processing of the wafer after sawing. During wafer mounting, the wafer is attached to a dicing tape. The dicing tape is a plastic foil with a synthetic adhesive on one side to hold the wafer. To separate the wafer into individual dies the mechanical wafer sawing process was used (using AppTech's dicing team competence). The existing process was not optimized for such a thin wafer (only to find optimal parameters was considered as a project by itself) and therefore it was decided to use another set-up which uses the laser light to dice wafers (process developed and owned by AppTech).

The tapes used for dicing could be divided in three types: so called "blue" which is pressure sensitive, UV-curable and thermal tapes. Pressure sensitive tapes will stick to the wafer with application pressure without the need for solvent, heat, or water for activation. To deactivate this kind of tape, pressure needs to be applied to peel off the tape from the surface. Pressure sensitive tape is suitable for dicing standard silicon wafers, but it is limited to a fixed adhesion value. The goal of thermal tapes is to have an adhesion level high enough to hold the die during sawing, and low enough for the die to be removed easily. Thermal tapes provide two levels of adhesion: stronger during the dicing process, and then reduced when cured with heat for easy lift-off. UV-curable tape loses its adhesiveness by irradiation with UV light. The disadvantage of this tape is that after the exposure by the UV irradiation the adhesion does not drop to zero, the remaining adhesion is usually quite high. The tape used in most cases in the semiconductors industry is the pressure sensitive (blue) one.

#### The Nitto R420+.SWT.500-01-6216 - blue adhesive tape

All dicing tapes have two layers- a backing film plastic covered with an adhesive release layer. The SWT blue tape manufactured by the Nitto-Denko Corporation, Osaka, Japan, has a total thickness of 150 $\mu$m. It consists of poly-vinylchloride (PVC) film uniformly coated with a pressure sensitive adhesive layer.

The thickness of each layer is:

- 100 $\mu$m for the PVC foil and
- 50 $\mu$m for the adhesive film.

To determine the adhesive properties of the blue SWT tape the adhesive force was measured using special equipment manufactured by Zwick/Roell, Ulm, Germany. A cylindrical metallic body with diameter of 8 mm was placed on the tape. The adhesive force of the tape was determined by removing the body from the tape while measuring the applied force. The adhesive force of the used SWT blue tape was found to be 5 N. Transmissivity measurement of this tape using irradiation of Q-switched Rofin 50D Nd:YAG laser with intensities used in the experiments does not show noticeable absorption in the tape.

**The Nitto Revalpha.3198LS thermal sensitive adhesive tape.**

The Revalpha tape, Figure 4.3, manufactured by the Nitto-Denko Corporation, consists of a polyester (PET) film, uniformly coated with a thermal sensitive adhesive layer, which contains a mixture of gas bubbles within a bulk. When the tape is

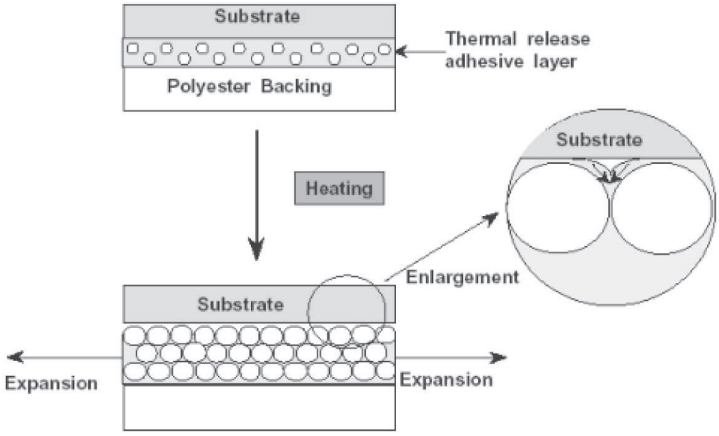


Figure 4.3: The Revalpha 3198LS thermal sensitive adhesive foil and its peeling mechanism.

heated, the gaseous bubbles expand and they create a roughness on the surface which decreases the surface of contact between the attached substrate and the tape. This is illustrated in Figures 4.4 and 4.5. As a result, the adhesive force drops almost to zero and the component can be released. The adhesive properties of Revalpha.3198LS,

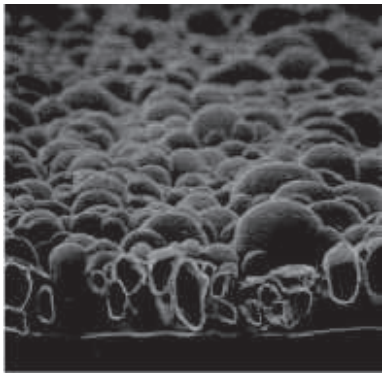

Figure 4.4: Bubbles which grew due to thermal activation of the Revalpha foil.

according to Nitto-Denko Corporation, can be summarized by the two following properties:

- high adhesive strength in standard ambient conditions (room temperature and pressure) and

- rapid vanishing of the adhesive properties when the temperature threshold of 90°C is achieved. Then the adhesive force drops to zero, as indicated in Figure 4.5.

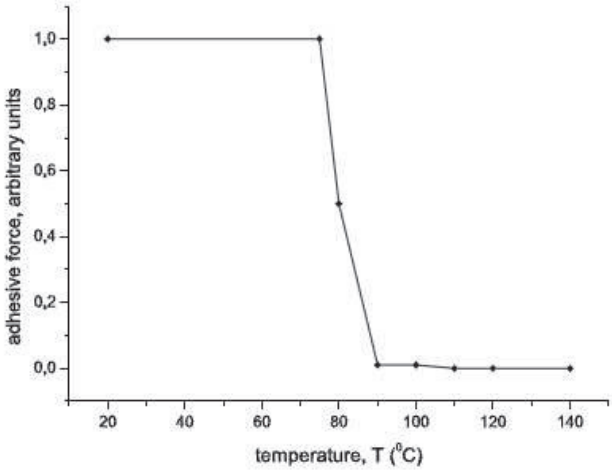


Figure 4.5: The adhesive behavior, according to the manufacturer, of the Revalpha.3198LS foil, when temperature rises due to thermal treatment, [Den08].

The thickness of the tape layers:

- 100 $\mu$m for the PET backing foil and
- 48 $\mu$m for the thermal release adhesive film.

To determine the adhesive properties of Revalpha tapes the adhesive force was measured. A cylindrical metallic body with diameter of 8 mm was placed on each tape. The adhesive force of the foils was measured by removing the body from each foil. The results are presented in figure 4.6. The adhesive force of the used Revalpha tapes is found to be 1.3 $N$. Using a photodetector the tape transmission measurements were performed. The beam size is approximately the same as the detector size. Placing the tape between the detector and the laser beam, (Figure 4.7) and changing the distance between the detector and the tape, it was found that with increasing the distance from the detector, the transmitted energy was decreased, see Figure 4.8. When the tape was placed on the detector directly, tiny absorption could be detected.

The conclusion: glue layer scatters the laser light but does not absorb it. Thus, the tape absorption is neglected in the following analysis.

It should be noticed that to prepare the dies on the Revalpha tape several additional steps have to be taken because it is impossible to use the Revalpha tape as a wafer carrier during dicing process. Preparation steps are the following: the wafer should be diced on the "blue" adhesive tape, such as Nitto R420, and afterwards re-taped in two steps. The first re-tape step is to attach diced wafer to the UV curable tape such as DT-UV-203, produced by STM, San Jose, USA. After that the Nitto

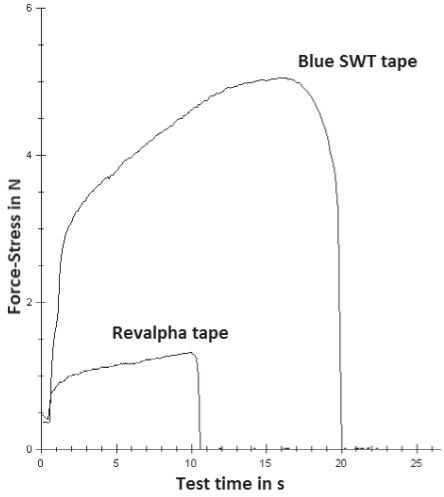


Figure 4.6: Adhesive force measurements concerning SWT and Revalpha tapes.

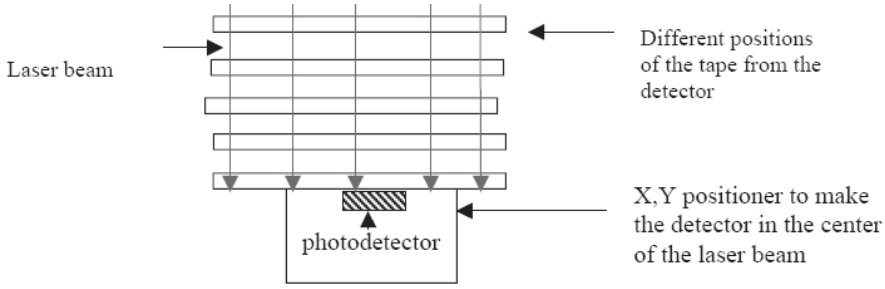


Figure 4.7: The schematic view of the tape scattering measurements.

R430 has to be peeled-of from the wafer, leaving its active side connected to the tape. The second step of the target preparation is to attach the Revalpha tape to the wafer and irradiate the wafer with UV light to release the wafer from UV tape. At the end of this process the dies of the singulated wafer are situated on the Revalpha tape.

### 4.2.3 The laser source

A Rofin Sinar M-50D Q-switched diode pumped Nd:YAG laser, operating in its fundamental harmonic, 1064 nm was used.
The operating software allows the user to select:

- Q-switched or continuous wave (CW) mode of operation,
- the output power by regulating the current of the pumping diodes,
- the number of pulses or the duration of operation, in the case of Q-switched or CW mode, respectively,
- the Q-switching frequency.

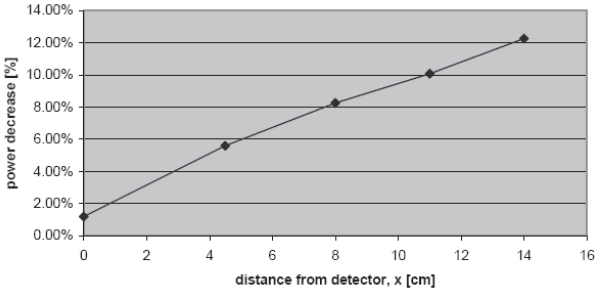


Figure 4.8: Revalpha tape scattering versus distance of the tape from the detector.

The duration of the pulse also depends on the diode current. The temporal shape of the pulse is shown in Figure 4.9. The pulse duration is 45ns FWHM. The spatial

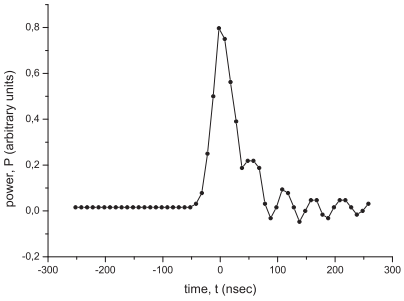


Figure 4.9: The temporal shape of the Nd:YAG laser's pulse for the case of 25 A current and 2.8 mm aperture.

distribution of the laser beam can be adapted by changing the diameter of an aperture inside the cavity, since, this affects the transverse modes, $TEM_{mn}$ in the cavity. Figure 4.10 shows the spatial distribution of the beam for different aperture diameters measured using the MicroSpotMonitor of Primes GmbH. The measurements correspond to a current of 25 A of the pumping diode. As shown, the radius of the laser beam with the aperture diameter of 2.8 mm is 126 $\mu$m. The spot of the focused laser beam used in the experiments is $5 \times 10^{-4}$ cm$^2$, which was obtained with the biggest aperture of 2.8 mm. The intensity spatial profile for this aperture has a "doughnut" shape with some intensity peaks, see Figure 4.10,(c).

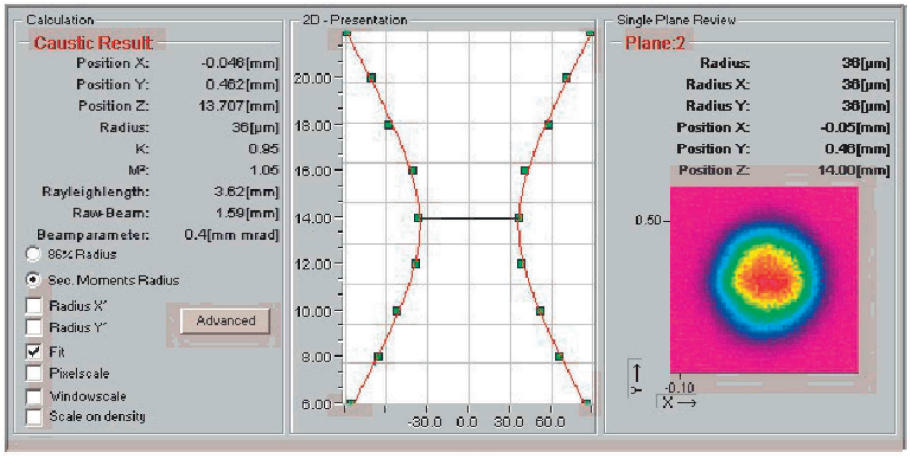


(a)

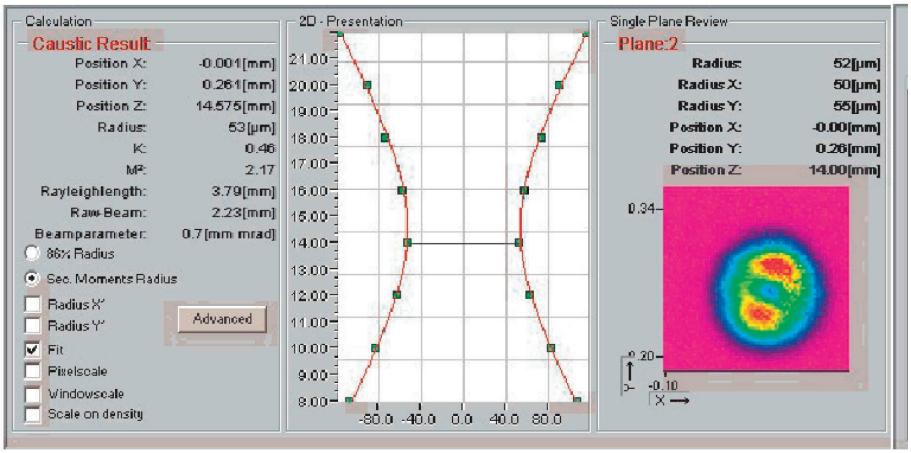


(b)

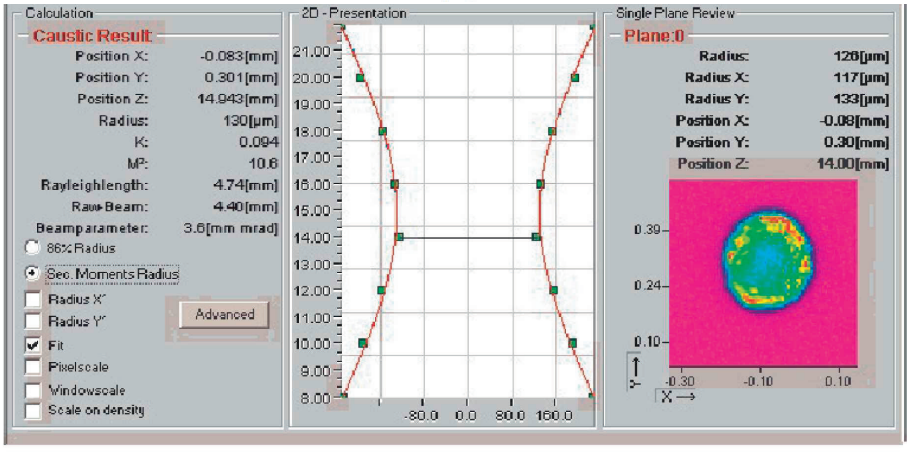


(c)

Figure 4.10: The spatial distribution (profile) of the Nd:YAG Rofin-Sinar 50D laser's beam for 25 A diode current and (a) 1.0 mm, (b) 1.4 mm and (c) 2.8 mm cavity's aperture.

## 4.3 Study of the gold-coated crystalline silicon dies detachment from the Nitto SWT blue tape

The goal of the first experiments was to study the release of the component from its carrier tape, and to obtain information about velocities of the released components. That is, to observe the dynamics of the component's motion.

The dies had the dimensions of $335 \times 335 \times 190$ $\mu$m$^3$. They were coated on one side with a gold layer 1.5 $\mu$m thick, while, on the opposite side a gold bubble with a radius of 67 $\mu$m is placed (see Figure 4.11). The components were situated on the Nitto SWT carrier tape. The setup, shown in Figure 4.1, was used to study the detachment

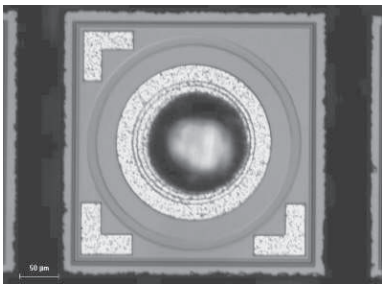

Figure 4.11: The experimentally used golden coated crystalline silicon die.

process.

The high speed PCO. SensiCam was used to image the release process, by a series of frames. The pictures, which had been shot by the SensiCam (Figure 4.12 were obtained by shadowgraphic imaging corresponding to different energy densities. The release was achieved using a single laser pulse. The laser fluence varied from 8.16 to 8.62 J/cm$^2$. In this small range, we obtained the release only near the maximum pulse energy of the Rofin Sinar 50D laser. The time between two successive exposures was 100 $\mu$sec, see for example Figure 4.12.

Measuring the distance of each frame from a reference plane, which is the tape surface in the pictures, the time evolution of the component's position was obtained. Based on analysis of these pictures, no noticeable speed acceleration of the released components at the observed view(4-5 mm) was found, therefore, the velocity of each die was considered as constant with values which vary in the range of 2-6 m/sec, depending on the incident energy density. This implies that acceleration took place during the interval between the first image and the release. Figure 4.13 illustrates the dependence of the average velocity, on the incident energy density. The energy threshold for release was determined experimentally to be $E_{thr}$=8.16 J/cm$^2$ for doughnut beam profile, Figure 4.10.

Observing the position of the golden bubble, in the pictures of Figure 4.12, rotation of the released die is analyzed. The kinetic energy due to rotation can be calculated from:

$$E_{krotat} = \frac{1}{2} J \omega^2, \tag{4.1}$$

where $J$ [kg m$^2$] is rotation inertia and $\omega$, [rad] is angular velocity. The angular velocity could be calculated from photos, such as the ones shown in Figure 4.12, by

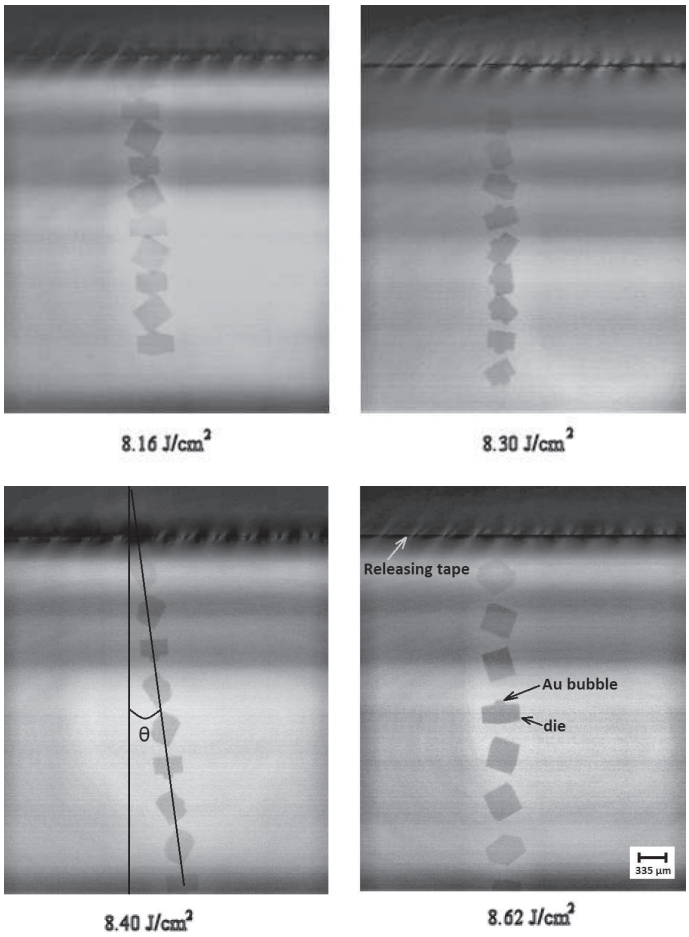


Figure 4.12: Shadowgraphic imaging by the PCO.Imaging SensiCam of the Nd:YAG laser-assisted release process of gold-coated dies for various incident energy densities. The time between successive frames is 100 $\mu$sec.

analysis of the position of the golden bubble. The rotational inertia reads

$$J = \frac{1}{12} ml \tag{4.2}$$

where $m$, [kg] is the mass of the component and $l$, [m] is the length assuming that the component is a thin slab rotated about the axis through the center, perpendicular to the length. The kinetic energy of rotation is found to be $10^{-9}$ J which is 2 orders of magnitude lower than the kinetic energy of translation ($10^{-7}$ J). Thus, rotation, in terms of amounts of kinetic energy, is neglected here. However, the rotation of the component should be decreased.

Further, it should be noted from these pictures that the release direction of the die is not perpendicular to the tape. This angle can be up to $\theta$=10°, see Figure 4.12 and Figure 4.15. This angle will affect the placement accuracy. In the ideal situation the die should be transferred perpendicularly to the release surface. The larger the

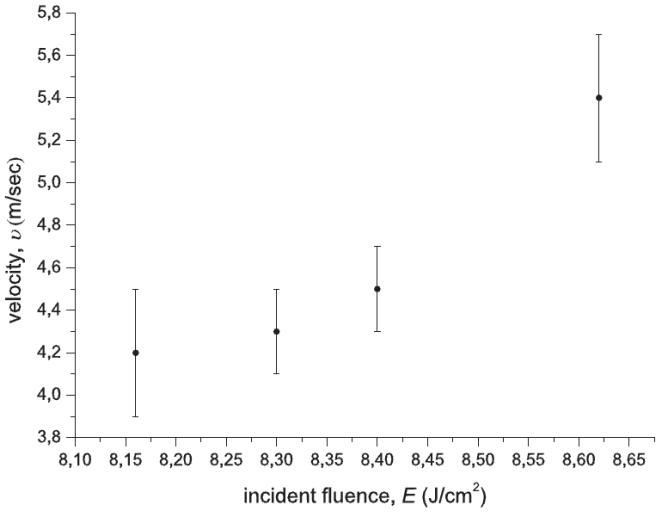


Figure 4.13: The velocity of the released gold-coated dies, previously attached to SWT foil, as a function of the incident energy, in the case of irradiation by 1064 nm wavelength of the Nd:YAG laser.

release angle (the angle between the direction of the die release and perpendicular to the receiving surface), the larger the displacement from the component's desired position will be. From the experimentally determined velocities the fraction of the incident energy which is transformed into kinetic energy can be found. This fraction is termed as coupling efficiency [Hol98]. Here it is calculated as $\eta = \frac{E_k}{E_{in} - E_{thr}}$. This fraction is not constant over the examined range of fluences: that is, it ranges from from 0.15 to 0.30%.

The spot of the focused laser beam used in the described experiments is $5 \times 10^{-4}$ cm$^2$, used spatial profile Figure 4.10 c, while the area of the die's surface is $1.12 \times 10^{-3}$ cm$^2$. Thus, only 45% of the component's area is irradiated. Then, the rotation can be explained by the fact that it is likely to irradiate the die not at the central area of its surface, but in an asymmetric way. Figure 4.14, obtained by a $\times 100$ optical microscope, presents a exemplary case. It is obvious that the sample of picture (a) is asymmetrically irradiated, while the other one, (b), is irradiated closer to its center. This has to do with the spatial distribution of the pulse energy: the darkened area which is observed on the components surface is ablated material which corresponds to doughnut profile on Figure 4.10, c. An uneven energy distribution and alignment mistake caused asymmetrically distributed pressure and, therefore, uneven release propulsion. When using the Gaussian beam (Figure 4.10, a) it was too much energy in the center of the die, but not enough at the periphery - the release was possible, but the die and tape were molten.

The release of this particular type of component using the Nd:YAG Rofin-Sinar 50D is not optimal due to the following reasons:

- the laser beam size is not optimal for this size of the component. Small beam is difficult to align with the center of the die, misalignment causes uneven release

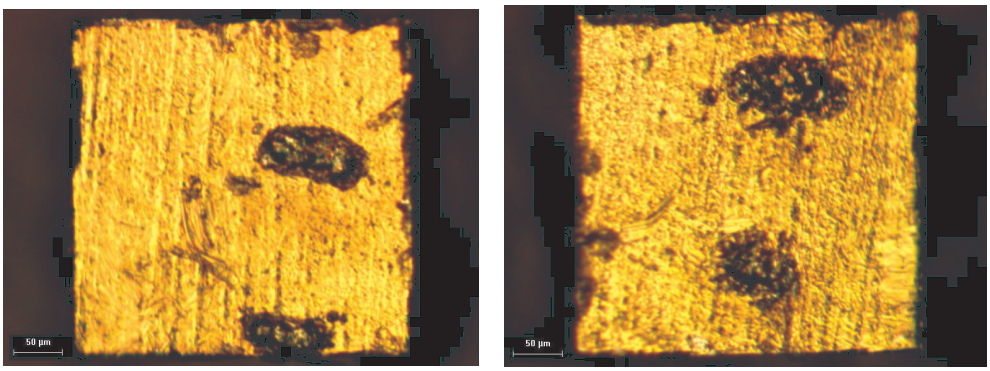


Figure 4.14: The irradiated surface with power density profile of Figure 4.10, c of released gold-coated micro-components. Figures correspond to (a) asymmetrically and (b) closer to the central area irradiation.

and rotation of the die;

- the used power level is the maximum possible for the given laser. This fact limits the the beam's size range: release was not possible to achieve with larger beam size;
- the considered component has a golden bump with a 67 $\mu$m radius. This bump has a mass of $2.4\times10^{-8}$ kg which is comparable with the mass of the die itself ($5\times10^{-8}$) kg. This bump is placed not precisely in the center of the die, see Figure 4.11. The average displacement of this bump from the die center is 7 $\mu$m which adds a moment to the die while release.
- the considered component has a limited application, where the electrical connections are made through the gold surface and the opposite gold bump wire-bonded for I/O operations. This type of component is not suitable for flip-chip or bare die assembly for which the development of laser-induced transfer process emerges.

Using a more powerful laser, larger laser beam size and uniform intensity distribution within the beam, the release process could be improved. However, it is difficult to find the homogenizer or the fiber which could withstand such a high power densities which were used in the experiments. The laser was used already on it's maximum power and adding the available homogenizers will decrease the energy which can be used.

## 4.4 Study of die detachment from the Nitto SWT carrier tape

In the following experiment, release of bare crystalline silicon components has been examined. The release is achieved by irradiation of the IR Rofin-Sinar RS.M-50D Nd:YAG laser, $\lambda$=1064 nm. The laser light propagates through the transparent carrier tape and is absorbed by the silicon, some of the energy goes through the sample. The silicon is rapidly heated and evaporates. Gas pressure causes the release and propulsion of the component. The ablation-induced release process of the bare crystalline silicon components was experimentally examined using the set-up, shown in Figure 4.1.

A die of $300 \times 300 \times 130$ $\mu$m$^3$ attached to carrier tape is irradiated by the Nd:YAG laser, 1064 nm. The component's size is smaller than the beam size in order to cover the whole area of the component, which was achieved with a cavity aperture of 1 mm and a Gaussian spatial profile.

The release process of bare silicon die, recorded by the shadowgraphic imaging (PCO.Imaging SensiCam) is illustrated in Figure 4.15. It can clearly be observed that the die is tumbling during it's flight and that the direction of flight has a release angle of about 10 degrees. In Figure 4.16, the pictures of the flying dies are represented for various incident energy densities. The angle during the release process is found to be around $\pm$4 degrees in about 90 % of experiments. In some cases the angle can be greater then 20 degrees ($\pm$), in about 1% of cases.

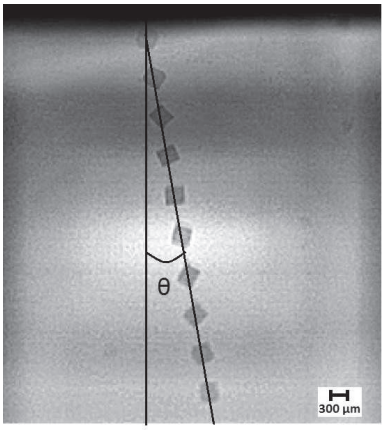


Figure 4.15: Release of a c-Si micro-component from SWT tape, irradiated by Nd:YAG laser, $\lambda$ = 1064 nm. The time between successive frames is 150 $\mu sec$.

From the obtained pictures, the velocity of the released micro-components has been found by fitting of their time-evolved position. Figure 4.17 presents the dependence of the die release velocities on incident laser energy density.

In this case, the experimentally observed energy density threshold for release is $E_{thr} = 3.7$ J/cm$^2$ which is roughly 3 times lower than the gold-coated dies, discussed in section 4.3.

The energy conversion efficiency is again not constant: for the minimum fluence of 3.8 J/cm$^2$ the coupling efficiency $\eta = 0.1\%$ and for maximum of fluence 8.7 J/cm$^2$

$\eta = 0.004\%$.

Figure 4.18 shows that the surface of the irradiated silicon was molten. In this Figure, the laser beam did not cover the whole surface of the die, because a misalignment of the beam with the center of the die occurred. The melting of the irradiated surface can cause thermal damage of the component. Therefore, a simulation model has been developed to study this thermal damage, Chapter 6.

Rotation of the component and release with an angle to the receiving substrate (Figures 4.16) are observed. The conclusion is that despite the decreasing of the misalignment errors by choosing the component's size small, relative to the laser beam size, improving the intensity distribution within the beam, the release is still unstable: non-zero initial angle of the release is observed in all experiments. The possible causes of the release errors are studied in the modeling Chapter 6.

The range of the energy densities which can be used for successful release is wider than in the case of gold-coated dies. The release velocities are quite high with the maximum of 10.5 m/s. It is important to note that these high velocities could cause damage to the component on impact with the receiving surface. Assuming the component strikes the final receiving substrate with the velocity $\upsilon_f$=10 m/sec and all of its kinetic energy is converted to compressive strain within the component itself, then the resulting local strain will be at least of order $\varepsilon = \upsilon(\frac{\rho}{Y})^{1/2}$, where $\rho$ and $Y$ are the density and Young's modulus of the component, respectively and $\upsilon$ is the velocity of the component [Hol98]. For a silicon structure ($\rho$ = 2330 $kgm^{-3}$, $Y$=162.4 GPa with $\upsilon$=10 m/s, this yields $\varepsilon \approx 0.0022$ which is far below the elastic limit of 0.02. The kinetic energy generated on laser release can be dissipated without damage after impact.

The experimental results, where Revalpha tape was used as a carrier, do not differ from the results where STW tape was used: carrier tape material plays negligible role in the ablative-release process.

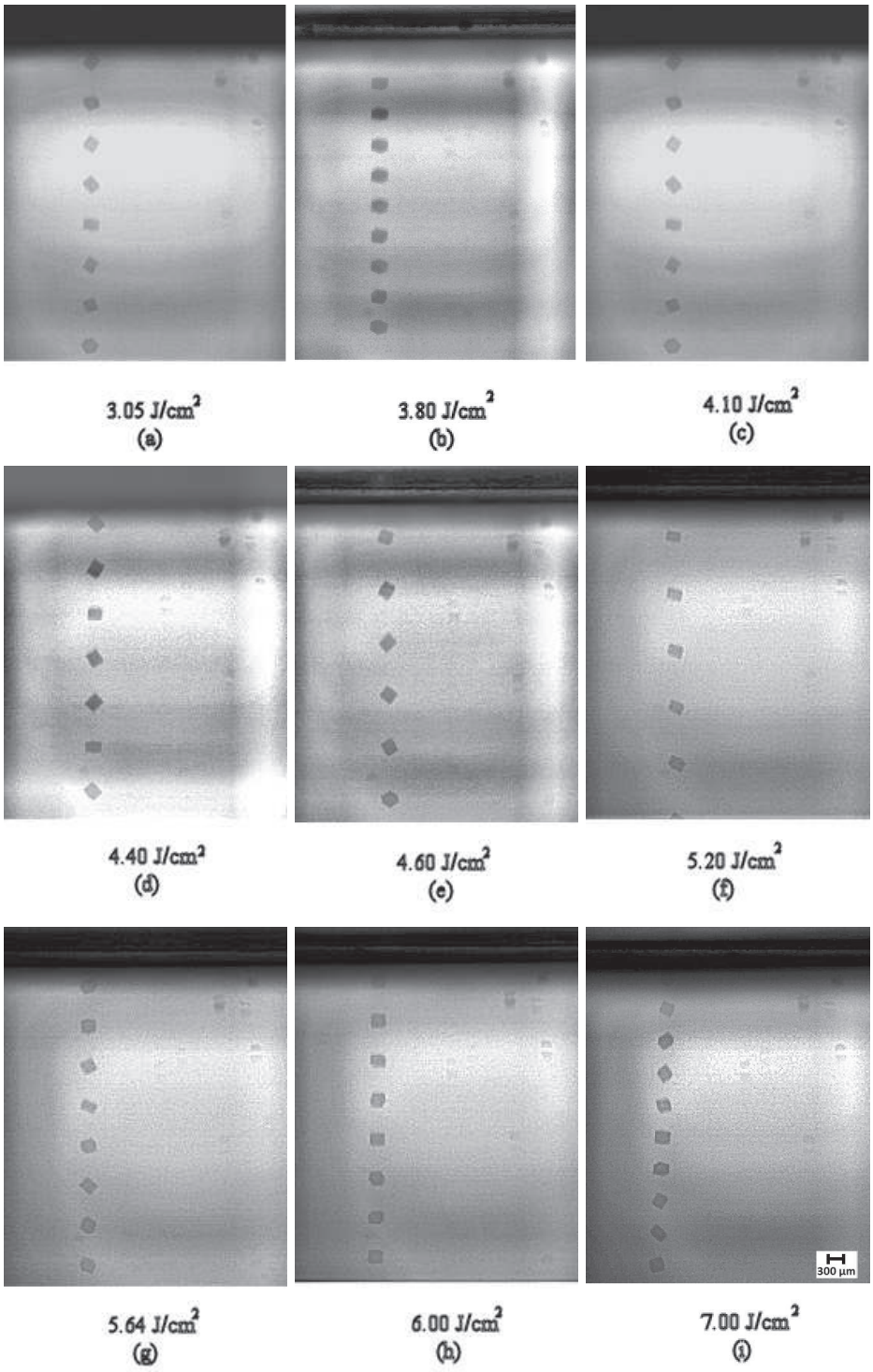


Figure 4.16: Shadowgraphic imaging by the PCO.Imaging SensiCam, of the Nd:YAG laser-assisted release process of c-Si dies, previously attached to SWT foil, for various incident energy densities. The time between two successive frames is (a) 250 $\mu sec$, (b), (c), (d), (e), (f) 150 $\mu sec$, (g), (h) 100 $\mu sec$ and (i),50 $\mu sec$.

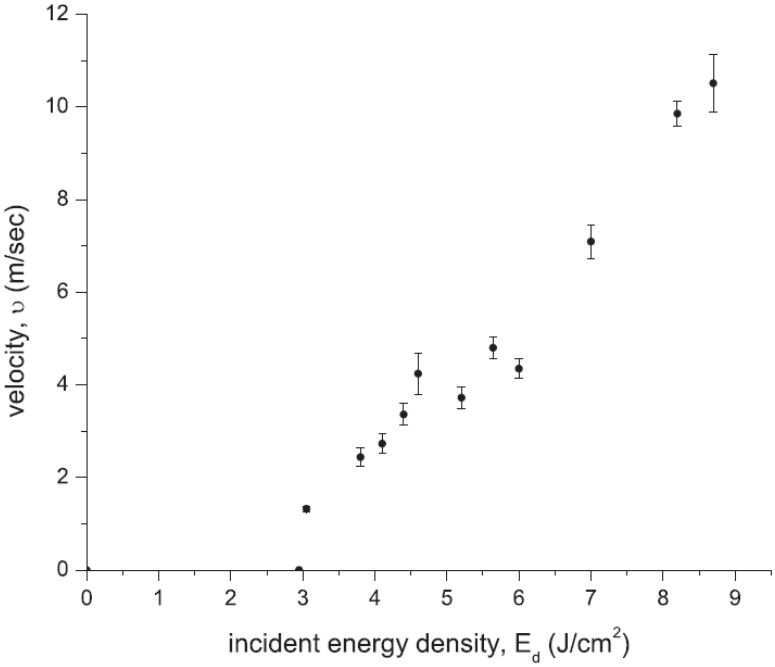


Figure 4.17: The velocity of the released silicon dies, attached previously to SWT foil, versus the incident energy density, in the case of irradiation by the Nd:YAG laser.

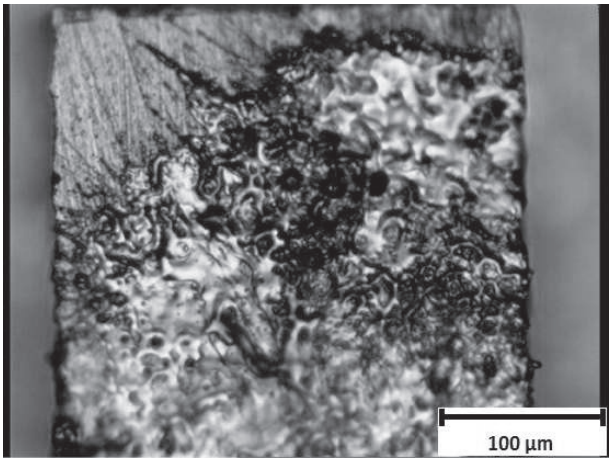


Figure 4.18: The irradiated surface of the released c-Si micro-component.

## 4.5 Discussion

Experiments have been performed in order to investigate the ablation-induced release process.

Both gold-coated silicon components and bare silicon components were used. These types of components were successfully released from the tape carriers using Nd:YAG Q-switched laser irradiation with 1064 nm wavelength. Observations by a high speed camera showed that the components rotated during the release and fly in unpredicted directions, but within ±4 degrees. Experiments show tumbling and a non-zero release angle of the components.

The spatial profile of the laser beam used in experiments with gold-coated dies had a "doughnut" shape with non-equal intensity peaks see Figure 4.10, b: one side of the beam had a higher intensity level. Non-equal intensity causes local overheating of the die, as can be observed in Figure 4.14, and non-homogenous pressure formation and, therefore, non-uniform release. The direction of the die rotation has correlation with the position of the highest intensity peak: all of the dies are flying in one "preferable" direction, see Figure 4.16 . The non-uniform spatial intensity distribution is considered as a main factor which is responsible for the variation in release. A homogenous beam spatial profile is recognized as a main factor which will improve the predictability of the release process.

The improvement of the intensity distribution within the laser beam for Q-switch nanosecond high power lasers is challenging: one possible solution is to use an optical fiber as a homogenizer. The integration of the fiber to this type of lasers is difficult and will cause unacceptable intensity loss: there will not be enough power to initiate the release. A more powerful laser will solve this limitation.

During the experiments with bare silicon dies, a Gaussian intensity distribution was used see Figure 4.10,a. Laser beam size was chosen to cover the die completely. However, the component tumbling and variation of the release angle is observed.

The thermal damage of the die surface, irradiated by the laser, which was caused by melting, (see Figure 4.18) is analyzed and the active layer situated on the opposite side of the die should not become overheated during the release process (see Chapter 6).

Two types of tape were used as a support carrier for the dies: STW Nitto blue pressure sensitive tape and thermally-activated tape Revalpha. In both cases release speed was the same. This can be explained by the fact that the main process responsible for the die release is ablation of the silicon surface.

The ablation-induced release process is one possible approach to release the components from the carrier tape. The tape material does not play a role, which is beneficial for the wafer dicing process: manufacturing does not need to balance between best tape for dicing process versus best tape for the component pick-up process: the best tape for dicing can be chosen.

However, the high release velocity of the components is a factor which caused difficulties during placement on the receiving surface: dies bounced away from it. It was decided to work on decreasing of the release speed and control of the flying dynamics.

# Chapter 5

# Thermal-induced release experiments

## 5.1 Introduction

In these experiments, the combination of the properties of the thermal tape Revalpha and complex mechanism of the silicon absorbtion of the low intensity infrared and green laser irradiation are investigated. The thermal release process differs from ablation release. That is, silicon absorbs the low intensity laser light mainly in the bulk of the component, the surface temperatures are lower than in ablation approach and the main mechanism of the release is gas formation in the contact layer of the tape. This kind of release is not possible to achieve with any other types of carrier tapes. Two laser sources were used during the study:

- Nd:YAG, operating with $\lambda = 1064$ nm, Rofin Sinar RSY 150P, fibre coupled;
- Frequency doubled Nd:YAG $\lambda = 532$ nm, Unitek Miyachi welding laser ML80-50A, fibre coupled;

To complete the investigation, the experiments were performed in order to determine the placement accuracy and to find the factors influencing it. The Nd:YAG laser, with 0.4-1.0 millisecond pulse duration was used first in order to test the release. The other laser source Unitek Miyachi ML80-50A Nd:YAG frequency doubled laser was used in order to investigate influence of the different wavelength on the process of release and to test the influence of the beam homogeneity improvement.

## 5.2 Experimental equipment and set-up for thermal-induced release using 1064 nm wavelength

For the thermal release the IR source was firstly investigated. The Rofin Sinar RSY 150P is a flash lamp pumped laser source which provides a high peak power up to 150 W. The flexible fiberoptic beam delivery and the small focused spot size of the laser beam allow this laser to be successfully applied in many cutting and welding applications. The laser can operate in continuous and pulsed (0.1-20 ms) modes. Beam delivery is done by a optical fibre with 0.6 mm core diameter. Alignment of the laser beam with the target is by using the pilot laser operating at 653 nm. A set-up was built to improve the alignment of the laser beam with the components and to match the size of the laser beam with the size and the shape of the tested component. Another important feature of the set-up is that the assembly process can be easily observed. The principle of the designed and realized experimental setup for the thermal release process is shown in Figure 5.1. A corresponding photo of the set-up is given in Figure 5.2. The laser power goes through the fiber and a collimation

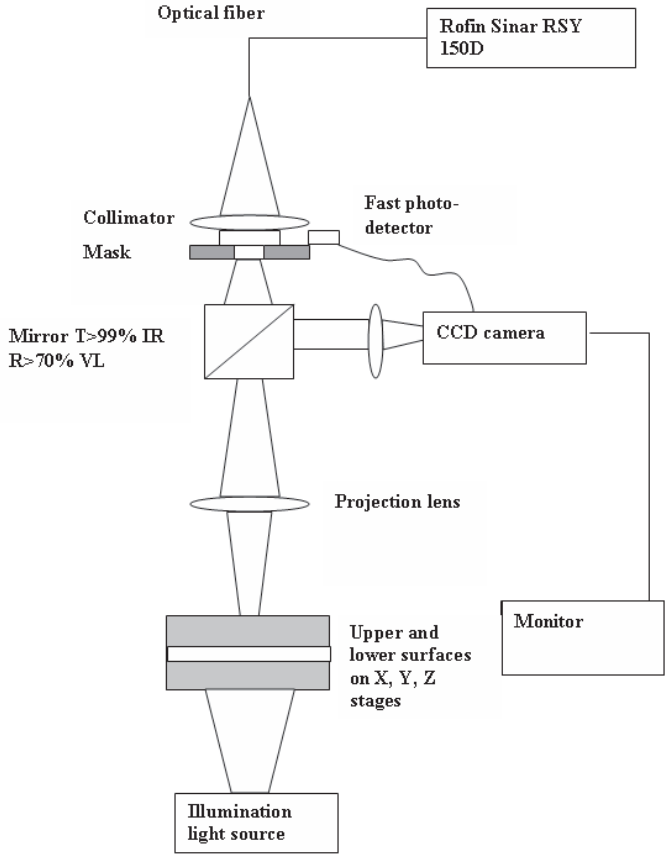


Figure 5.1: Schematic view of the experimental set-up for thermal release experiments

lens which creates the beam spot with diameter equal to 20 mm across the mask. The object to be imaged was a 3×3 mm$^2$ square hole in a plate which the light had to pass through. To create the mask on the quartz plate, covered with a 300 nm thick chromium layer, the area 3×3 mm$^2$ of this layer has been evaporated using UV laser ablation. This mask could not withstand for a long time the used laser intensity and despite it's benefits from optical point of view (limited diffraction on edges due to it's thickness) another mask is used in the assembly experiments: a 2 mm thick Copper plate with a 3×3 mm$^2$ hole in it.

As a collimating lens a lens with $f_1$=58 mm was applied. This was the same lens used as projection lens $f_2$=58 mm. The mask was imaged with magnification of 10:1 to create a square laser beam with 0.3×0.3 mm$^2$ size matching exactly the size of the die so that surrounding dies were not touched. The center of the lenses, as well as the respective focal points are along the symmetry axis of the system. An optical rail, with three carriers, was used for easy alignment of the whole system. Two rail carriers were used for the two lens mountings and a third one was used to mount and slide the object to be imaged along the rail. The camera is triggered by the laser light

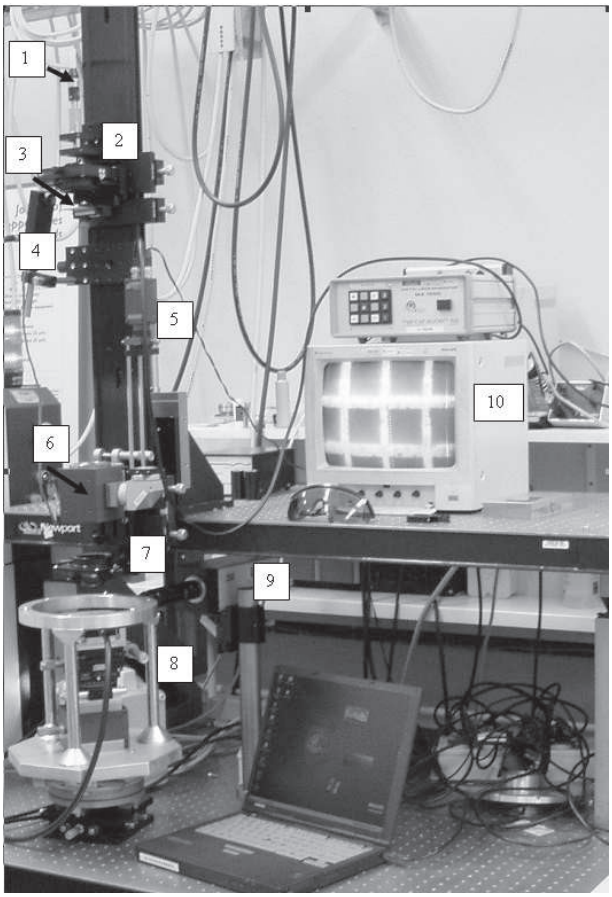


Figure 5.2: The experimental set-up for thermal release experiments: 1. fiber exit; 2. collimation lens; 3. mask; 4. laser signal detector; 5. CCD camera; 6. dichroic mirror; 7. projection lens; 8. targeting system; 9. high speed camera; 10. monitor which is used for alignment and assembly observation.

reflected from the mask by fast photo-detector. The detection system consists of a dichroic mirror that is transparent for the infrared light and reflects the visual light, zooming optics and a CCD camera connected to the computer.

Under the projection lens, the targeting system is placed which consists of the release (upper surface) and receiving (lower surface) substrates brought in the 0.5 mm proximity gap using special holder. The release substrate is a tape with the components on it. It is placed at the image plane of the projection lens. The shadowgraphic images of the components, illuminated from beneath by the light source are seen at the monitor (10) in Figure 5.2. The alignment was achieved by matching the laser beam illumination of the pilot laser with the shadowgraphic image of the component. In the same picture with number (8) the targeting system is shown. The details of this targeting system are shown in Figure 5.3. The upper surface (carrier tape with components on it), placed on a stage which can move in X, Y directions and with

rotation $\theta$ around Z axes for alignment of the component with the laser beam. On the second X-, Y-, Z and $\theta$ stage an independent holder for the lower surface (glass with glue layer) is mounted. Right under lower surface a light source is placed from beneath for homogenous illumination of the working area.

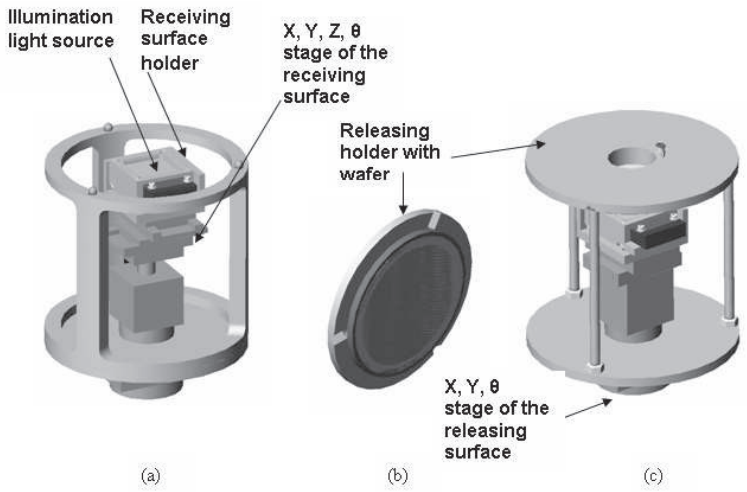


Figure 5.3: Targeting system for placement accuracy investigation, thermal detachment approach: (a) receiving surface holder, (b) release surface, (c) complete targeting system.

The silicon test dies were fabricated from 130 $\mu$m thin wafer. This wafer is diced into 0.3×0.3 mm components using laser cutting. During dicing the wafer is placed on the standard transparent tape. Afterwards dies are re-taped to the single sided Revalpha tape. The lamination of the tapes and re-taping were made manually under atmospheric conditions. During manufacturing, these steps were made in a vacuum environment, using special machines preventing air remaining between the wafer and the tape and provide uniform lamination pressure.

### Laser beam spatial profile measurements

A beam analyzer MicroSpotMonitor of PRIMES GmbH, Germany, was used to quantify the focused laser spot. It resembles a rectangular, uniform intensity distribution. Examples of spot measurements which are done for the described set-up combination: fiber, square mask and projection optics, are shown in Figure 5.4. The spatial intensity profile has on average a uniform distribution, but it shows a significant number of spikes. Some of these spikes are much higher ( 40%) than the average intensity of the beam. These isolated spots of high intensity shift in location from shot to shot, see Figure 5.4. The laser source introduces phase distortion. At the focal plane, these phase variations lead to interference effects with large and uncontrollable illumination non-uniformities. Mode mixing within the fiber does reduce these peaks but they could not be completely eliminated.

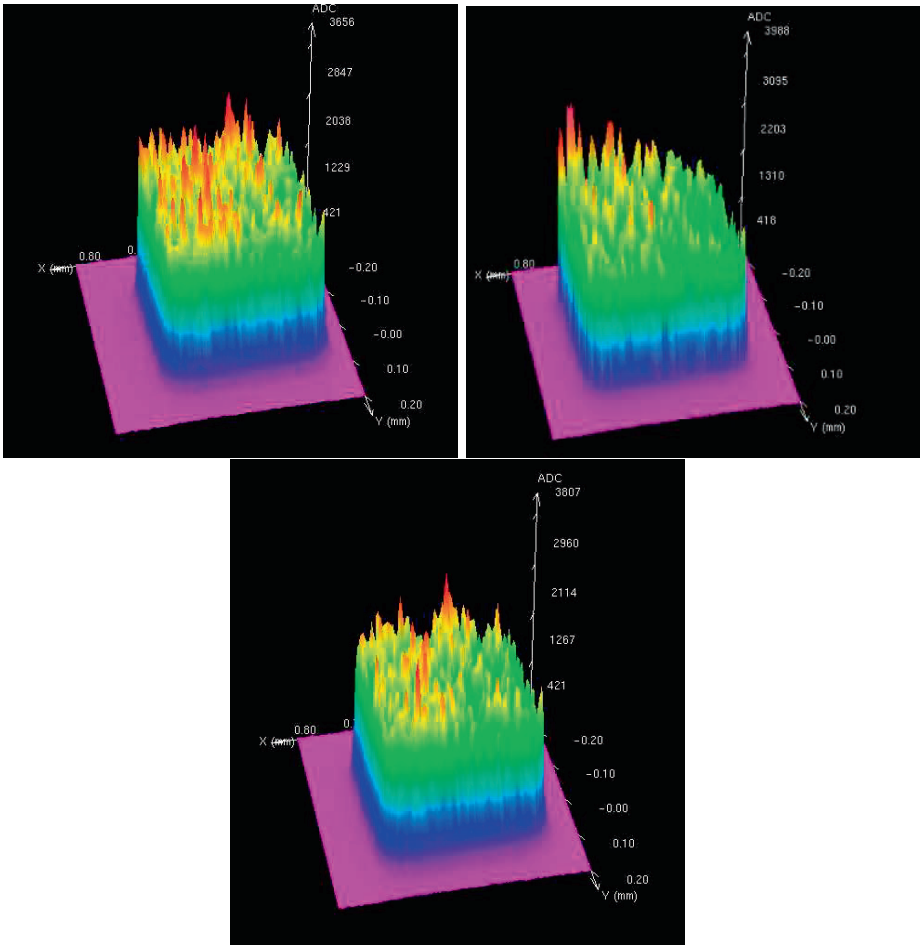


Figure 5.4: Spatial intensity profile Nd:YAG 150P laser beam spot for three different laser shots.

## 5.3 Study of the thermal-induced release crystalline silicon dies from the Revalpha tape using 1064 nm wavelength

It was determined that a relatively low irradiation intensity, $5.5\times10^4$ W/$cm^2$ is sufficient to achieve the release of the die from it's carrier thermal tape (in comparison $6\times10^7$ W/$cm^2$ intensity is used for ablative release).

The pictures which are obtained by shadowgraphic imaging and correspond to energy density E=22.2 J/cm$^2$ are shown in Figure 5.5. The die release velocity is vary a lot: for the same energy density the speed of the flying dies varies from 0.25 to 0.55 m/sec. Random release directions, tumbling and non-zero release angle are clearly visible on Figure 5.5. Following the same procedure as for the ablative release approach and measuring the distance of each frame from a reference plane, the velocities of each die are obtained. The laser energy density has been varied from 22.2 J/cm$^2$ to 82.6 J/cm$^2$. From Figure 5.6 which illustrates the average velocity versus the incident

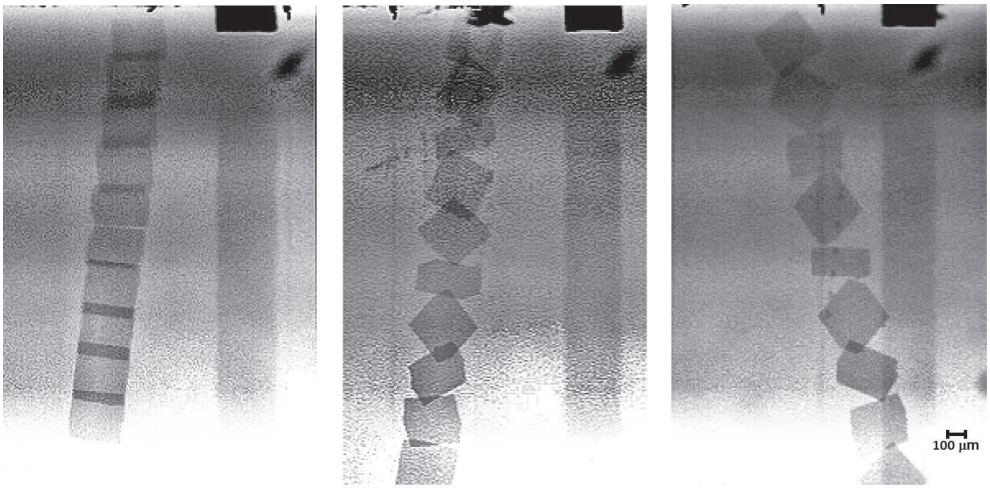


Figure 5.5: Shadowgraphic imaging of the Nd:YAG thermal-induced release process of the silicon dies. The time between two successive frames is 0.5 msec, laser energy density E = 22.2 J/cm$^2$, die dimension is $300 \times 300 \times 150$ $\mu$m$^3$.

energy density. It seems that there is no dependency of the die velocity on the laser energy. There is a large spread in velocities at all energy levels. The release process is much slower then ablative, the observed angle during the release process is $\pm$ 8 degrees. The final kinetic energy of the components is only a fraction of the incident

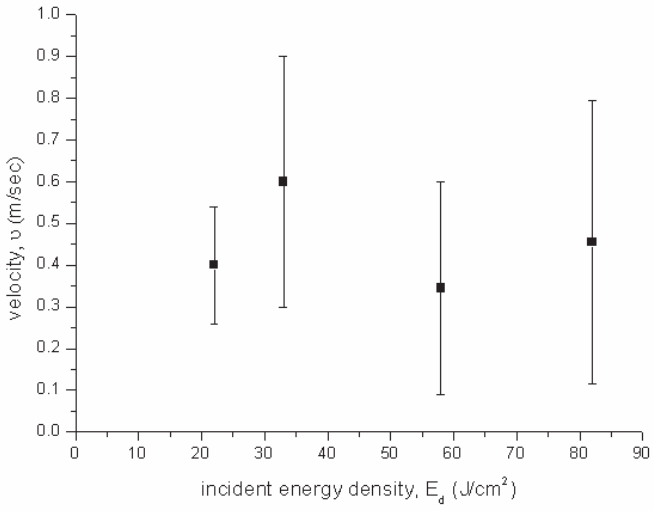


Figure 5.6: The velocity of the released c-Si dies, attached previously to Revalpha foil, depending on the incident energy density, in the case of irradiation by the fundamental harmonic of the Nd:YAG laser, $t_p$=0.4 ms

laser energy $\eta = \frac{E_{kin}}{E_{las} - E_{thr}} = 0.15 \times 10^{-7}$. From comparison with the ablative release where the efficiency was around 0.1% it follows that most of the incident laser energy is going to other processes, like heating of the released component and carrier, heat of vaporization, and lateral expansion of the bubbles inside the glue. Variable speed and angle of the release can be explained with more sensitive and slow process of the gas formation inside the Revalpha bubbles. Even small disturbances in the heating process will result in uneven release. The process will be further investigated and analyzed theoretically in the modeling Chapter 6. Factors which are involved in the process and their weight are discussed there.

### 5.3.1 Placement accuracy investigation

To investigate the factors which have influence on the positioning process, assembly experiments were carried out for the infrared thermal release approach. The carrier (upper wafer) and receiving substrate were stationary with a well-defined proximity gap equal to 0.5 mm. After a single laser pulse the die is released and the picture before and after release was captured. Figure 5.7 shows the CCD camera images of these two stages of the assembly process for two different dies. The dies are on the tape before laser pulse (a), (c) and these dies after single laser pulses landed on the receiving surface are shown in pictures (b), (d). From these images it is clear that

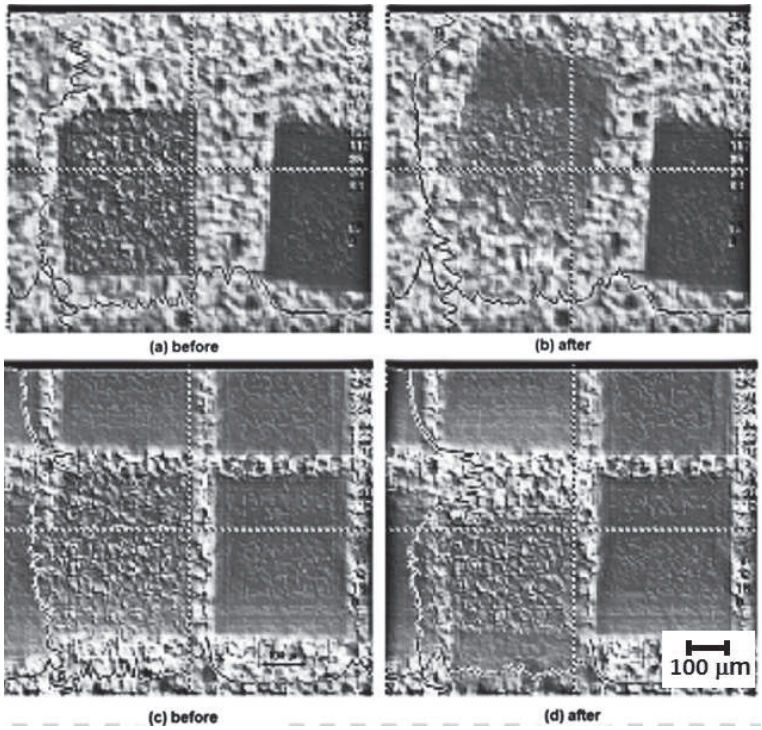


Figure 5.7: Dies ($300 \times 300$ $\mu m^2$) shadow images: Before laser irradiation, dies are aligned with the laser beam (a, (c); After laser irradiation, dies are released and landed on the receiving surface (b), (d)

the released die has a shift in location and, in (b) case, also has rotated during its release. The X-shift, Y-shift, and $\theta$-rotation of the components landed on the receiving substrate have been measured. The shift of die locations is shown on scattering plots in Figures 5.8, 5.9, 5.10.

These plots show the dies displacement for different laser energy densities. Plot (a) represents the displacement of the components at the laser intensity just above the release threshold, $E_d$= 24.4 J/cm$^2$. All components are placed with better than 100 micrometers accuracy. Increasing of the laser intensity to $E_d$= 46.7 J/cm$^2$ introduces worsening of the placement accuracy and precision: almost all components were placed within 200 micrometers. This effect is explained by increasing of the release angle

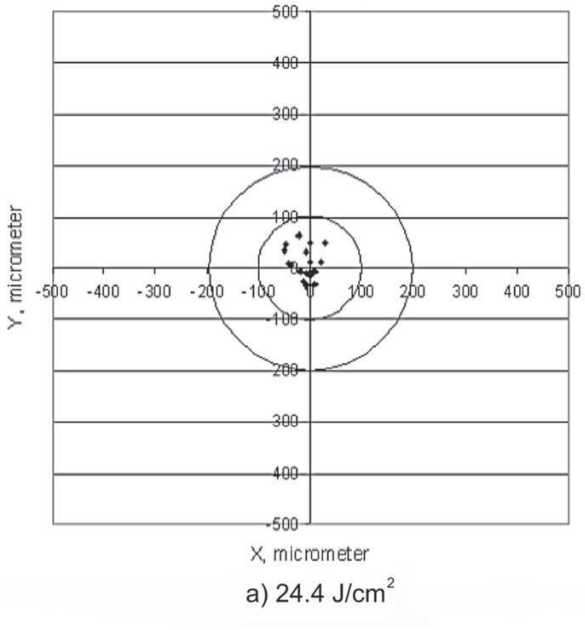


Figure 5.8: Die scattering plots for 24.4 $J/cm^2$ energy density.

with increasing of the energy density level, see Chapter 6 for details. There was no preferable direction observed: the components placement was random. Increasing of the intensity to $E_d$= 67.8 J/cm$^2$ confirms the effect of the increasing placement errors.

The histogram of the measured displacement at the threshold laser intensity is presented in Figure 5.11. According to the histogram 60 % of the components will be placed within the required 35 $\mu$m accuracy.

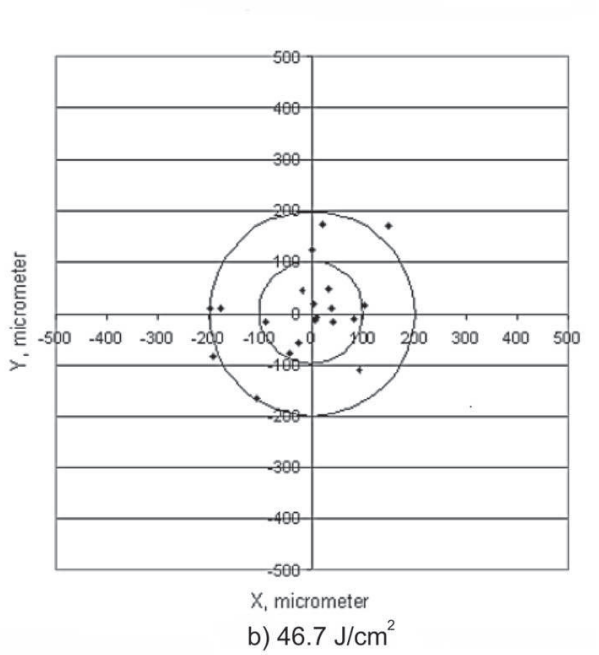


Figure 5.9: Die scattering plots for 46.7 $J/cm^2$ energy density.

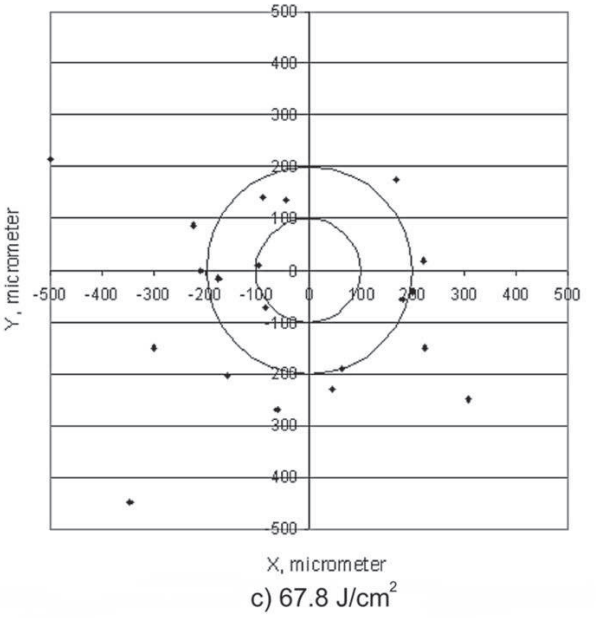


Figure 5.10: Die scattering plots 68.8 $J/cm^2$ energy density.

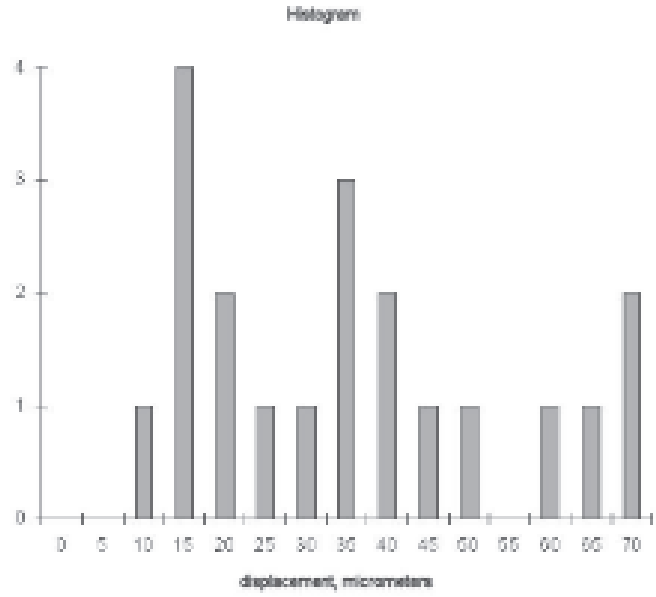


Figure 5.11: Histogram represents the displacement of the released components; $E_d$= 24.44 J/cm$^2$;

The contour plot in Figure 5.12 represents the statistical calculation of the average die displacement for a certain laser pulse length and power density. The lowest displacement occurs at the energy level which is just above the threshold energy of the die release, the lighter area on the plot. With increasing of the power and/or laser pulse width the component displacement is increasing.

The next, experiments were performed in order to check if it is possible to direct the die release by component's partial illumination with the laser spot. Figure 5.13 shows schematically the side view and the top view of components and the laser beam irradiating only a part of the die surface. One half of the die was irradiated by placing the square laser beam at one side of the die surface: (a) on the left part, (b) on right part and (c) opposite to the viewer. Corresponding pictures which were taken with the high-speed camera are shown in Figure 5.14.

Consider Figure 5.14, situation (a): there are two dies on this picture: first die at the left side is for reference only, die at the right side is irradiated by the laser beam. The beam irradiates only half of the die at the left side. The picture represents two images: before the laser irradiation and after 1 ms. The laser energy density was set to $E_d$=62 J/cm$^2$. It is visible that the die is flying to the opposite direction from the illuminated side. Pictures (b) and (c) show the same phenomena. On picture (b) the die right side is irradiated and on picture (c) the front side is irradiated, see Figure 5.13 for explanation. This experiment shows that it is possible to direct the die by positioning the laser beam on the die surface.

To investigate what is happening with the tape surface, after die release, SEM pictures were taken using FEI/Philips XL30 ESEM. In those pictures presented in

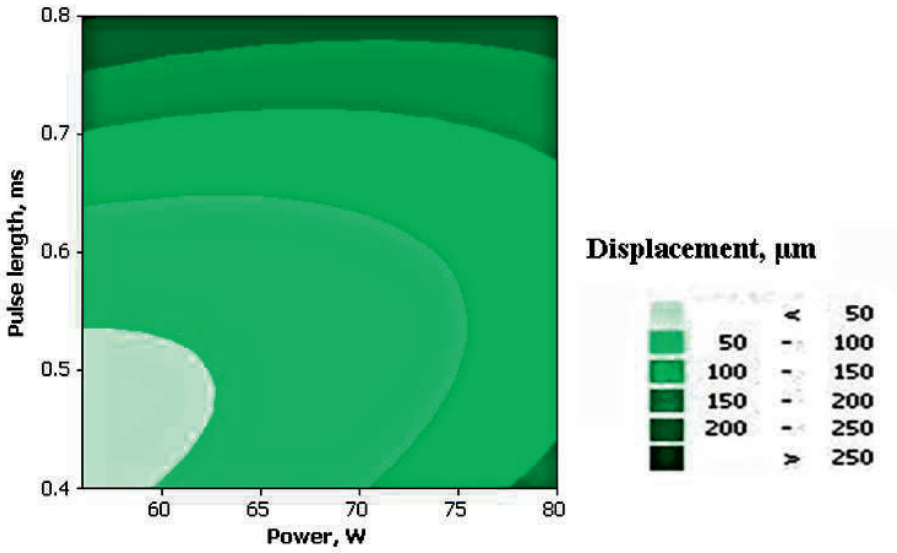


Figure 5.12: Contour plot of die displacement in $\mu$m versus laser pulse time and power.

Figure 5.15 and Figure 5.16 it is visible that, before die release, the surface of the tape is flat and there were no bubbles observed.

After release the tape surface is transformed by the gas bubbles, see Figure 5.15. Modified areas where dies were located before irradiation are clearly visible. The area shown in Figure 5.15 was irradiated with laser energy density equal to $E_d$=82.6 J/cm$^2$. On this picture there are bubbles (pointed with green arrows) and several craters (pointed by red arrows) on the tape surface. Craters appeared after gas bubbles explosion. The surface which is not modified is indicated with yellow rectangles.

In the Figure 5.16 the tape after laser irradiation with threshold laser energy density, $E_d$=22.2 J/cm$^2$ is presented. The quantity and size of the grown bubbles is much smaller then in case of higher irradiation. From these pictures it is possible to draw the suggestion that the bubbles distributed randomly in the tape material and their random size adds the instability to the release behavior as the gas bubbles will explode and push the die non-equally. Another factor which plays a role in the increasing of the release instability is the temperature dependant silicon absorption. For low intensity infrared irradiation it is non-linear: under the room temperature condition the silicon is almost transparent $\alpha = 12$ cm$^{-1}$, by increasing silicon temperature during the millisecond laser pulse the absorption increases exponentially $\alpha = 1.8\exp(T/158)$ cm$^{-1}$. Small changes in starting temperature, intensity peaks which are observed during spatial profile measurements, surface pollution, any small disturbances will cause local heating spots of a silicon die which will affect the release process.

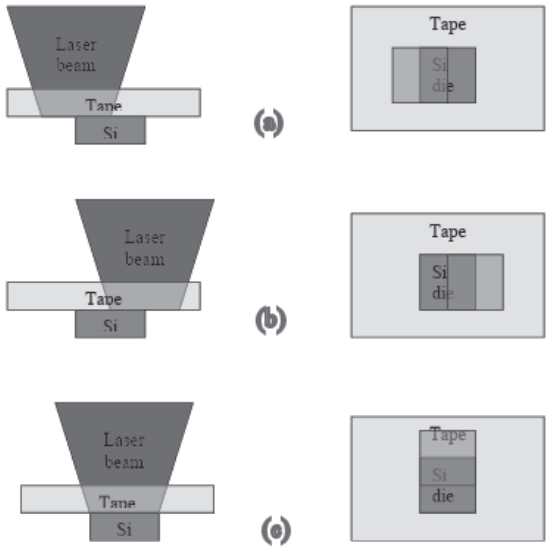


Figure 5.13: Side view and top view of the targeting system for different positions of the laser beam on die surface: (a) on the left part, (b) right part and (c) opposite to the viewer.

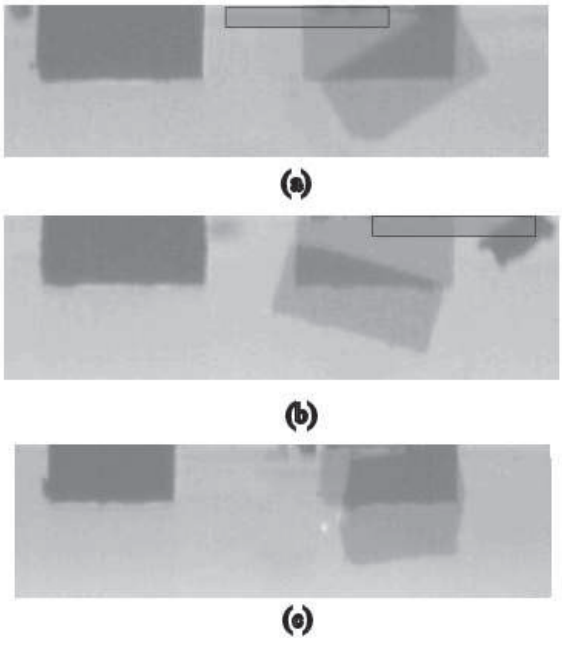


Figure 5.14: Shadowgraphic imaging by the PCO.SensiCam of the Nd:YAG laser-assisted release process of dies irradiated partly (see corresponding pictures in Figure 5.13

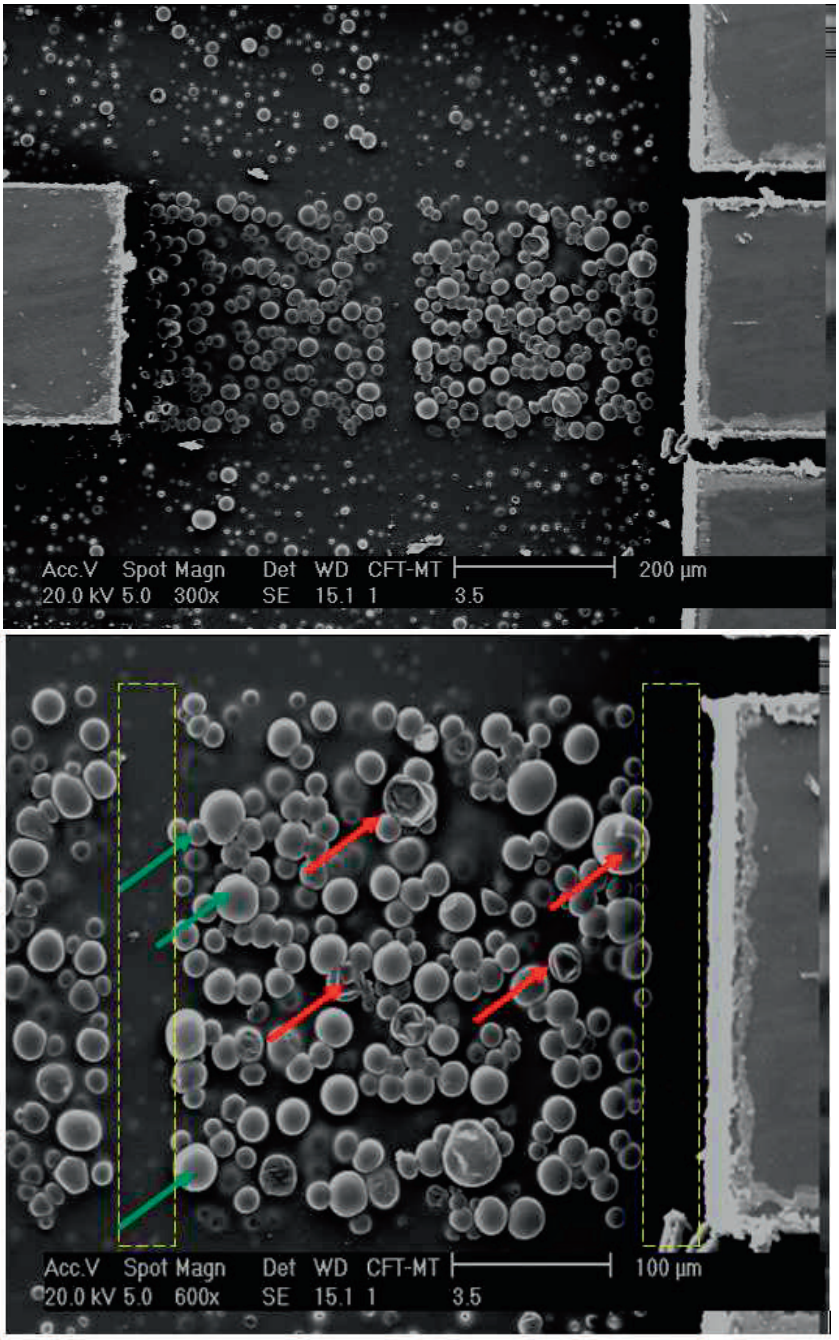


Figure 5.15: SEM image of the Revalpha tape surface irradiated by Nd:YAG laser, $\lambda$=1064 nm, $E_d$=82.6 J/cm$^2$, die dimension is 300 × 300 $\mu$m$^2$. Grown bubbles are indicated with green arrows, craters are indicated with red arrows, unmodified area is indicated with yellow rectangles.

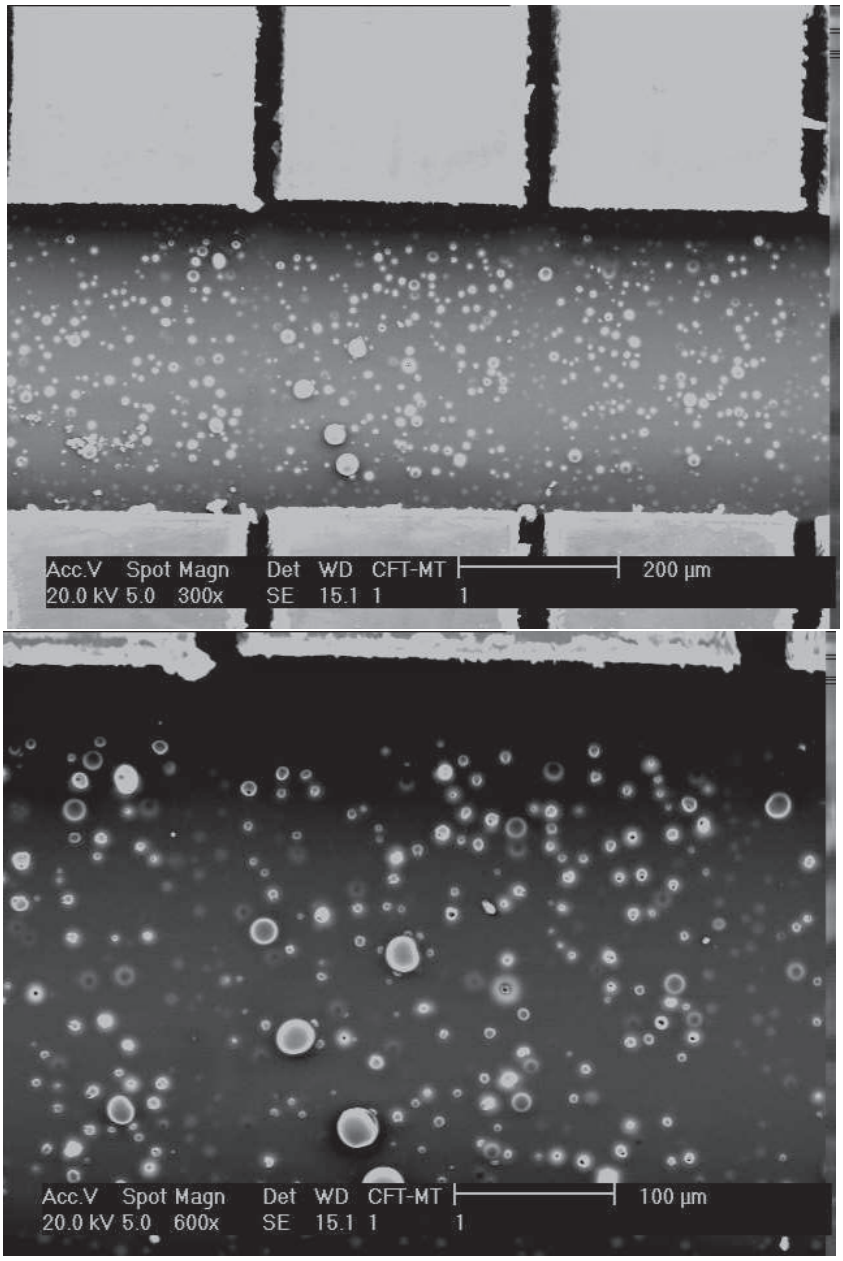


Figure 5.16: SEM image of the Revalpha tape surface irradiated by Nd:YAG laser, $\lambda$=1064 nm, $E_d$=22.2 J/cm$^2$

## 5.4 Experimental equipment and set-up for thermal-induced release experiments using 532 nm wavelength

To overcome the strong non-linear absorption in silicon, experiments with a frequency doubled Nd:YAG laser source have been performed. For a frequency doubled Nd:YAG laser, operating at low intensities ($3 \times 10^3$ W/cm$^2$), the absorption coefficient was found to be $\alpha = 93880 \exp(T/700K)$ cm$^{-1}$ [Sva79]. The initial absorption is high and laser light will be absorbed at the silicon surface. This process provides a better distributed heating over the laser pulse duration because the non-linearity of the heating process is eliminated which gives a more stable overall process.

A Miyachi laser source was used in the so called "green" thermal release experiments. For these experiments average laser intensity $3.8 \times 10^4$ W/cm$^2$ and 0.2 ms pulse duration was used; the laser beam beam diameter was 540 $\mu$m covering the component surface completely. The targeting samples were prepared by placing the components on the Revalpha tape manually.

To study the release behavior, the camera was placed below the targeting system and observed the process from two sides. A mirror was used to take simultaneous pictures, see Figure 5.17.

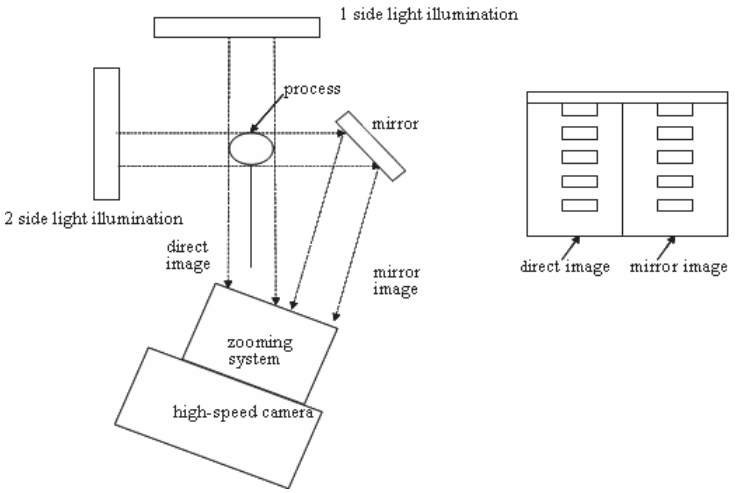


Figure 5.17: The set-up used for the simultaneous recording of the flying die (a); image, recorded by camera (b).

### Laser beam spatial profile measurements

A beam analyzer (PRIMES) was used for laser beam spatial profile measurements. These measurements show a relatively smooth beam homogeneity without local peaks, see Figure 5.18. However, there is an asymmetric area within the beam where intensity is approximately 10% lower.

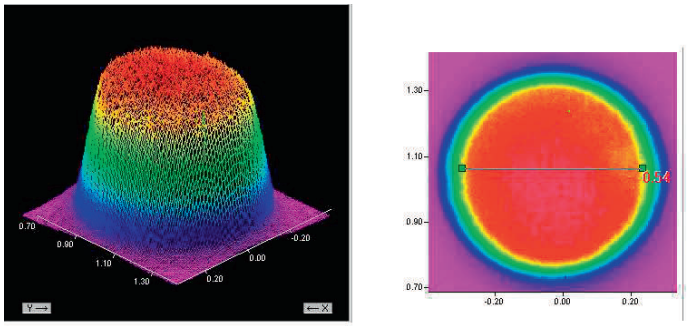


Figure 5.18: Spatial intensity profile of the Miyachi green laser operating at 532 nm wavelength, mesured by the PRIMES

## 5.5 Study of the thermal-induced release crystalline silicon dies from Revalpha tape using 532 nm wavelength

The "green" release approach was found to be the most optimal process for the component release. There are several advantages of this process. First, the effects of the non-uniform heating is decreased due to the fact that green laser light is absorbed preferentially in the silicon surface, not in the bulk of the component, as was the case of infrared irradiation. This fact makes the release process less sensitive to the disturbances in the component heating. The second fact is the quality of the beam profile which in case of the green Miyachi laser showed a homogeneous spatial profile.

However, during experiments it was observed that components had a "preferred" direction of the release. In Figure 5.19 it is shown that the components released mainly to the left. The velocity variation for each energy density is a factor of 2 less then in case of die release using IR laser. To that end compare Figure 5.6 for release using IR Rofin Sinar Nd:YAG laser to Figure 5.20 for the release using the green Miyachi laser. This characterizes the "green" process as a more stable. The speed of the released component varied from 0.7 to 1.1 m/sec, which is low in comparison with ablation release.

The coupling efficiency (part of the applied energy that is converted into die kinetic energy) $\eta$=1×10$^{-6}$, which is two orders of magnitude higher when compared to the efficiency of the thermal "infrared" release.

The optimum laser power and pulse duration for stable release was determined. The best condition (lowest release angle and minimum tumbling) was observed at laser irradiation with the minimum pulse duration of the used laser system, which was 0.2 ms and 32 W laser power. Pictures of the process made with a high-speed camera are shown in Figure 5.21. It might be expected that shorter pulses will give even better results but this falls outside the scope of the current experimental facilities.

The release angle was analyzed for direct and mirror images and represented in the histogram, Figure 5.22. Components released with E$_d$= 14.8 J/cm$^2$ and the gap between the receiving and release surface was assumed to be 0.5 mm. Displacement in X direction corresponds to the release angle (direct view) and Y direction corresponds to angle of the release captured using the mirror view. From the left histogram which represents measurements of the flying angle in one side of the observation - direct view

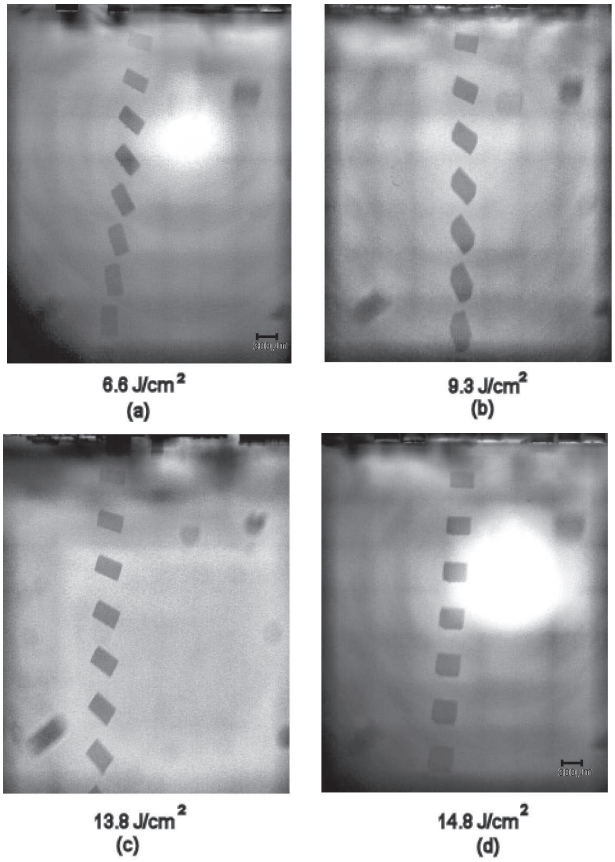


Figure 5.19: Shadowgraphic imaging by the PCO.Imaginh SensiCam of the Nd:YAG doubled frequency laser assisted release process of c-Si dies for various energy densities. The time between successive frames for (a) and (b) is 500 $\mu$sec; for (c) and (d) 400 $\mu$sec.

- it is clear that the angle variation has shifted from perpendicular direction to the left side. This result shows a good correlation with the beam asymmetrical profile. This confirms again that a symmetrical, uniform beam profile is the most important factor which influences the release direction. To estimate the component placement accuracy let's assume that the gap between the component and the receiving substrate is 0.5 mm. Then components, which are released within the angle $\pm 4$ deg, will be placed on the receiving surface within 35 $\mu$m accuracy which is suitable for most applications. This release angle is considered as an specification and represented as the vertical lines in the histograms, see Figure 5.22. Components, which are released with a larger angle, will be rejected. It was calculated that 75% of the components will land within the specification of 35 $\mu$m. By decreasing the gap between the die surface and the receiving substrate down to 0.2 mm, the allowed release- angle becomes 9 degrees. With this release angle 95% of the components will be placed with 35 $\mu$m accuracy. This accuracy meets the requirements for a wide area of the micro-assembly.

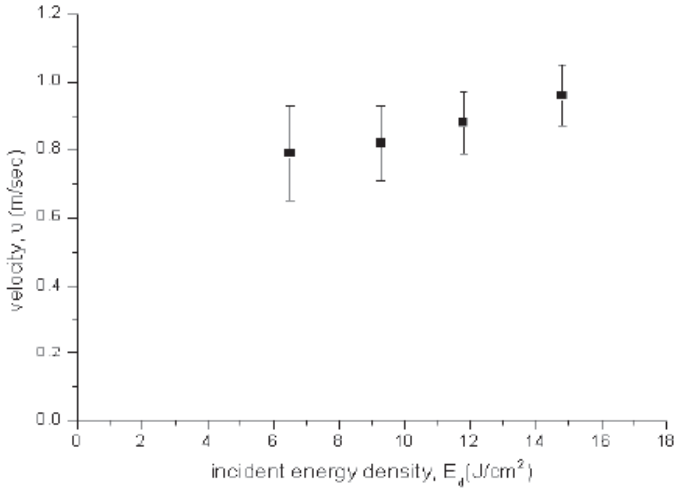


Figure 5.20: The velocity of the released c-Si dies on Revalpha, depending on the incident energy density, Nd:YAG laser $\lambda$=532 nm

## 5.6 Discussion

The thermal induced release processes were examined. The bare silicon components were placed on the special thermal tape Revalpha and the components were successfully released from the tape using Nd:YAG laser low intensity irradiation with 1064 nm and 532 nm wavelength. Observation by a high speed camera shows that the release behavior of the components irradiated with 1064 nm laser light was very unstable. The speed of the released die was relatively low. The overall slower process showed less tumbling and smaller release angle of the components.

The spatial profile of 1064 nm laser showed intensity peaks at random position. Non-equal intensity causes local overheating of the die. The process became more unstable with temperature rise as the silicon absorbtion is highly temperature dependant. This increases the temperature resulting in local overheating and non-equal gas formation in the thermal tape. The gas bubbles which are situated initially in the tape material grow faster on sites where the silicon is overheated. Then, pressure formation became unequal and pushed the die in different directions for each released die. This causes random release directions and relative large variety in the release speed, for the same intensity. However, in general the process is slower and appeared to be more stable than in case of ablative release. An inhomogeneous temperature rise in the component can hardly be overcome due to the nature of the silicon absorbtion of the low intensity IR light.

The release which was achieved with green Miyachi laser with 532 nm wavelength showed the best release process: low velocity, minor tumbling, small release angle which corresponds to the die placement accuracy within the specification. It is assumed that improvement of the intensity distribution within the laser beam will further improve the release stability.

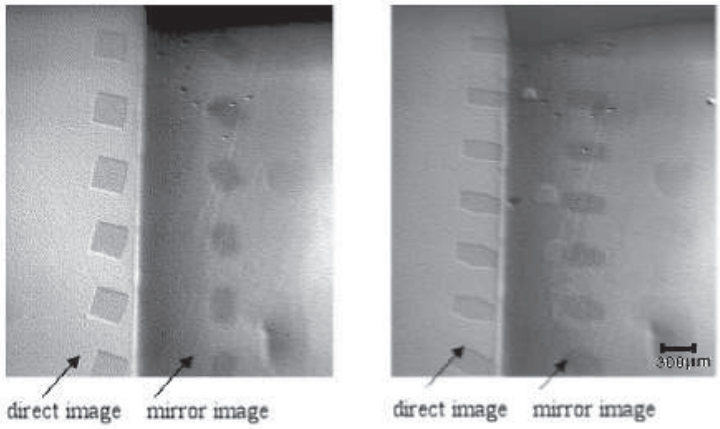


Figure 5.21: Simultaneous shadowgraphic direct and mirror images Nd:YAG laser release process $\lambda$=532 nm. The time between two successive frames is 700 $\mu$sec

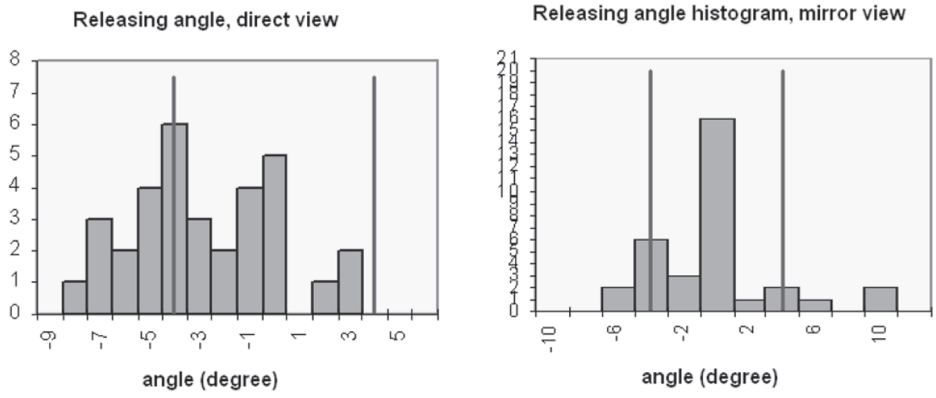


Figure 5.22: The histograms for the component release angle, direct and side view.

# Chapter 6

# Modeling

## 6.1 Introduction

In this chapter, a 2D Finite Element Method (FEM) model, based on work by D.F. de Lange carried out at the University of Twente is introduced. It was used to model the phenomena observed during the experiments. The goal of the simulation is to better understand the process and to find the process window of the die release process: the laser fluence between the release threshold and laser fluence at which the thermal damage of the die occurs. Ideally, the laser beam is absorbed in the silicon without any mechanical and thermal damage of the active electronic circuit. The temperature limit for the thermal damage of the active area is assumed to be 673 K. This is the oven temperature in the reflow step of the conventional manufacturing process. This temperature is considered as the allowable safe limit, although it might be that components could resist higher temperatures. Second goal of the model is to investigate the process sensitivity to the key laser parameters for both release approaches.

In the model a three-layer structure is considered: the tape, as the first layer, the second layer is the glue, which holds the die on the tape, and the third layer, which consists of the silicon die.

The model description consists of four parts. In the first part the radiation calculations are described, Section 6.2. In this section the physics behind the absorption of the laser irradiation, (paragraph 6.2.1) and the implementation in the simulation model, (paragraph 6.2.2) are described.

Section 6.3 describes the heat transfer in the three layer structure; silicon evaporation in the case of ablative release, (paragraph 6.3.1) or gas formation in the case of thermal release, (paragraph 6.3.2). The process of the die release and the flight dynamics of the die are described in Section 6.4. Model implementation is described in Section 6.5.

Section 6.6 presents the simulation results. In paragraphs 6.6.1 and 6.6.2 we present and discuss the calculation results for ablative and thermal approaches, respectively. These results are analyzed in comparison with the experimental data as discussed in Chapter 4 and 5.

## 6.2 Radiation

### 6.2.1 Absorption mechanisms in silicon

From the transmission measurements in Chapter 5, it was found that for the wavelength range from 532 nm to 1064 nm, the absorption in both carrier tapes is negligi-

ble. The first assumption of the model made here is that the absorption of the laser irradiation takes place only in silicon.

No plasma is considered in the model, because at fluences and laser pulse widths which were used in the experiments, no plasma ignition is possible. This is confirmed by the rule of plasma formation, which is states that plasma occurs when [Phi88]:

$$I\tau^{1/2} \geq B \tag{6.1}$$

where B$\approx 4\times10^4[W\cdot s^{1/2}\cdot\mathrm{cm}^{1/2}]$ is the laser-target coupling coefficient and where $I$ is the single pulse laser intensity [W/cm$^2$] and $\tau$ is the pulse duration [sec]. This formula was established for surface absorbing targets irradiated by ns or longer pulses [Phi88]. The peak intensity was found at which dense plasma formation mediates laser-target coupling. Only at the highest fluence used in the ablative approach, 9 J/cm$^2$, see paragraph 6.2.2, could be considered to ignite the plasma, but as it will be shown, below this fluence it is already beyond the die thermal threshold of 673K.

There are five distinct mechanisms for the absorption of light by semiconductors [Jel84]:

1. Photons with energy ($h\nu$) much lower than the band-gap energy ($E_G$) can excite lattice vibrations directly.

2. Free (or nearly free) carriers can be excited by absorption of light with $h\nu < E_G$; such carriers will always be present as a result of finite temperatures.

3. An induced metallic-like absorption due to free carriers, generated by the laser radiation.

4. For photon energies $> E_G$, absorption will take place by direct and/or indirect (photon-assisted) generation of electron-hole pairs.

5. Absorption induced by broken symmetry of the crystalline lattice.

The first mechanism will play a significant role for laser irradiation in the wavelength range corresponding to lattice vibration; for example, $CO_2$ laser radiation at $\lambda$=10.6 $\mu$m couples very efficiently to lattice vibrations of any material. The second mechanism is involved in the absorption of laser radiation of all wavelengths, but is particularly crucial for laser photon energies less than $E_G$ in indirect band semiconductors such as silicon. The effects of temperature on the linear absorption coefficient $\alpha$, for photon energies $h\nu$ near $E_G$ for silicon, involves primarily temperature-dependent band structure effects. This mechanism has little effect on the increased density of free carriers as the temperature is raised. The third mechanism will produce an intensity-dependent $\alpha$ and is important at high photon densities, especially for the wavelength near the indirect band gap in silicon and/or for short duration pulses. The largest contribution to $\alpha$, for irradiation with $h\nu > E_G$ in indirect band semiconductors is mechanism 4. The strong temperature dependence of the absorption coefficient comes through this mechanism (because of the temperature dependence of $E_G$) and not through the second mechanism.

The silicon bulk absorption coefficient strongly depends on temperature, wavelength and incident intensity, resulting in a strong nonlinear behavior.

There are a number of free carriers in silicon at room temperature. They absorb part of the laser energy and pass the energy to the lattice. As the temperature increases some more free carriers are generated. However, if we assume this is the only

absorption process, then we can not explain the exponential increase of local temperature in our ablation-induced release experiments, since silicon is almost transparent at a room temperature for Nd:YAG laser irradiation at 1064 nm wavelength [Sva79]. Basic temperature calculations show only a few degrees heating of the silicon for the ablative-induced process and we observed that the silicon surface melts.

To explain the experimental results, an intensity dependent absorption needs to be introduced (according to the third mechanism). The photon energy of Nd:YAG laser light operating at 1064 nm is approximately the same as the indirect energy gap of silicon. This condition is very important, because free carrier absorption (FCA) arises. This phenomenon describes a carrier generation mechanism which is far more efficient than heating due to lattice absorption [All95]. Every absorbed photon generates an electron-hole pair. The rate of generation of carrier pairs by the FCA mechanism in a semiconductor is proportional to the local irradiance [Lie82]. Experimental studies [Ugl81] show that for 1064 nm at an intensity of $10^7$ W/cm$^2$ in silicon, the free carrier concentration rises to $10^{20}$ cm$^{-3}$ within $10^{-10}$ sec, the absorption coefficient becomes $10^4$ cm$^{-1}$ at the same time. The contribution to $\alpha$ of nonlinear temperature-dependent absorption is almost insignificant for high-intense $10^7$ W/cm$^2$ laser irradiation, which was used in ablation experiments. Therefore a constant absorption coefficient $\alpha_{FCA} = 10^4$ cm$^{-1}$ is used in calculations, which means that absorption takes place at the silicon surface.

Therefore, the total absorption coefficient is defined as a sum of the intensity-dependent free carrier $\alpha_{FCA}(I)$ and temperature dependant lattice absorption $\alpha_L(T)$:

$$\alpha(T, I) = \alpha_{FCA}(I) + \alpha_L(T) \tag{6.2}$$

### 6.2.2 Implementation in the simulation model

For thermal-induced release processes, which is achieved with low-intensity pulses of $5 \times 10^4$ W/cm$^2$ of Nd:YAG laser operating at 1064 nm, the absorption takes place according to the second mechanism described in the previous section. In this case silicon bulk absorption is dominant and the absorption coefficient, which is used in calculations, is temperature dependant: $\alpha_L(T) = 1.8e^{(T/158)}$ cm$^{-1}$.

The reflectivity and the absorption coefficient determine the amount of laser intensity absorbed within the material. The diminution of the irradiance at depth $x$ by a normal incident beam of irradiance $I$ is, according to Lambert-Beer's law,

$$\frac{dI}{dx} = -\alpha(1 - R)I, \tag{6.3}$$

where $x$ is the direction of light propagation $R$ is the reflectivity coefficient of the material. From this partial differential equation the local intensity $I(x, y, t)$ has to be solved.

The boundary condition for this differential equation is:

$$I(x = 0) = (1 - R)I_0(y, t), \tag{6.4}$$

where $I_0$ $(y, t)$ is the incident laser fluence, $t$ is time and $y$ is direction perpendicular to the light propagation.

In case of ablative release, initiated by 1064 nm laser irradiation and thermal-induced release, initiated by 532 nm laser irradiation, the first term $\alpha_{FCA}(I)$ is dominant in equation 6.2.

For ablative release the initial absorption is equal to $10^4$ cm$^{-1}$. In case of thermal "green" release the absorption coefficient is calculated according to: $\alpha_L(T) = 93880e^{(T/700)}$ cm$^{-1}$ [Sva79]. Assuming constant $\alpha$ the optical penetration depth $l_{alpha}$ can be calculated from from Lambert-Beer's law:

$$\frac{I}{I_0} = e^{-\alpha l_{alpha}}, \tag{6.5}$$

where $I_0$ [J/cm$^2$] and $I$ [J/cm$^2$] are fluences of the incident light and the transmitted light, respectively.

In other words,

$$l_{alpha} = \frac{1}{\alpha}, \tag{6.6}$$

In both cases, the initial absorption coefficient is so high and penetration depth is so small (1 micrometer for ablative IR release and 7 micrometers for thermal green release) that, silicon surface absorption of the irradiation will dominate the process. In this case equation 6.3 is not solved by assuming that the irradiation in the model is a function I(y,t) and applying it as an heat source on the interface.

## 6.3 Heat transfer

Ablative and thermal release can be described as either one of two processes: silicon surface evaporation in case of high intense laser irradiation (at $10^7$ W/cm$^2$) and tape gas formation, in case of low laser irradiation (at $3 \times 10^3$ W/cm$^2$). Considering thermal release, the temperature field in the three-layers structure, can be calculated by solving the heat conduction equation with appropriate boundary conditions:

$$\rho \cdot c_p \frac{dT}{dt} = \nabla \cdot (k(T)\nabla T) + q, \tag{6.7}$$

where $\rho$, $[kg/m^3]$ is the density of the material, $c_p$, $[J/kgK]$ its specific heat and $k$ $[W/mK]$ its thermal conductivity. $T$ [K] is the 3D temperature field in the material and $q$, $[W/m^3]$ is a volume heat source. These equations are solved for all three layers: carrier tape base material which is made of polyethylene terephthalate (PET), the glue layer and the silicon die, see Figure 6.1.

For silicon $q$ is represented as the bulk absorption of the low intense laser radiation:

$$q_{Si} = I\alpha, \tag{6.8}$$

where $\alpha(T, I)$ is temperature and intensity dependent radiation absorption coefficient. At the right side of the silicon die, $x = h$, where the $h$ is the die thickness, there is thermal insolation:

$$-k\frac{dT}{dx}\bigg|_{x=h} = 0. \tag{6.9}$$

At the left side, $x = 0$ there is a continuity of the temperature and the heat fluxes: the heat flux is in balance with the flux that "escapes" to the glue layer:

$$k_{glue}\frac{dT}{dx}\bigg|_{glue} = k_{silicon}\frac{dT}{dx}\bigg|_{silicon} \tag{6.10}$$

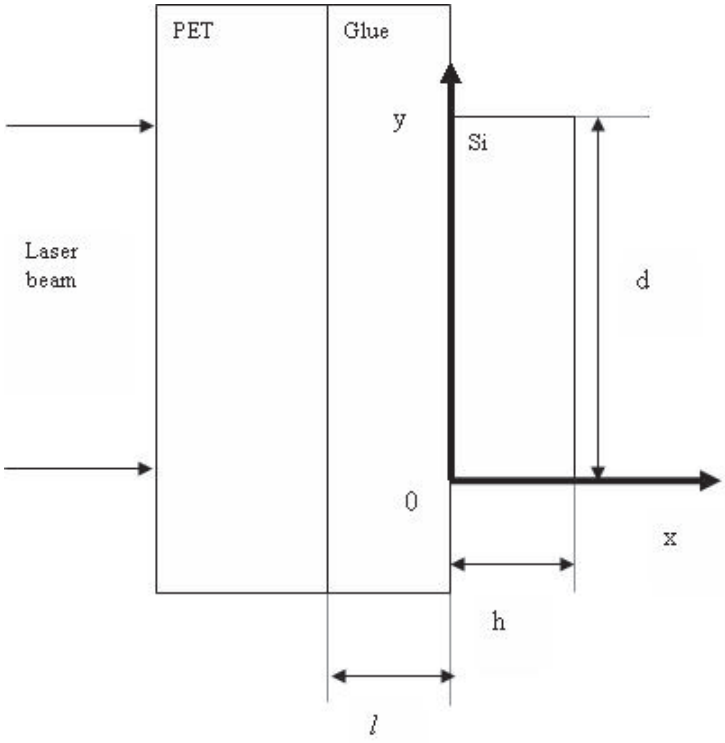


Figure 6.1: Schematic view of the three-layer configuration and coordinates system.

The initial temperature of the layers was set to:

$$T_{(t=0)} = T_0 = 300K. \tag{6.11}$$

The heat source for the glue layer originates from a chemical reaction in the gas bubbles, which are supposed to be homogenously distributed within the layer. This process can be endothermic or exothermic and can be written as

$$q_{glue} = C_{cal} R_p, \tag{6.12}$$

where $C_{cal}$, $[J/mol]$ is a coefficient which represents an amount of heat generated for the production of one unit of gas and $R_p$, $[mol/(m^3\ s)]$ is a production rate. The details of this equation will be described in the Section 6.3.2.

### 6.3.1 Silicon evaporation

In case of ablative release, $q_{Si}$ and $q_{glue}$ are equal to zero, the radiation is absorbed in the surface. Therefore the heat source $q$ is considered to be a surface heat source exactly on the glue - silicon interface. The heat balance at the boundary

$$k_{glue} \frac{dT}{dx}\bigg|_{glue} - k_{silicon} \frac{dT}{dx}\bigg|_{silicon} = q_{deposition} \tag{6.13}$$

where $q_{deposition}$ is the net heat deposited at the interface.

The heat flux toward either of the layers (left hand side terms) is equal to the net heat flux. The net deposited heat flux is the absorbed heat flux reduced by the latent heat associated with the evaporation of silicon.

The temperature at the surface of silicon $x = 0$ is used to obtain the evaporation heat flux $q_v$, [Lan04]

$$q_v = H(T)\phi_e = 0.82H(T)p(T)\sqrt{\frac{m}{2\pi k_B T}}, \tag{6.14}$$

where $\phi_e$ [kg/sec] is a evaporated mass flux and $H(T)$ is the heat content of the material [J/kg], $m$ is the molecular mass and $k_B$ [J/K] is Bolzmann's constant. The factor of 0.82 compensates for the fact that, part of the evaporated particles return to the surface [Sch05]. Finally, $p(T)$ is the equilibrium vapour pressure, which is described by

$$p(T) = p_0 \exp\left(\frac{L_v}{R_s T_b}\left(1 - \frac{T_b}{T}\right)\right) \tag{6.15}$$

where $T_b$ [K] is the boiling temperature at atmospheric pressure $p_0$ [Pa], $L_v$ is the latent heat of evaporation [J/kg], and $R_s$ is the specific gas constant. The recoil pressure $p_r$ working on the surface is about half of the saturated vapour pressure [Lan04]

$$p_r = 0.55p(T). \tag{6.16}$$

The pressure $p_r$ is the pressure caused by the escape of the silicon-vapour from the die surface, and it is the pressure which pushes the die.

With equations ( 6.14) and ( 6.15), the heat lost due to evaporation can be rewritten as

$$q_v = 0.82H_{Si}p_0 \exp\left(\frac{L_v}{R_s T_b}\left(1 - \frac{T_b}{T}\right)\right)\sqrt{\left(\frac{m}{2\pi k_B T}\right)}, \tag{6.17}$$

in which the ratio $(L_v)/(R_s T_b)$ is a Trouton constant and equal to 14 for silicon, [Yoo00].

The net heat source was calculated using:

$$q_{deposition} = I(1 - R(T)) - q_v, \tag{6.18}$$

where $R(T)$ is temperature dependant reflection of silicon.

### 6.3.2 Gas formation in the glue layer

In case of the thermal release approach, gas formation takes place in the glue layer. The glue layer closest to the silicon surface ($x$=0) starts to heat up due to the conduction of heat from the silicon. At the start of the process, there are already some cavities or bubbles, in the glue layer filled with gas. According to information from the tape manufacturer, the gas fraction is equal to 0.16 [Den08]. That means 16 percent of the glue volume is gas. Hence, the initial gas fraction $G_f$=0.16 is a model constant. Below the activation temperature $T_a$, [K], the gas bubbles inside the glue are stable and the adhesive force of the glue is constant. Once the temperature reaches the activation point $T_a$=463 K, the gas fraction increases due to a chemical reaction

inside the gas. From this point onward, gas is generated with a reaction rate $R_p$. The formation of gas bubbles is described by solving the following equation for variable $c$ $[mol/m^3]$, which represents the amount of gas formed at any instant:

$$\frac{dc}{dt} = \nabla \cdot (Di \nabla c) + R_p(T), \tag{6.19}$$

where $Di$ $[m^2/s]$ denotes the diffusion coefficient, $c$ is gas concentration $[mol/m^3]$, $R_p(T)$ is the gas production rate, which depends on temperature.

The gas production rate $R_p$ is described as:

$$R_p = \left(\frac{c_{max} - c}{c_{max} - c_0}\right)^2 \left(\frac{G_n}{G_f}\right)^{2/3} R_c \left(\frac{T - T_a}{T_a}\right)^{r_e}, \tag{6.20}$$

where $c$ is actual gas concentration $c_{max}$ is the maximum gas concentration. The latter is introduced as a limit factor: the reaction cannot be continued as there is no glue left to produce a new portion of gas. The part of equation: $(c_{max} - c)/(c_{max} - c_0)$ describes a slowing production rate. $R_c$ is a general coefficient to get the term in the right range:

$$R_c = r_c \, T_a^{r_e} \tag{6.21}$$

where $r_c$ is proportional reaction coefficient. Gas fraction $G_n$ is the new gas volume $V_g$ divided by the total volume, which is the sum of gas and liquid volume:

$$G_n = \frac{V_g}{(V_g + V_l)}, \tag{6.22}$$

At the beginning, the volumes are equal to $V_g = G_f$ and $V_l = (1 - G_f)$. The liquid volume remains constant, since the production of gas does not imply much mass, but the gas volume increases significantly, and we assume that the gas volume is proportional to the amount of gas in mol so

$$V_g = G_f \frac{c}{c_0}. \tag{6.23}$$

Now, substituting this in equation ( 6.22) we get the expression for gas fraction, which is increasing with increasing gas concentration:

$$G_n = \frac{c}{c + c_0 \cdot \frac{1 - G_f}{G_f}}. \tag{6.24}$$

Gas production is proportional to the gas bubble surface, when considering that the gas formation takes place at the gas/glue interface of the bubble. When the bubble starts growing, its surface area increases, which, in turn, increases the gas produced per unit time. The term $(G_n/G_f)^{2/3}$ in equation (6.20) represents the increase of the surface area in comparison to the initial area.

An uncertainty of the gas formation in the glue layer, is introduced by the last part of equation (6.20) with two coefficients: the exponential reaction coefficient $r_e$ and the proportional reaction coefficient $r_c$. These coefficients were varied in order to find the best correlation with experimental results.

Hence, from the production rate we can calculate the gas concentration $c$ using equation (6.19). At this point the gas quantity $n_{gas}$ can be determined from:

$$n_{gas} = \int_0^{l_{glue}} c \; dydzdx, \tag{6.25}$$

where $dydz$ is a small piece of the die area [m] and $l_{glue}$ is glue thickness [m]. Using the ideal gas law, the pressure is determined by:

$$p = \frac{nR_uT}{V_{gas}}, \tag{6.26}$$

where $n$ is the number of moles, $R_u$ is the universal gas constant.

$$p = \frac{nR_uT}{V_{gas}} = \frac{R_u}{V_{gas}} \int_0^{l_{glue}} cTdydzdx \tag{6.27}$$

The gas volume is increasing according to:

$$V_{gas} = dydzx(y); \tag{6.28}$$

The pressure rise can be calculated from:

$$p(y) = \frac{R_u}{V_0 + \triangle V} \int_0^{l_{glue}} cT \; dydzdx \tag{6.29}$$

where $V_0$ is the initial volume of the gas bubbles in the tape, and $\triangle V$ is the volume expansion of gas. The initial gas volume is $dydzx_0$ with $x_0 = G_f \cdot l_{glue}$. The volume expansion is equal to $\triangle V = dydzx(y)$, with $x(y)$ the displacement of the die interface from its initial position,

$$p(y) = \frac{R_u}{(G_f \cdot l_{glue} + x(y))} \int_0^{l_{glue}} cT \; dx. \tag{6.30}$$

The initial gas concentration $c_0$ $[mol/m^3]$ at atmospheric pressure $p_0$ [Pa], initial temperature $T_0$ [K] and gas fraction $G_f$=0.16 are calculated from:

$$c_0 = \frac{p_0 G_f}{R_u T_0}. \tag{6.31}$$

## 6.4 Release dynamics

The general configuration of the tape, glue and die is illustrated schematically in Figure 6.2.

The die speed can be calculated using Newton's relation:

$$\ddot{x_c} = \frac{F}{m}, \tag{6.32}$$

where $x$, $[m]$ is the die location, $m$ is the die mass $[kg]$ and $F$ $[N]$ is the force applied to the die.

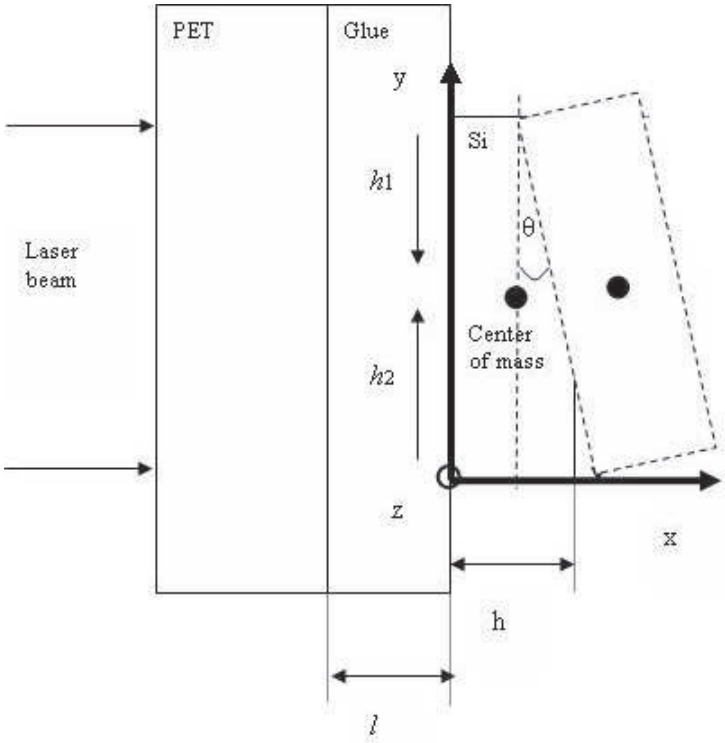


Figure 6.2: Schematic view of the three-layer configuration coordinate system.

This force is determined by the pressure generated by the gas bubbles, multiplied by surface area $A$. As we consider a two dimensional model, the force $F$ can be obtained from

$$F = \int_A ((p(y) - p_0)dA = d_z \int_0^d (p(y) - p_0)dy, \tag{6.33}$$

where $p(y)$ is an absolute pressure, and $p_0$ is atmospheric pressure [Pa]. The absolute pressure, in the case of the ablative release, is calculated according to equation (6.16) and in the case of thermal release according to equation (6.30). The forces applied to the die may not be uniform and, as a result, the die will rotate around its center of gravity. This can be described by using the angular acceleration formula:

$$\ddot{\theta} = \frac{M}{J} \tag{6.34}$$

where $\theta$ [rad] is the angle of the die rotation and the $J$ $[kgm^2]$ is the moment of inertia of the die. The latter is calculated according to the formula for a thin rectangular plate with height $d$ width $h$ and mass $m$:

$$J = \frac{1}{12} m(d^2 + h^2). \tag{6.35}$$

The angle $\theta$ represents the die rotation. It is the angle between the die surface and the tape surface, considering the die and tape surfaces that were previously connected. From this angle and the instant of detachment the flying angle is calculated. It is this flying angle that directly influences the positioning accuracy of the die on the receiving substrate. This flying angle is not explicitly calculated in the model. It is estimated under the assumption that the die first gets a rotating movement around the edge of the die (the edge which remains attached longest). This rotation is directly related to the velocity of the die center of mass, which in other words follows a circular path around the rotation center (the edge of the die). Once the edge finally detaches from the tape, the remaining movement is a straight linear movement of the center of mass with the velocity that the center of mass has, at the instant of detachment. The axial component $x_c$ of the velocity of the center of mass is given as $\ddot{x_c}$, equation (6.32) and the angle, at the moment of detachment, is given by $\theta$ at that very instant.

For a displacement and rotation the axial $x$-component of the die position is calculated from

$$x(s) = x_c + s \cdot sin(\theta), \tag{6.36}$$

where $s$ [m] is the parameter that indicates the position on the die as the distance measured from the mass center position, $x_c$ [m] is the position of the die center.

In the same way the $y$-component of the die position can be calculated

$$y(s) = y_c + s \cdot cos(\theta). \tag{6.37}$$

In the model $y_c$ is not calculated. For small $\theta$ there is an assumption that $sin(\theta)$ is equal to $\theta$ and for $cos(\theta)$ is equal to 1. Based on these, the total displacement of the die is calculated as:

$$D = x_c + \theta(y - \frac{d}{2}). \tag{6.38}$$

The moment of rotation $M_c$ about the axis passing through the center of mass and parallel to the axis $z$ follows from:

$$M_c = \int_A -(y - y_c)((p(y)) - p_0)dA = d_z \int_0^d -(p(y) - p_0)(y - \frac{d}{2})dy, \tag{6.39}$$

where $y_c$ is the die's center of gravity. The following assumption is made in the model: the break-off takes place from the sides towards the die's center.

Once the die is locally detached, that area of the die no longer contributes to the force or moment, equations (6.33) and (6.39), so

$$F = d_z \int_{h_1}^{d-h_2} (p(y) - p_0)dy, \tag{6.40}$$

$$M_c = d_z \int_{h_1}^{d-h_2} -(p(y) - p_0)(y - \frac{d}{2})dy. \tag{6.41}$$

To describe the break-off condition, the following assumption was made: as long as the gas pressure is less than threshold pressure $p_{thr}(G_n)$, the die remains attached:

$$p < p_0 - p_{thr}(G_n), \tag{6.42}$$

where $p_{thr}(G_n)$ represents the adhesive force over the die area, which is changing due to the gas bubble area, which grows due to the increase of the gas fraction $G_n$, see equation (6.24).

When this criterion is satisfied, positions on the glue-die interface, where the die begins to release from the tape, $h_1$ and $h_2$, start to grow, see Figure 6.2. The die is totally disconnected if

$$\left(\frac{h_1 + h_2}{d}\right) \geq 1. \tag{6.43}$$

When this condition is not satisfied, the die may be still be partially connected.

Coefficients, $C_1$ and $C_2$ are related to a excessive local tensile stress, which makes the die disconnect from the tape:

$$\frac{dh_1}{dt} = C_1, \tag{6.44}$$

$$\frac{dh_2}{dt} = C_2 \tag{6.45}$$

The values of $C_1$ and $C_2$ are zero as long as there is no detachment. When break off occurs, $C_1$ and/or $C_2$ increase to positive values, and according to the equations (6.44) and (6.45) the values of $h_1$ and $h_2$ grow as long as the values of $C_1$ and $C_2$ are positive.

The condition of the break-off is

$$p < -C_{break} \tag{6.46}$$

where $C_{break}$ is a break-off tensile stress level, measured experimentally. The value of $C_{break}$ is reduced, when the amount of bubbles and the temperature is increasing, see equation (6.47). This means that the remaining glue force is reducing and break off occurs more easily. Summarizing:

$$C_1 = \int_0^d \left(\frac{c \cdot T \cdot C_{break}}{p} - p + p_0 - C_{break}\right) \delta(y - h_1) dy, \tag{6.47}$$

$$C_2 = \int_0^d \left(\frac{c \cdot T \cdot C_{break}}{p} - p + p_0 - C_{break}\right) \delta(y - d + h_2) dy, \tag{6.48}$$

where $\delta$ is a Dirac delta function.

Once the die is totally disconnected, a free flight is assumed, moving steadily with a constant speed that it has at the moment of detachment.

The release mechanism as described here in equations (6.40) and further, are only applied to the thermal release models. In case of ablative release, it is assumed that the whole die surface reaches the evaporation temperature and, as a consequence, the die is completely detached at that time. The force and moment which accelerates the die are applied when the die already released. So for the ablative model only equations (6.32) to (6.39) are used.

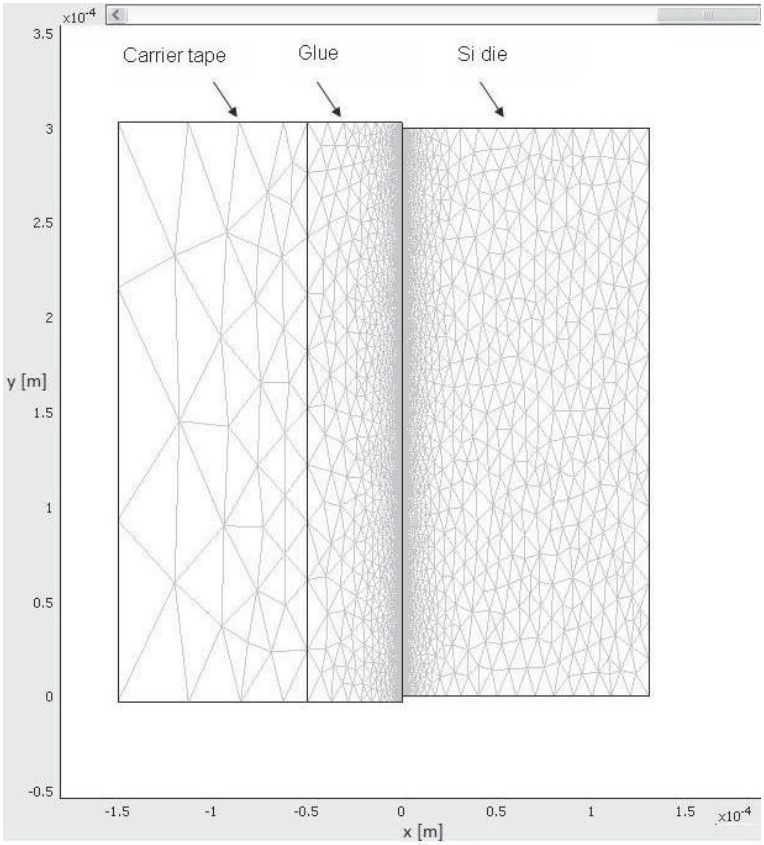


Figure 6.3: Mesh used for the simulations in COMSOL.

## 6.5 Model implementation

The practical implementation of the model was based on the Finite Element approach for which the Comsol Multiphysics code was used. The COMSOL Multiphysics simulation software environment facilitates all steps in the modeling process - defining geometry, meshing, specifying physics, solving, and then visualizing results.

The 2D geometry of the system was defined in three domains: tape, glue and silicon die, with appropriate sizes. The constants were described, such as laser fluence, pulse duration, reflectivity, material properties etc. Silicon absorption was defined as a function of temperature. The model set-up used predefined physics interface modes: heat transfer by conduction, diffusion and partial differential equations (PDE). Meshing was used, dividing the geometry into small elements. In the model, a non-uniform density of the triangular meshes was generated, with a finer mesh near the boundary, see Figure 6.3.

The time step was automatically chosen by Comsol based on the resulting error estimate. If the error is too large, after several iterations, it will reduce the time step and if it is small after the first iterations it will try to increase slowly the time step. The user chooses some maximum and initial time step, and from then on, Comsol

chooses to increase or decrease the value, but with a maximum time step limitation as indicated.

A series of calculations were performed to study the influence of the most important parameters involved in the die release process, which are: laser energy, pulse duration, homogeneity of the energy distribution within the beam, etc.

## 6.6 Simulation results

This section consists of three subsections: the first subsection presents results of the ablative release approach, where the die release is achieved by rapid silicon evaporation under highly intense 1064 nm laser irradiation. The second subsection shows the results of the thermal release due to growing of the gas bubbles in the glue material using low-intensity 1064 nm laser IR light. The third subsection deals with calculations for the thermal release using 532 nm radiation.

The dimensions of the focal spot of the laser beam used in the calculations had the same size as the irradiated die and assumed to cover the die homogenously. The dimensions of the silicon die were chosen to be 300 $\times$300 $\mu$m, thickness 130 $\mu$m and the tape thickness was 150 $\mu$m, of which 50 $\mu$m is a glue layer. Coordinates for the carrier tape, glue and silicon die are represented in Figure 6.3.

### 6.6.1 Simulation results with the ablative release model

The incident energy density varied between 3 J/cm$^2$ and 9 J/cm$^2$ which corresponds to conditions where the die release was observed experimentally, see section 4.4. The laser pulse duration was chosen to be 45 ns; the same as in the experiments.

Material parameters, used in the ablative release calculations are represented in Tables 6.1 and 6.2, [All95].

Table 6.1: Optical properties of silicon at high-intensity 1064 nm irradiation.

| Name | Si, 1064 nm |
|---|---|
| Reflectivity $R$ | 0.35 |
| Absorption $\alpha_L$ [cm$^{-1}$] | $10^4$ |

Table 6.2: Material properties used in calculations, high intense 1064 nm laser irradiation, release from PVC tape.

| Name | PVC | Si |
|---|---|---|
| Conductivity $k$ [W/(m K)] | 0.38 | 163 |
| Density $\rho$ [kg/m$^3$] | 2200 | 2330 |
| Specific heat $c_p$ [J/(kg K)] | 1900 | 703 |

The laser light propagates through the tape and heats the silicon surface. The temperature distribution in the silicon die, at the end of the laser pulse, is shown in

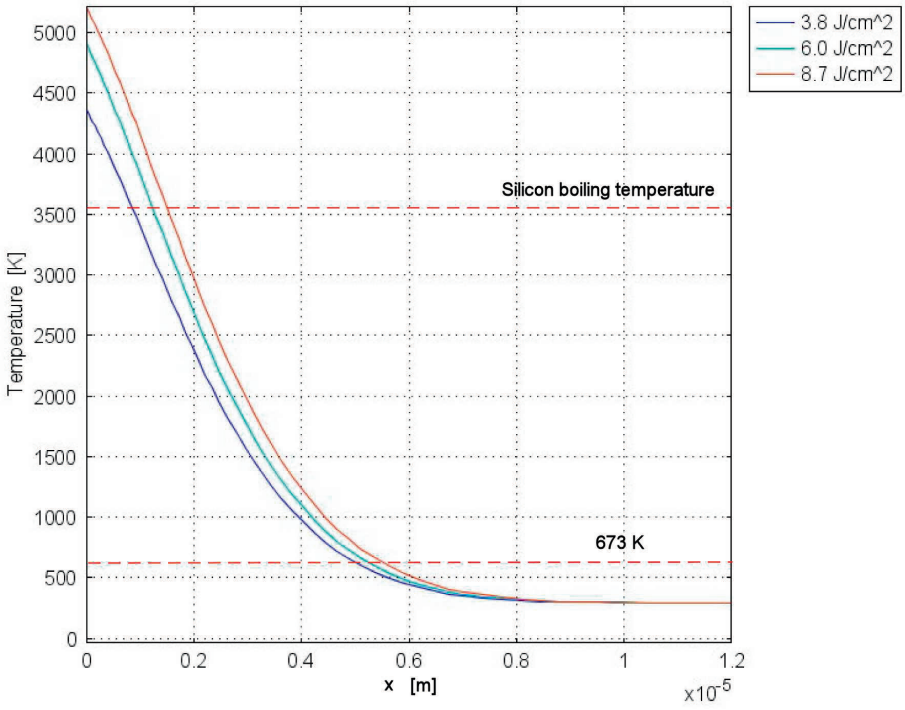


Figure 6.4: Temperature distribution within a silicon die, at the end of the 1064 nm laser pulse, for different laser fluences, $t_p$=45 ns, PVC tape.

Figure 6.4. Remember, that the dimensions and coordinates are defined according to Figure 6.3 as described in Section 6.5.

In this Figure, the temperature distribution at 3 laser fluences, release threshold fluence, 3.8 J/cm$^2$, then for 6.0 J/cm$^2$ and finally for the maximum fluence used in experiments, which was 8.7 J/cm$^2$ are shown. The silicon surface temperature in all cases is higher than the silicon boiling temperature which is 3538 K. The maximum die temperature was 5215 K at highest laser fluence, which was 8.7 J/cm$^2$. The corresponding die velocity was 14.2 m/sec.

When the system reaches the equilibrium temperature, the opposite side of the silicon die never reaches the damage point of 673 K.

Calculations of the die speed for different laser fluences are shown in Figure 6.5. From this Figure it is clear that the die acceleration took place within a laser pulse duration, and the release at different laser fluences took place in about the same time frame. When the temperature reaches a level above the evaporation level of silicon, it is assumed that the die is totally disconnected from the tape. The recoil pressure $p_r$ is directly related to the temperatures reached on the interface, if the temperature is lower, the pressure is less, and the acceleration is therefore less, resulting in a lower release speed.

The comparison of the component release velocities which were calculated using

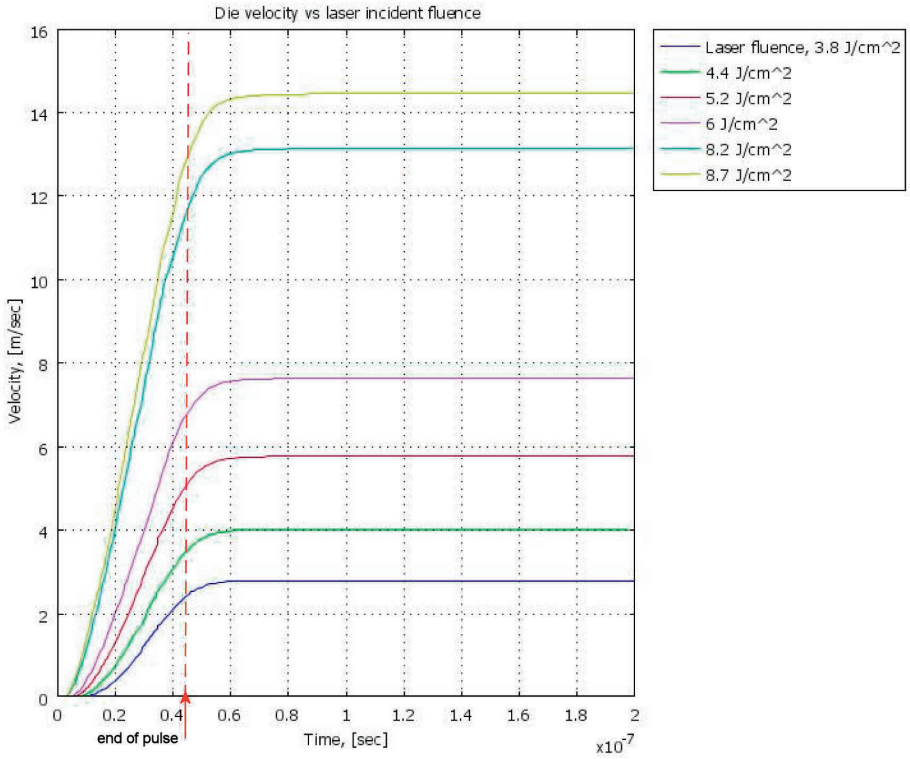


Figure 6.5: The calculated velocity of the released dies, as function of the incident 1064 nm laser fluence, $t_p$=45 ns, PVC tape.

the model and observed during experiments, is shown in Figure 6.6. The fluence release threshold was determined experimentally to be about 3.0 J/cm$^2$. The model calculations show that, for this laser fluence, the speed of the die release is 1 m/s, whereas in the experiments speed of 1.7 m/s was observed, see Figure 6.6. For lower fluences, no release occurred experimentally. The result of the calculations is in good agreement with the experiments. To simulate the rotation of the component, the extreme case was chosen, when only half of the component is irradiated. The rotation speed is found to be a factor of two higher than experimentally found; $2\times10^4$ rad/sec in calculations and $1\times10^4$ rad/sec in experiments. This is in good agreement when taking into account that in the calculation the extreme case was considered. However, even in this extreme case the angle of flight does not correspond to the real observed value: 0.006 degrees from the model versus 4 or 10 degrees in the experiment. This difference might be explained by the fact that we assumed no pressure on the die, as long as ablation is started, and the die is detached. In reality there might still be pressure causing a bigger displacement on one side, at the same time, the glue layer in the section which is not radiated will still have an effect causing a larger flight angle.

The temperature distribution within the whole geometry, at the moment of the die release, at maximum used laser fluence, is shown in Figure 6.7. This figure shows that

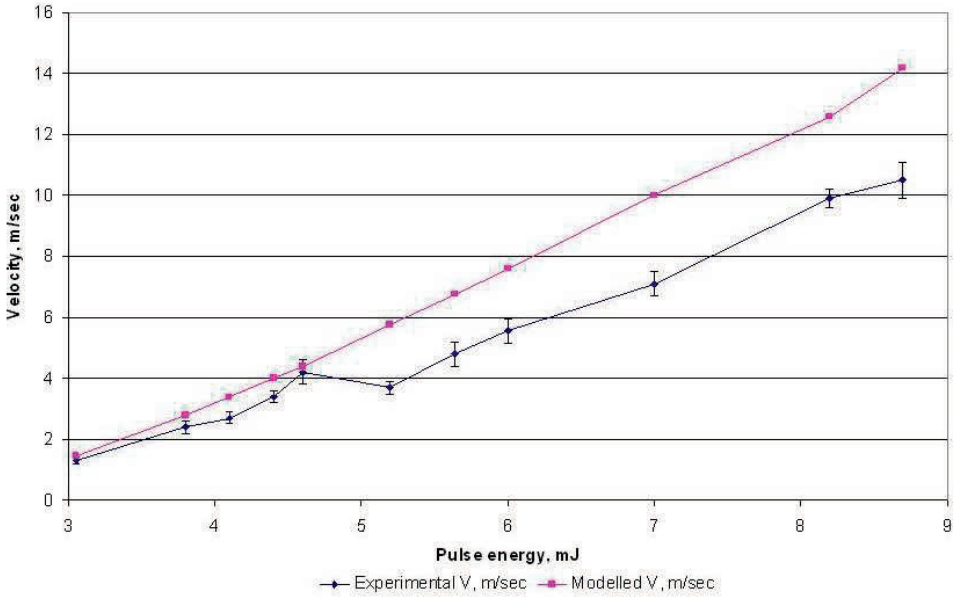


Figure 6.6: The velocity of the released dies, previously attached to PVC foil, as function of the incident 1064 nm laser energy, calculated and measured experimentally, $t_p$=45 ns, PVC tape.

almost the complete system remains at room temperature, and the heating process takes place within only 6 micrometers of the silicon surface.

In Figure 6.8 the deeper temperature penetration after 100 ms from the beginning of the laser pulse ($t_p$=45ns) is shown. The surface temperature after 100 ms is lower than after 45 ns due to cooling down. A maximum of 2700 K is reached at maximum fluence of 8.7 J/cm$^2$.

The model can predict the process behavior for different laser pulse durations. As an example, the effect of the longer pulse duration, 100 ns, is shown in Figure 6.9. The pulse energy is kept the same, the intensity is different due to a different pulse length. The penetration depth (assuming a constant $\alpha$) is roughly proportional to

$$\delta = \sqrt{\alpha t}. \tag{6.49}$$

The peak temperature obtained in case of $t_p$=45 ns was 5215 K versus 4650 K at $t_p$=100ns. Hence, with longer pulse durations, the heat propagates deeper into the bulk.

In case of longer pulse duration, the recoil pressure is much less, and therefore, acceleration is less, see Figure 6.10. On the other hand, the duration of the acceleration is longer, but the pressure is non-linear with intensity and lowers more than proportional when the temperature goes down. As a result, the velocities are much lower with longer pulses: 10.83 m/sec versus 14.2 m/sec, even though the pulse energy is the same.

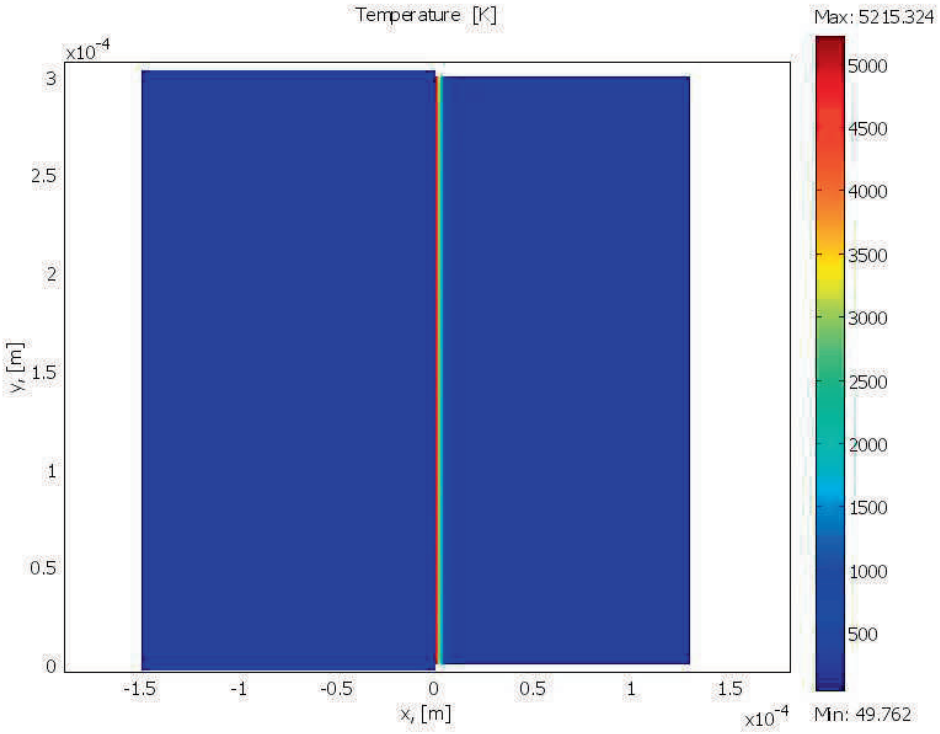


Figure 6.7: Temperature distribution within tape/die system at the end of the laser pulse, incident fluence 8.7 J/$cm^2$, $t_p$=45 ns, PVC tape.

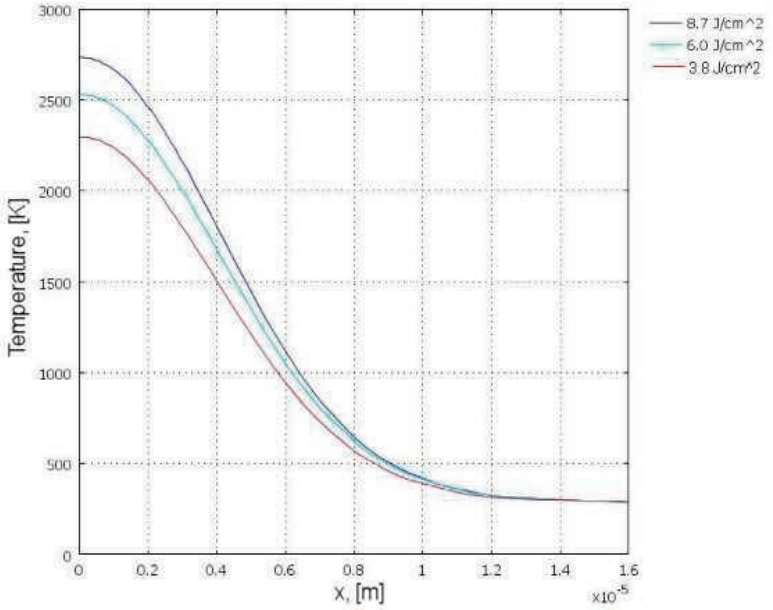


Figure 6.8: Temperature distribution within a silicon die after 100ms from the beginning of the 1064 nm laser pulse for different laser fluences, $t_p$=45 ns, PVC tape.

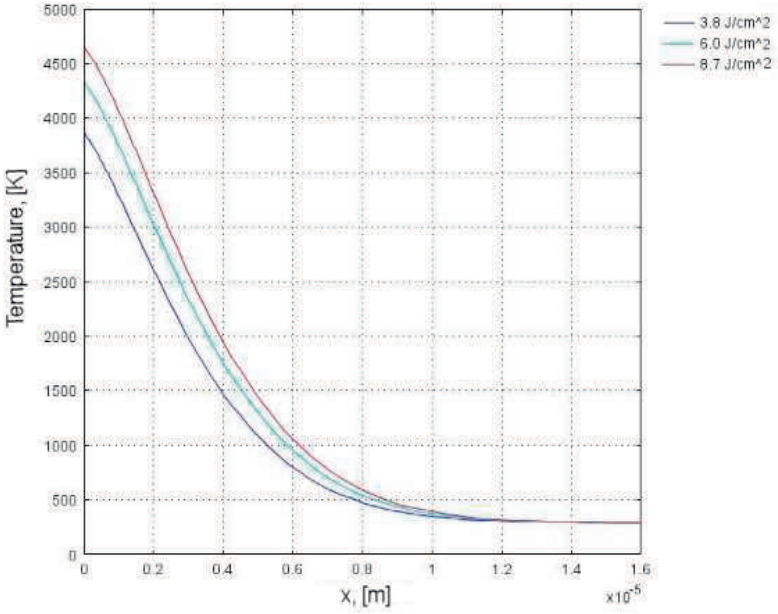


Figure 6.9: Temperature distribution within the silicon die, at the end of the 1064 nm laser pulse, for different laser fluences, $t_p$=100 ns, PVC tape.

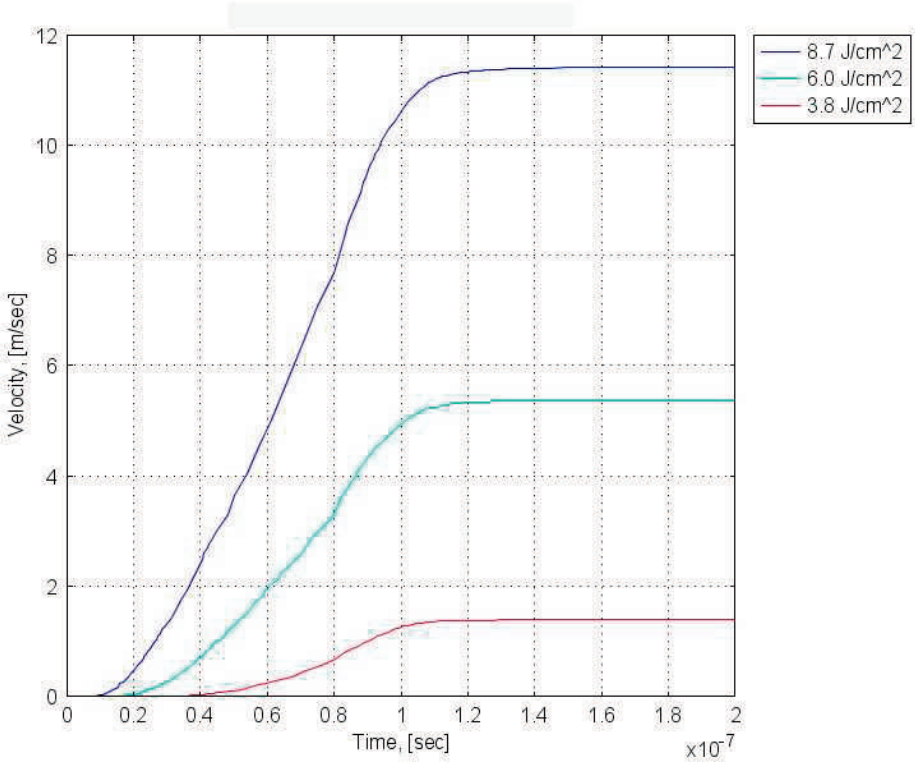


Figure 6.10: The calculated velocity of the released dies, as function of the incident laser fluence, $t_p$=100 ns, PVC tape.

### 6.6.2 Simulation results with a thermal release model

**Results of the thermal-induced release of the silicon dies from the Revalpha tape using 1064 nm laser irradiation.**

The process which is responsible for the die release, using low-intensity 1064 nm laser irradiation, is more complex than in case of the ablative release approach described in the previous section. The low intensity laser irradiation does not initiate free carrier absorption in the silicon surface and therefore the die is almost transparent for the laser irradiation. At the beginning of the pulse, the lattice absorption takes place within the bulk and therefore, the complete die heats up slowly. When using the conventional PVC tape as a carrier for the dies, it was not possible to achieve the die release with low level irradiation. Only the ablation release was possible. In the glue layer of the Revalpha tape (made of PET), using which the thermal release was possible, initially there is an amount of gas bubbles which are randomly distributed, see Chapter 5. When the temperature of the glue layer reaches the activation level, the material of the tape starts to evaporate into the existing bubbles, causes their growth and forces the die away (the number of bubbles is assumed to remain constant during the process). When the bubble growth stops, and the die velocity already reached the level when it overcomes the break-off tensile stress level, the detachment process starts. The detachment is modeled to begin from the edges and move to the center. Once a section of the die is considered to be detached, the pressure at that section is made equal to the ambient pressure, so the remaining pressure is considered to have escaped to the edges with ambient pressure - the model discards the pressure and acceleration after disconnection of the tape. The challenge of modeling this process is to find the correct parameters responsible for the gas production inside the gas bubbles.

In the model, the following coefficients were used to simulate the gas production rate, see equation (6.20): $r_e$, $r_c$ and $c_{max}$. Coefficient $r_c$ is a proportional reaction coefficient, and the coefficient $r_e$ is the exponent of the temperature dependent term. Initially $r_e$ was chosen to be equal to 2, because making it higher makes the reaction term "explosive". Another coefficients used in the model are $c_{max}$ - the maximum gas mole production, stops the reaction when reaching the maximum level because the amount of reactants is finishing, $c_{break}$ which is the break-off tensile stress level, $C_{cal}$ is coefficient which represents the amount of heat generated for the production of the one unit of gas and $r_c$ is the proportional reaction coefficient.

There is no data available to obtain or estimate the coefficients based on physical data, so the coefficients are chosen so, that the simulation results correspond as good as possible to the experimental results. To obtain the fit, three power levels were used for each of the 2 laser light sources of 1064 nm and 532 nm. At the lowest power level, no release is expected, at medium and high power levels, the experimentally obtained velocities are provided as a reference. By means of an optimization procedure, the values of the tape coefficients are adapted in such a way that the simulation velocities have optimum correspondence to the experimental reference velocities.

The optimization procedure results in the following optimized numbers for the coefficients: $r_c$=82000 $mol/(m^3\ s)$, $c_{max}$=300 $mol/m^3$, $C_{cal}$=50000 $J/mol$ and $C_{break}$=8000 $Pa$.

In Table 6.3 optical properties of silicon, used in calculations at low-intensity 1064 nm irradiation are shown [All95]. Other material properties used in this Section are

shown in Table 6.4.

Table 6.3: Optical properties of silicon at low-intensity 1064 nm laser irradiation.

| Values at $T(K)$ | 300 | 500 | 700 | 900 | 1100 |
|---|---|---|---|---|---|
| Absorption $\alpha_L$ [cm$^{-1}$] | 12 | 105 | 470 | 1200 | 2700 |
| Reflectivity $R$ | 0.35 | 0.35 | 0.35 | 0.35 | 0.35 |

Table 6.4: Materials properties used in calculations, low-intensity 1064 nm irradiation, release from Revalpha tape

| Name | PET | Glue (PMMA) | Si |
|---|---|---|---|
| Conductivity $k$ [W/(m K)] | 0.38 | 1.9 | 163 |
| Density $\rho$ [kg/m$^3$] | 2200 | 1190 | 2330 |
| Specific heat $c_p$ [J/(kg K)] | 1900 | 1420 | 703 |
| Tensile stress $C_{break}$ [Pa] | - | 8000 | - |

Figure 6.11 shows the calculated die release speed for different levels of applied laser energies.

In Figure 6.11 it is shown that, for low energy density, 19.98 mJ, the die starts to accelerate at 0.26 ms after the beginning of the laser pulse. This acceleration starts because the gas bubbles expand by gas formation and heating. It takes 0.04 ms. Detachment occurs when the die starts to slow down, because the bubble expansion stops and starts to slow down the die, but the die breaks away and detaches. The force that decelerates the die is the remaining glue strength. For the higher power levels it can be seen that there is less deceleration, because more gas formed and the remaining glue strength is less, so there is less deceleration.

For the highest applied laser energy level, which is equal to 74.34 mJ, the die release takes place after 0.1 ms from the beginning of the laser pulse. Then the die is released with the speed of 0.85 m/sec. The delay in acceleration is observed for different laser fluences. This delay is important for synchronization between the acceleration of the die's sides. If one side of the die has different temperature, due to local overheating, this side of the die will start to accelerate much earlier. It implies a large rotational speed.

Calculated and experimentally measured die release velocities which were achieved using 1064 nm laser irradiation are shown in Figure 6.12. In the experiments it is shown that there is a clear threshold energy level below which there is no release. Above this threshold, immediately velocities of a certain level are observed, so there is a discontinuity in the velocity graph. The calculated velocity results are within the confidence interval of the experiments. For the lowest and the highest incident laser energy levels the calculated velocities are a bit out of the observed range. As it was described in Chapter 5, experimentally observed release speeds are not reproducible. For example, at the same laser energy level of 19.98 mJ, the observed release speed varies from 0.26 to 0.54 m/sec with the average velocity of 0.4 m/sec. There was no clear velocity dependency on incident laser energy; small deviation in the energy

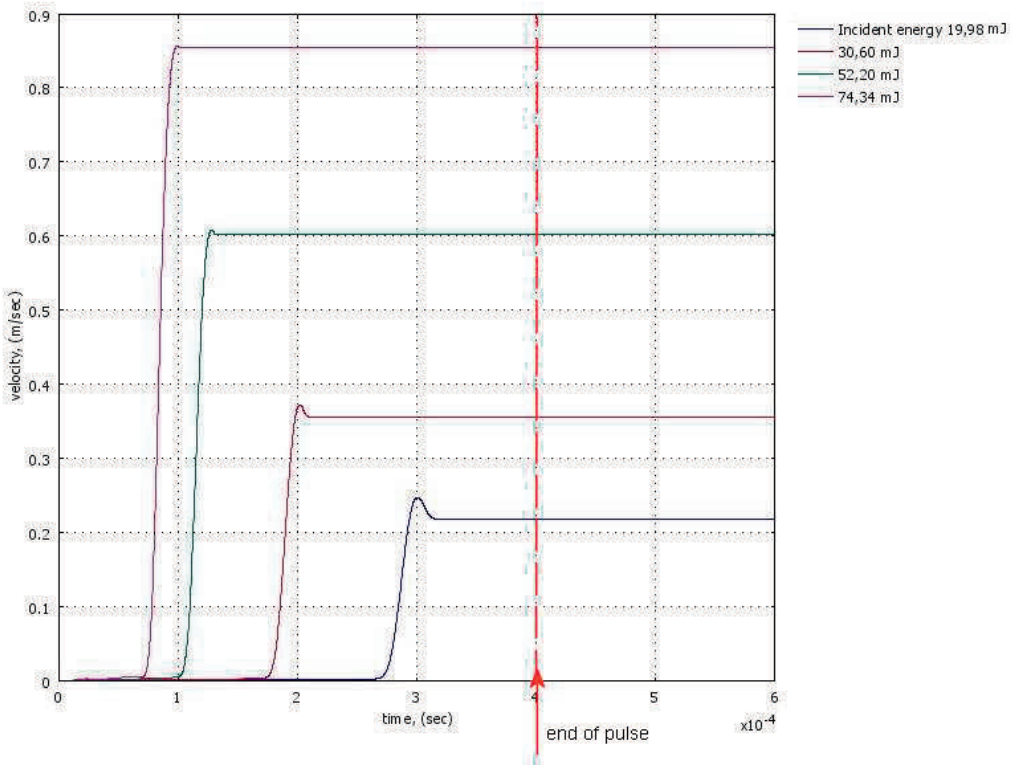


Figure 6.11: The velocity of the released silicon dies, attached previously to Revalpha foil, depending on the incident energy density, 1064 nm laser irradiation, pulse duration is 0.4 ms.

distribution within the laser beam, within the die due to impurities or pollution of the silicon surface can affect the velocity. Another reason, which is considered to be less important, is the model implementation of the break-off force $c_{break}$. It is a constant value, but also takes into account the amount of bubbles: when there are bubbles, the assumption in the model is that the force is less. However, at high laser energy there are so many bubbles that the break-off force is almost negligible, see Figure 6.11. Hence, the calculated speed is higher than experimentally observed. In case of the lower energy for the same reason, the speed is lower than experimentally observed.

Figure 6.13 shows calculated temperatures within the die for 19.98 mJ laser incident energy, which is the threshold energy for the die thermal release at 1064 nm irradiation. It can be clearly seen that the die is heated up within the bulk. Die is released on 0.295 ms from the beginning of the laser pulse. Three graphs which represent temperature calculations at the time instance 0.30, 0.31 and 0.315 ms shows effect of "isolation layer". This happened because to model the release of the die parameter "switch" was used. The parameter switch is a switching function (Heaviside

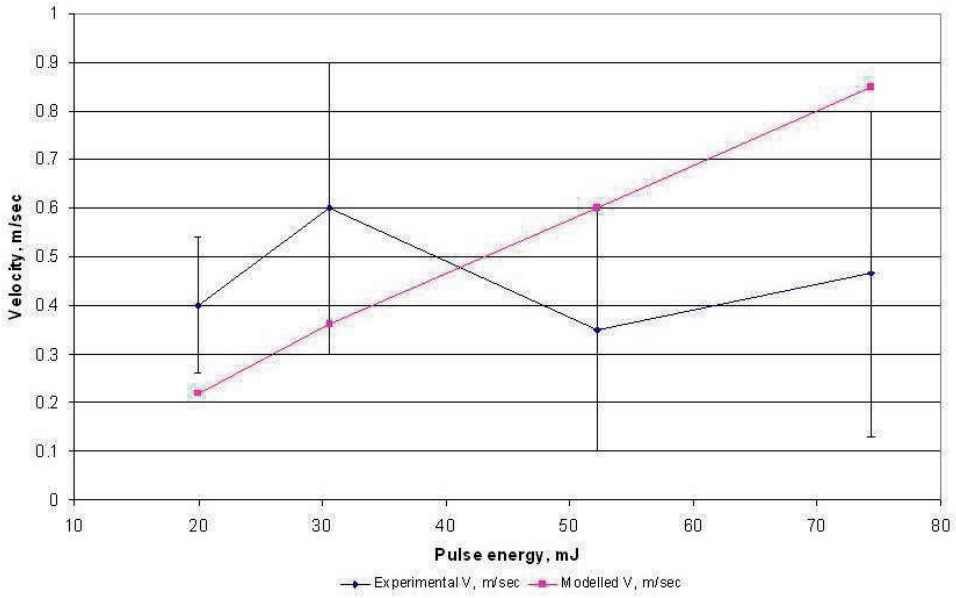


Figure 6.12: The velocity of the released dies, as function of the incident 1064 nm laser energy, measured experimentally and calculated.

step function) which is used to switch of the heat conductivity coefficient (making it very small)once the die is released. In the moment that the die releases, it is supposed that the connection between the die and the glue layer does not exist anymore. In model the die elements remains in contact with the glue elements, so the glue layer will keep absorbing heat from the die. In order to avoid that the heat flux to the glue layer keeps existing, the switch is used to make the conductivity in a thin die layer equal to a negligible small value in order to prevent heat the conductive heat flux in that layer, and form an artificial isolating layer. In order to avoid that the temperature in the die layer increases unbounded by a continued deposition of energy in the isolation silicon layer, the heat source in that layer is also turned off, and that is why the temperature remains constant in the isolation layer, once the section of the die is detached from the tape. Even if the isolation layer is created, the rest of the die can be used for an estimation of the temperature that is reached in the die: after 0.315 ms from the beginning of the laser pulse, the maximum temperature of the silicon die is 392.9 K.

In Figure 6.14 the silicon temperature is shown at the maximum incident laser energy, 74.34 mJ at different time steps, pulse length $t_p$=0.4 ms. At first, there is low absorption in the die, and heating is taking place all over the die. When it gets more heated up with time, the heat starts to concentrate closer to the boundary zone ($x$=0.2x10$^{-4}$ m) which, in turn, speeds up the heating. This effect is the main reason why the release under these conditions is unsteady. In the die release it is possible to recognize this effect by the fact that the die release for low power is much later in time, see Figure 6.11 in comparison with the instant die release or starting point of

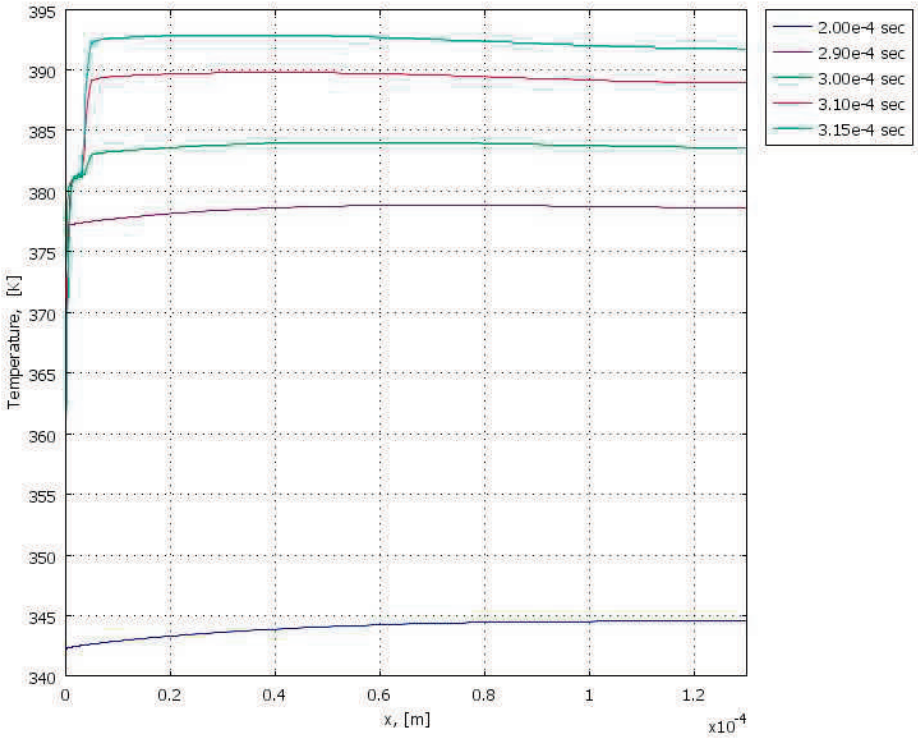


Figure 6.13: Temperature distribution within a silicon die at different time steps from the beginning of the 1064 nm laser pulse, incident energy 19.98 mJ, Revalpha tape.

acceleration for the high power release, see Figure 6.5 in Section 6.6.1.

From these results the conclusion can be drawn that, the silicon die does not reach the damage temperature of 673 K. Another interesting effect, which can be observed from these pictures is the "edge" effect: the heat from the edges of the die heats up the glue layer in the small section (at $y < 0$ and $y > 300$ micrometer) where they are not in contact with the die. It is a local effect and it is causes a slightly cooler edge of the die, because it loses more energy due to the heat sink into the unheated area.

The temperature in the glue layer reaches its maximum level of 354.5 K at 0.30 ms from the beginning of the laser pulse, see Figure 6.15. The maximum temperature when the die is already released from the tape (0.316 ms from the beginning of the laser pulse) is lower, 348.5 K which confirms that the die is not anymore in contact with the tape.

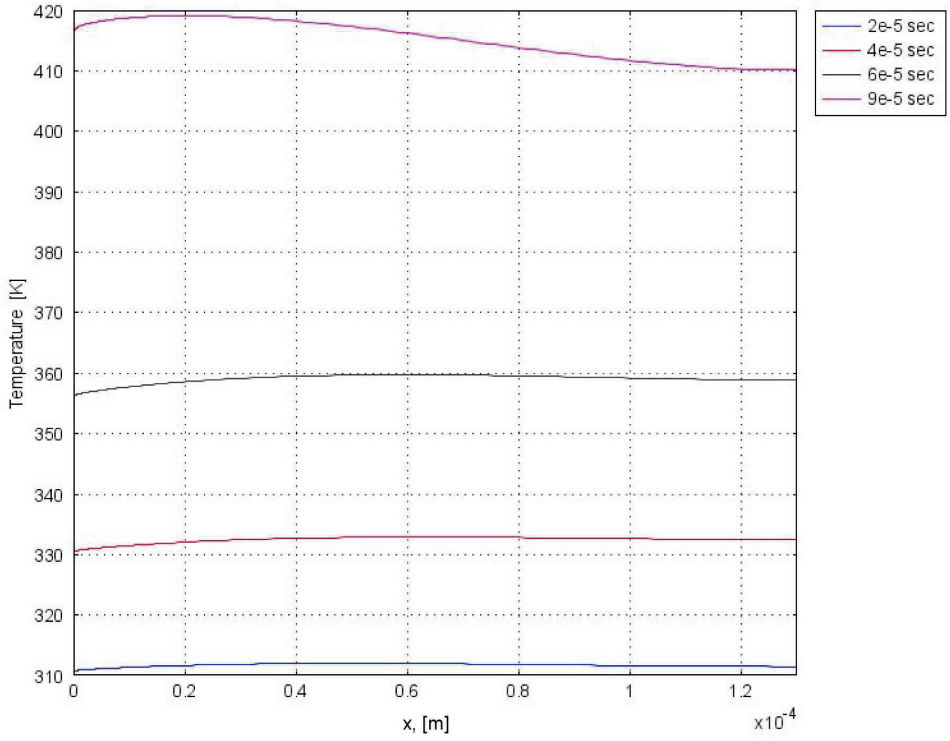


Figure 6.14: Temperature distribution within a silicon die at different time steps from beginning of the 1064 nm laser pulse, incident energy 74.34 mJ, Revalpha tape.

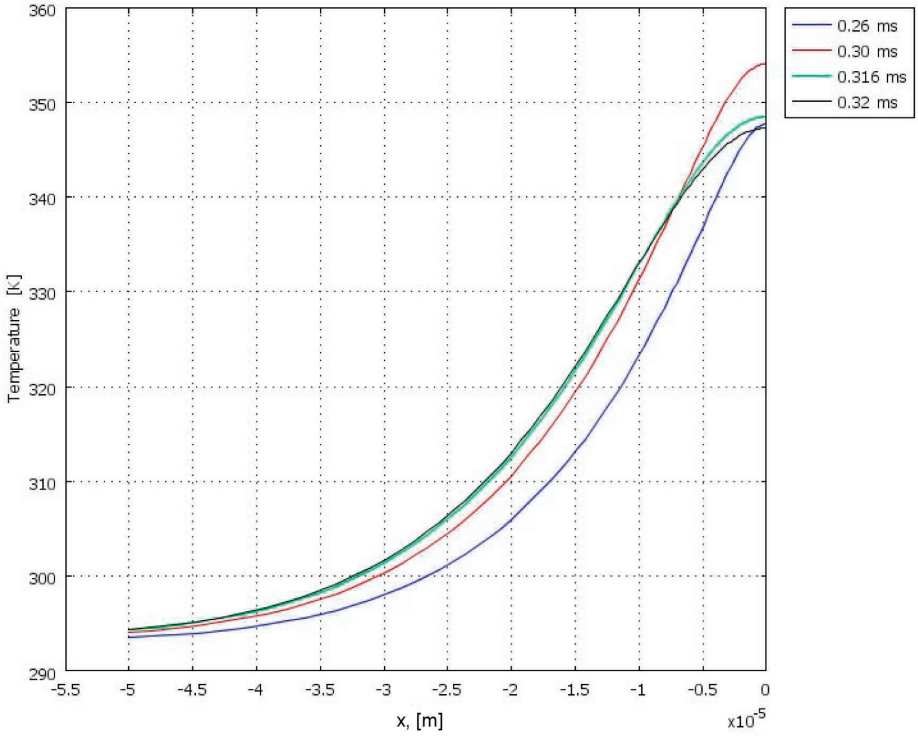


Figure 6.15: Temperature distribution within the glue layer at different time instances from the beginning of the 1064 nm laser pulse, incident laser energy 19.98 mJ on Revalpha tape.

The maximum temperature calculated for the glue layer is 350 K at 0.09 ms from the beginning of the laser pulse. Release takes place at 0.1 ms from the beginning of the laser pulse. The temperature distribution within the glue layer at different moments in time for 19.98 mJ is shown in Figure 6.16.

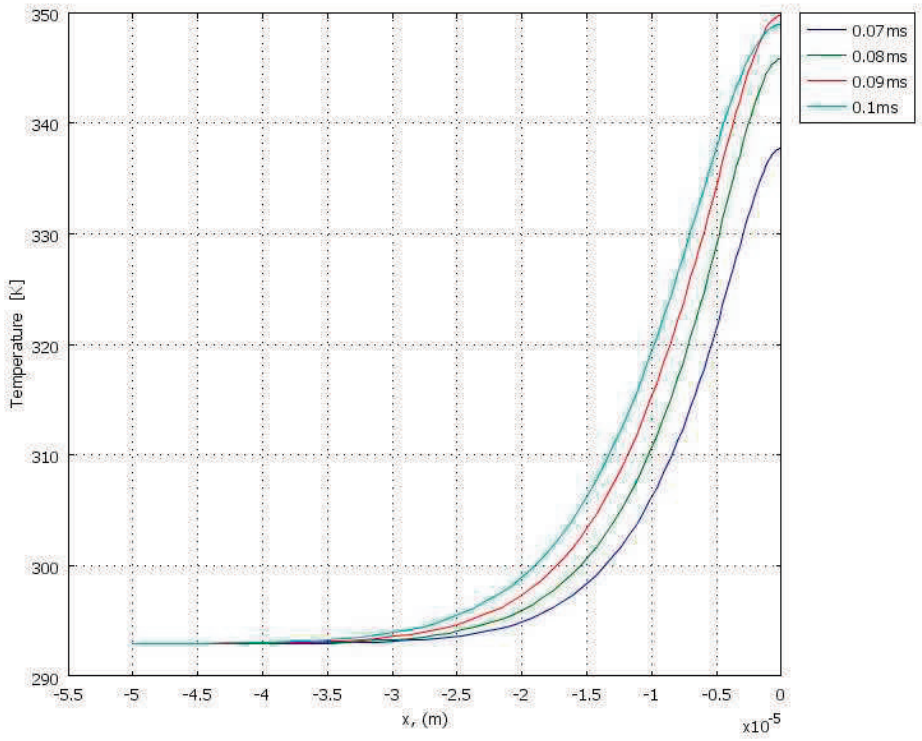


Figure 6.16: Temperature distribution within the glue layer at different time instances from the beginning of the 1064 nm laser pulse, incident laser energy 74.34 mJ on Revalpha tape.

From the temperature distribution in the glue layer at the lowest incident laser energy level, 19.98 mJ, shown in Figure 6.15, one can conclude that the maximum temperature of the glue layer was achieved at the lowest energy level. This can be explained with the fact that the tape remains in contact with the die during only 0.1 ms at highest energy level and and 0.295 ms at lowest energy level. From calculations of the temperature within the glue layer, it is concluded that the condition, needed to achieve the release of the die from the tape, is to heat up 5 micrometers of the glue layer to the temperature of 340 K. The temperature distribution in the glue layer at 30.6 mJ confirms this, see Figure 6.17. That is, the release takes place after 0.20 ms from the beginning of the laser pulse and the glue layer of 5 micrometers is heated up to 340 K.

Calculation of the force applied at the center of the die versus time from the beginning of the laser pulse is shown in Figure 6.18 for 19.98 mJ incident laser energy.

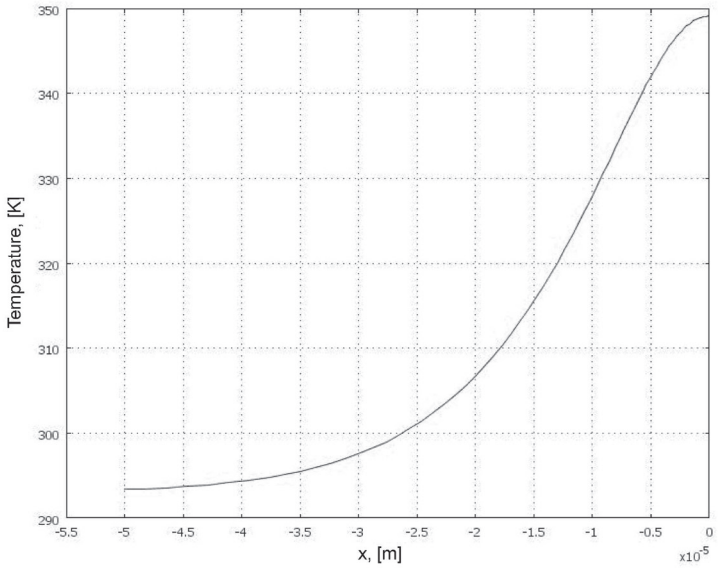


Figure 6.17: Temperature distribution in the glue layer at 0.20 ms from the beginning of the 1064 nm laser pulse, incident laser energy 30.6 mJ on Revalpha tape.

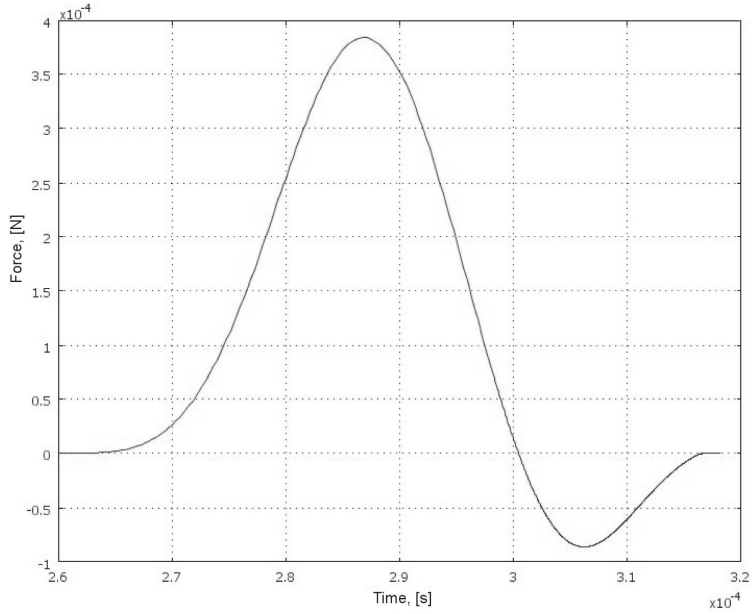


Figure 6.18: External force applied to the center of the die versus time, incident 1064 nm laser energy is 19.98 mJ.

When the gas production reaction is finished, at 0.28 ms from the beginning of the laser pulse, the pressure is at its peak value; when the pressure is high, it pushes the die and it accelerates. That will continue until the pressure reduces to zero (relative pressure) at 0.30 ms from the beginning of the laser pulse. When the force is zero, the pressure in the glue layer is equal to the pressure in the atmosphere. Then the glue layer expands less than the speed of the die and that means that the die is pulling the glue until it breaks off, when the tensional pressure (negative relative pressure) is larger than the break-off level. This effect takes 0.016 ms and after that, at about 0.295 ms from the beginning of the laser pulse, the die is disconnected and released from the tape with the constant velocity of 0.22 m/sec.

At the higher laser energy level of 30.6 mJ, the tape sticky effect is still observed but its duration is much shorter, -0.007 ms, and at the highest energy level which is 74.34 mJ, the effect is negligible, see Figure 6.20.

The maximum force values at the incident laser energies 19.98, 30.6 and 74.34 mJ are: $3.8\text{x}10^{-4}$ N, $6.7\text{x}10^{-4}$ N and $1.68\text{x}10^{-3}$ N respectively.

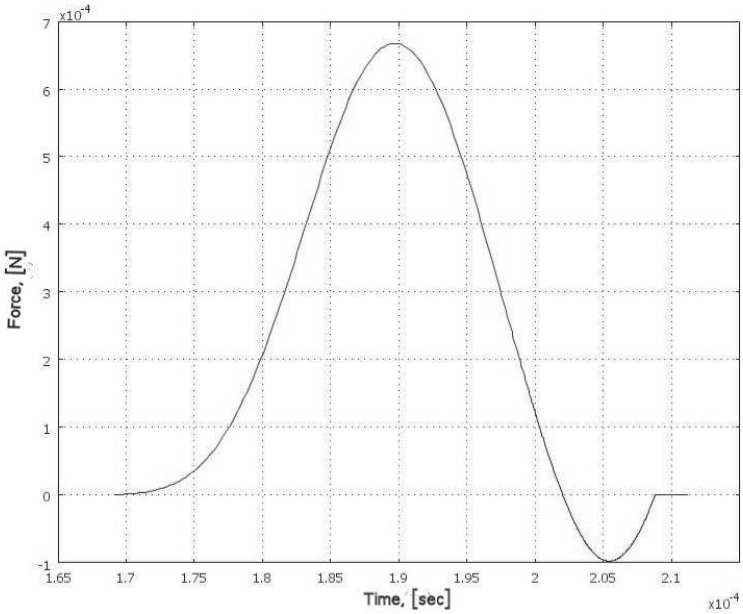


Figure 6.19: External force applied to the center of the die versus time, incident 1064 nm laser energy is 30.6 mJ.

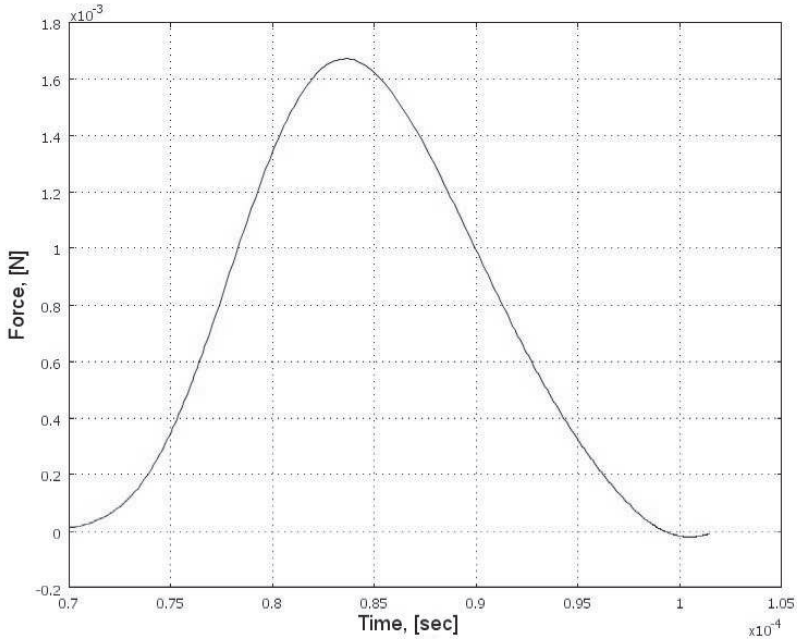


Figure 6.20: External force applied to the center of the die versus time, incident 1064 nm laser energy is 74.34 mJ.

An indication of how sensitive the non-uniformity of the intensity of the die is for the the rotation speed of the released die, is shown in Figure 6.21. The laser intensity is described so, that the value of $Z$ is the relative difference in intensity between the two sides of the die.If the value of $Z$ is equal to 0.10 the intensity is 95% on one side and 105% on the other side.

$$I = I_0(1 + Z(y/d - 0.5)) \tag{6.50}$$

Calculations were carried out for the highest energy of 74.34 mJ. The angle $\theta$ for different values of the coefficient Z (0.1, 0.05 and 0.012) is shown in Figure 6.21 for incident laser energy 74.34 mJ. The die is released in 0.1 ms from the beginning of the laser pulse. The angle $\theta$ reaches the value of 0.208 rad in 0.6 ms from the beginning of the laser pulse. That means, the die makes one revolution in about 18 ms. In that time the die flies about 15 mm. In the experiments with 1064 nm irradiation the observed tumbling was unpredictable and different even for the same level of the applied laser energy. The distribution of the energy within the beam was also not stable, with some peaks. It is difficult to compare the calculated results with the experimental ones in this case.

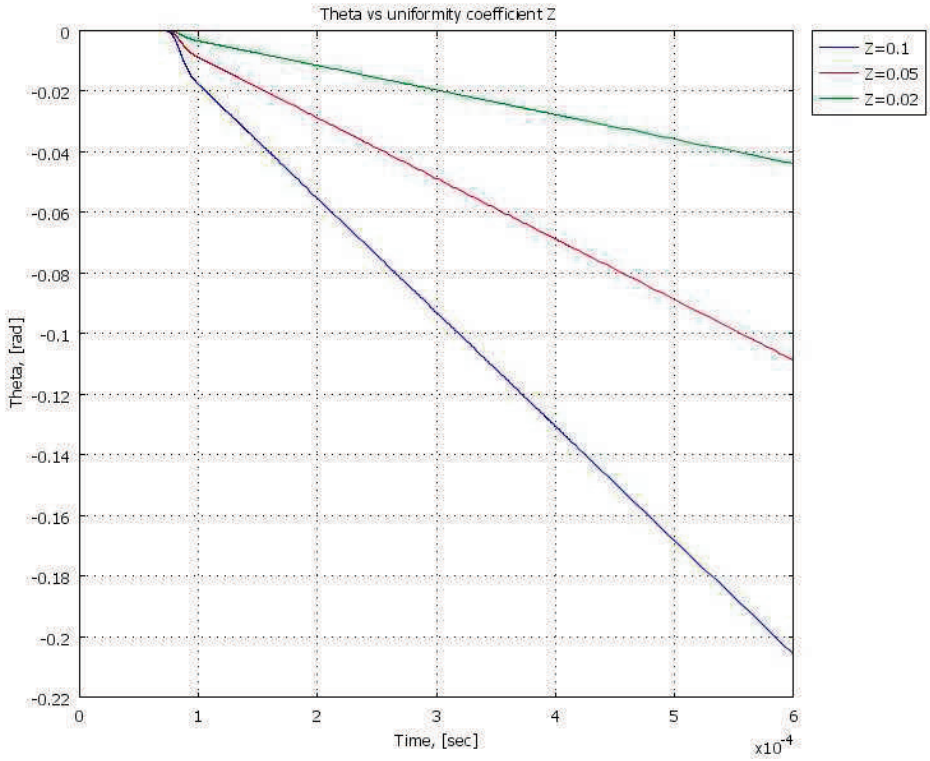


Figure 6.21: The angle $\theta$ of the die release at different coefficients $Z$, 1064 nm laser energy 74.34 mJ.

### Conclusion

The velocities predicted by the model and the experimentally measured velocities are in good agreement which confirms that the model calculations are correct. Temperature calculations show that the die remains within the safe temperature range and there will be no thermal damage of the die. The model explains the observed process well. The model shows that the process is very sensitive to a small variation of the intensity distribution.

**Results of the thermal-induced release of the silicon dies from the Revalpha tape using 532 nm laser irradiation.**

The thermal release of the silicon dies using the 532 nm laser wavelength was achieved at low laser incident energy in the range from 5.94 to 13.32 mJ with 0.2 ms laser pulse duration, see Chapter 5. The difference in the die release process using 1064 nm laser and 532 nm wavelength is in the absorption mechanism of silicon for these wavelengths. In case of infrared laser irradiation the die is almost transparent and it heated up slowly within the bulk. At 532 nm, the surface absorption dominates due to the highly temperature-dependent absorption mechanism.

The thermal and mechanical material parameters used in the model are the same as used in the previous section, see Table 6.4. Only optical parameters of silicon are different, in this case see Table 6.5, [All95].

Table 6.5: Optical properties of silicon at low-intensity 532 nm laser irradiation.

| Name | SI, 1064 nm |
|---|---|
| Reflectivity $R$ | 0.37 |
| Absorption $\alpha_L$ [cm$^{-1}$] | $93880e^{(T/700)}$ |

Calculated die velocities for the laser wavelength of 532 nm are shown in Figure 6.22. There is not so much time acceleration delay difference between the energy levels observed as in case of 1064 nm thermal release, see Figure 6.11, because the heating process is smooth and stable.

For the lowest laser incident energy, at which the release was observed in 0.073 ms from the beginning of the laser pulse, the temperature distribution is shown in Figure 6.24. This graph shows that the die is heated up to 380 K mainly within 25 micrometers. The rest of the die thickness is cooler - about 340K. At the beginning of the laser pulse the temperature is distributed more homogenously.

The forces applied to the center of the die in case the laser incident energy is 5.94 mJ are represented in Figure 6.25. The effect of the tape adhesive force is observed in around 0.068 ms from the beginning of the laser pulse.

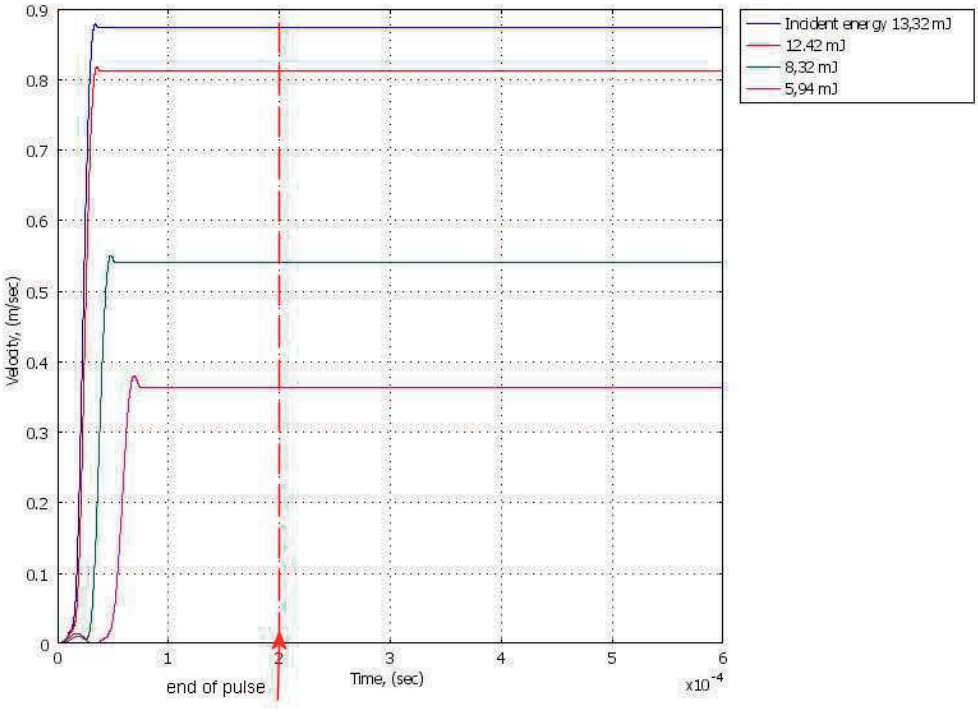


Figure 6.22: The velocity of the released dies, attached previously to Revalpha foil depending on the incident energy density, 532 nm laser irradiation, pulse duration 0.2 ms.

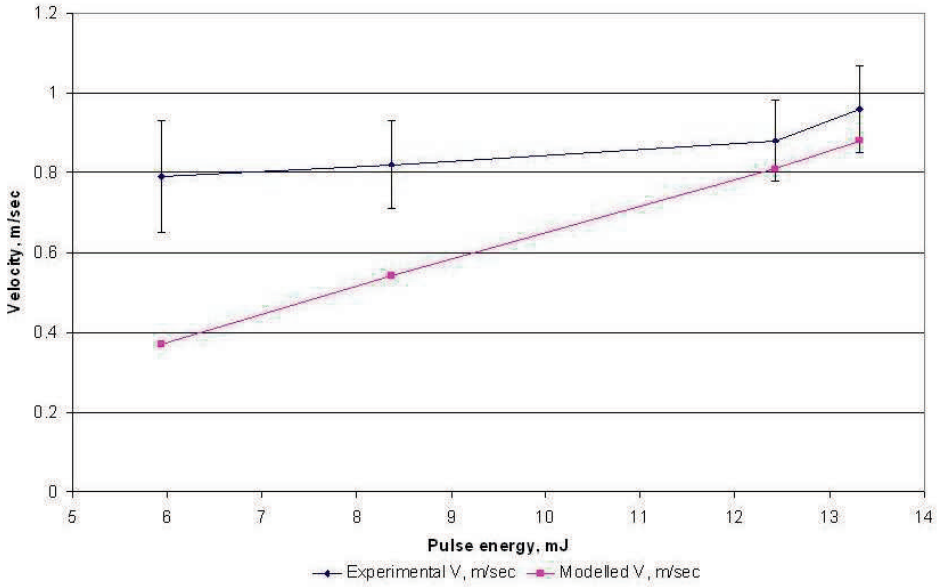


Figure 6.23: The average velocity of the released dies as function of the incident 532 nm laser energy, measured experimentally and compared with calculated velocity, Revalpha tape.

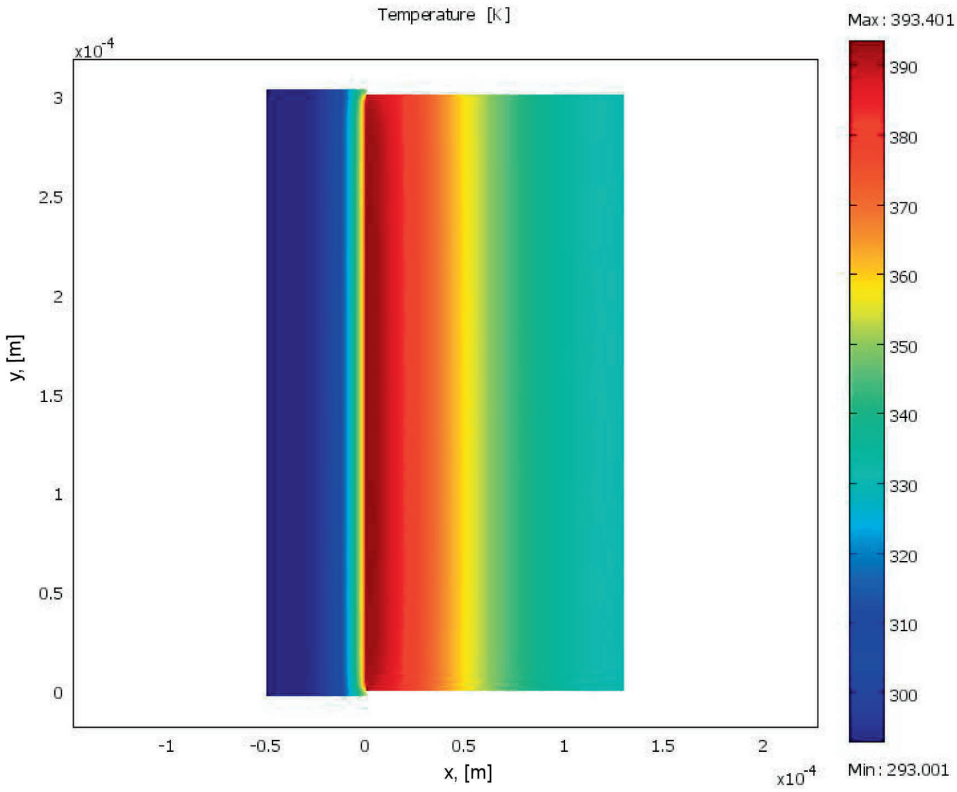


Figure 6.24: Temperature distribution at the moment of the die release in 0.073 ms from the beginning of the 532 nm laser pulse, applied laser energy is 5.94 mJ, Revalpha tape.

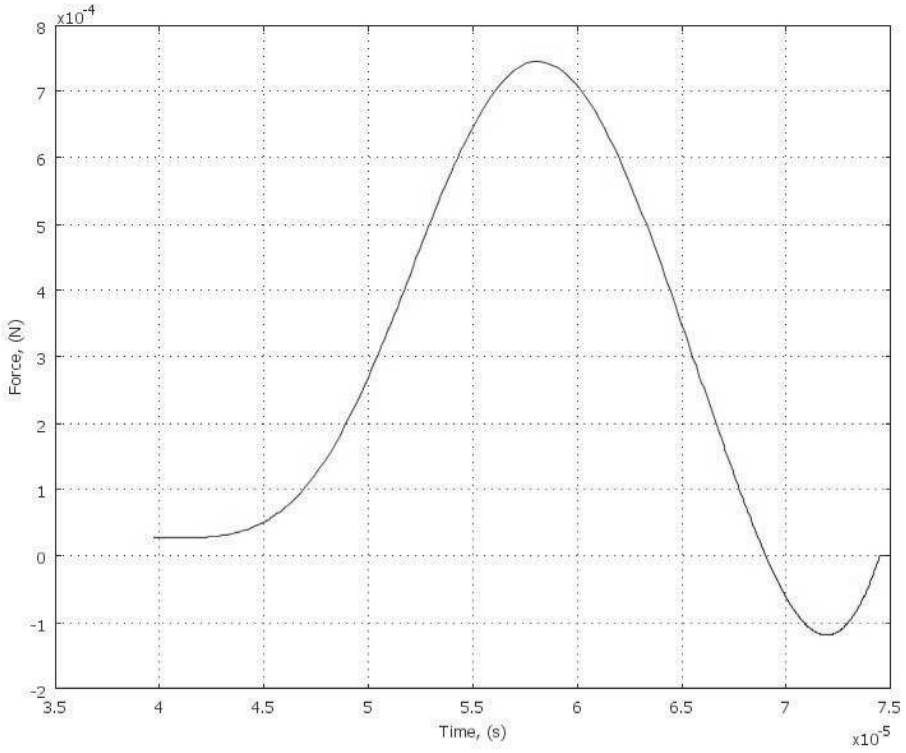


Figure 6.25: External force applied at the center of the die versus time, laser incident energy 5.94 mJ.

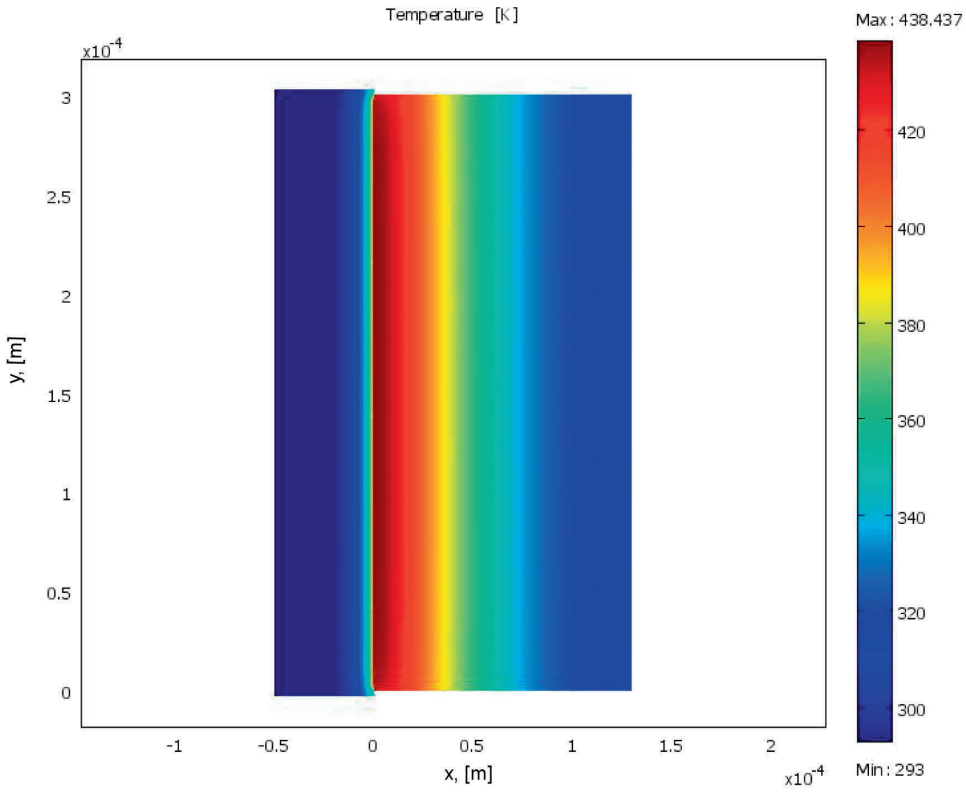


Figure 6.26: Temperature distribution at the moment of the die release in 0.036 ms from the beginning of the 532 nm laser pulse, applied laser energy is 13.32 mJ, Revalpha tape.

The temperature distribution in the glue layer and the silicon die at the highest energy level used in experiments, 13.32 mJ, is shown in Figure 6.26. It is clear that the heating of the die became even more local at the higher energy, as the absorption coefficient is highly temperature-dependent, and with higher temperature the absorption takes place at the surface of the silicon die. The opposite side of the die ($x = h$) is not heated at all.

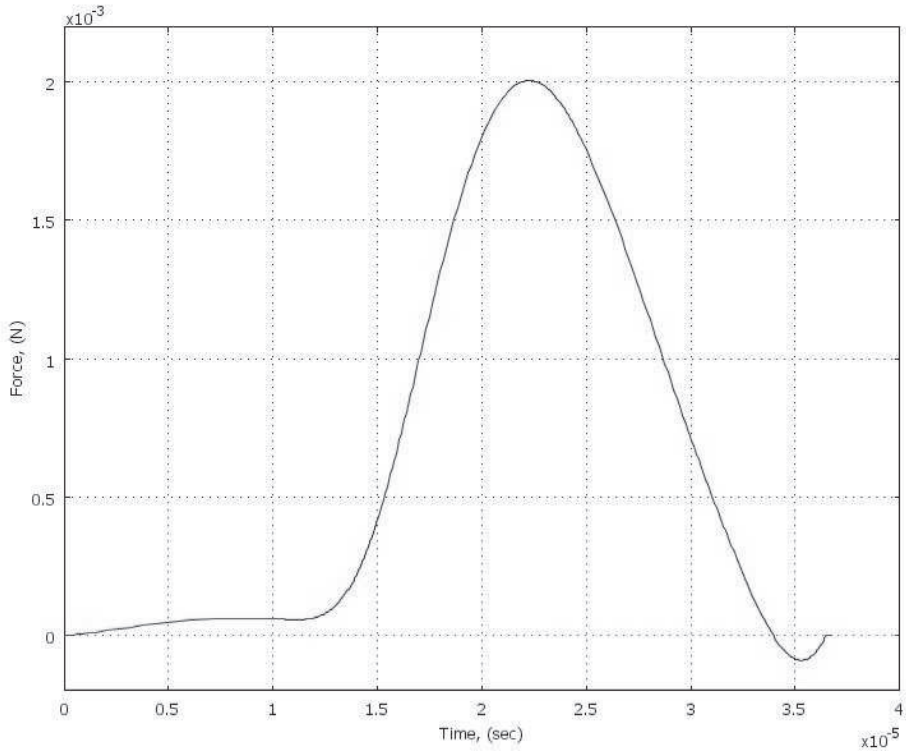


Figure 6.27: Force which is applied to the center of the die versus time, 532 nm laser incident energy is 13.32 mJ, Revalpha tape.

Temperature distribution within the silicon at highest energy level, 13.32 mJ, at different times from the beginning of the laser pulse is shown in Figure 6.28.

The effect of the tape adhesive force is still observed at the highest energy, see Figure 6.27, but it is negligible.

As can be observed from Figure 6.29, the angle theta $\theta$ reaches the value of 0.23 rad at 0.6 ms from the beginning of the laser pulse. That means that the die makes one revolution in about 16 ms and in that time the die flies about 15 mm. In the experiments with 532 nm irradiation, the observed tumbling was very stable and the direction of the flying was predictable. Intensity spatial distribution for the 532 nm laser had about 10% difference and the tumbling which was observed at this energy level: one revolution in 14 ms. The model shows an excellent match with the experiments.

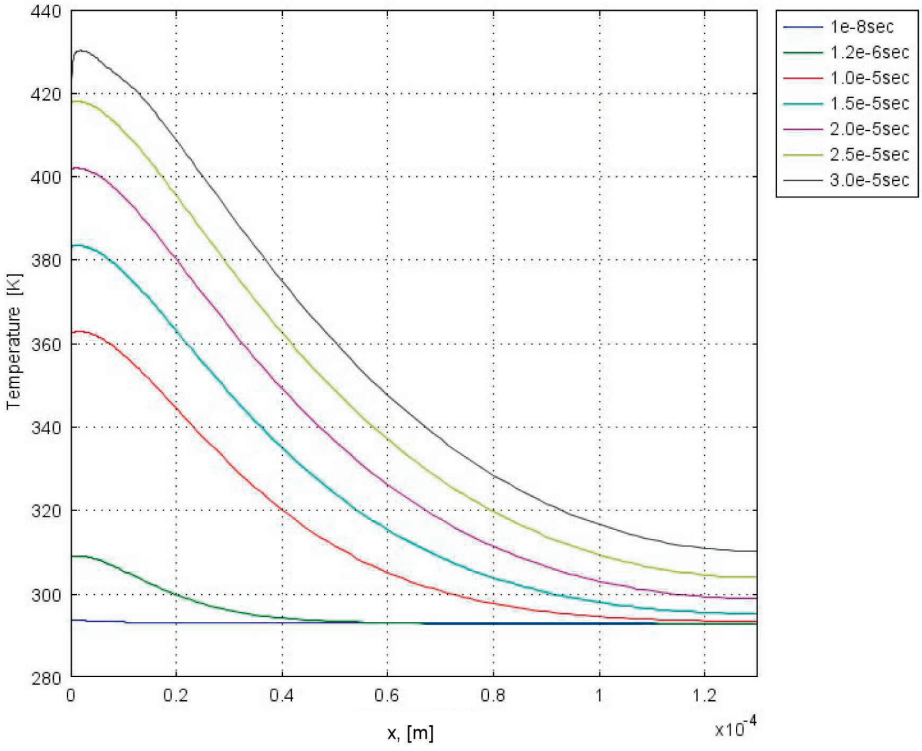


Figure 6.28: Temperature distribution within a silicon die at different times from the beginning of the 532 nm laser pulse, incident energy 13.32 mJ, Revalpha tape.

### Discussion

The analysis of the forces calculated for the thermal release using 1064 nm and 532 nm wavelengths shows that the calculated velocities differ from the experimentally observed values in case the effect of the break-off force is large: it slows down the speed at the low energy levels too much. Probably, the dependency of the break-off is more complex than it was assumed in the model. In all other respects the model shows good correlation with the experimentally observed results. The model describes and explains the process of the die release, observed energy threshold of the process, predicts the die temperature and release dynamics (including speed, acceleration, and tumbling). The model could be used to predict release acceleration for other types of lasers to ensure that the die will not be damaged physically. It can also be used to predict (and avoid) thermal damage; and last but not least, placement accuracy. Based on application with selection of the laser type, one can choose either fast but not accurate release, or slower but accurate placement of dies.

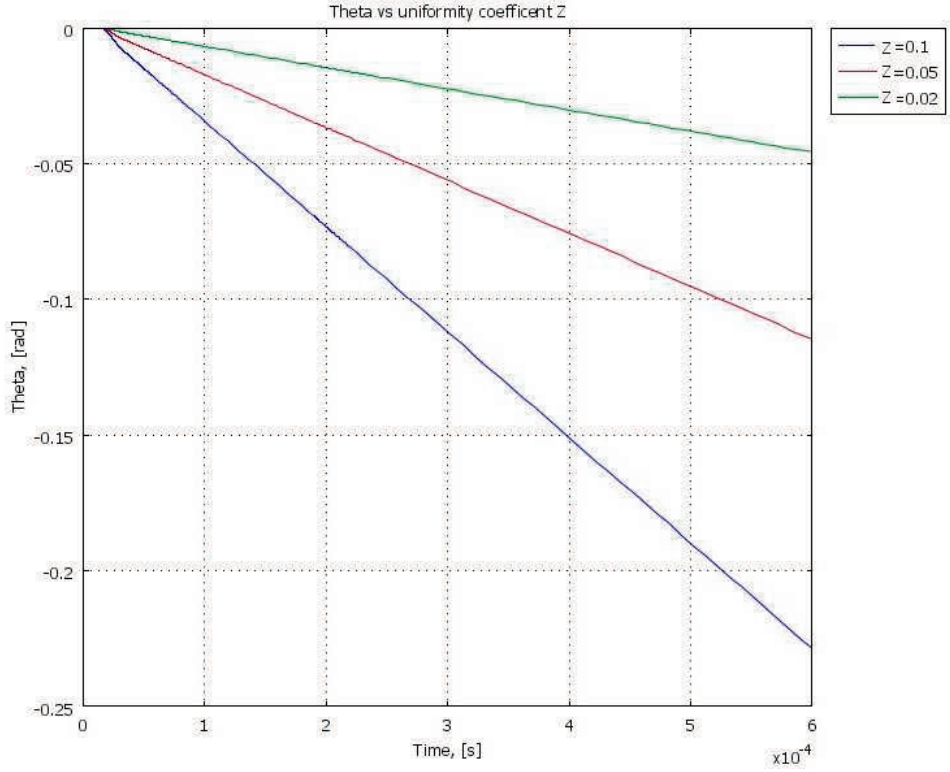


Figure 6.29: The angle $\theta$ of the die release at different coefficients $Z$, energy 13.32 mJ.

# Chapter 7

# Diffractive Optical Element

## 7.1 Introduction

In this Chapter the use of the Diffractive Optical Element to shape the laser beam and by that to reduce the effect of the intensity spikes is discussed. Both the experiments and the model simulations show that the die release process is very sensitive to the laser energy distribution at the die surface. Therefore, one of the primary challenges when scaling-up the process to industrial production rates, is to develop a beam delivery system that produces a uniform laser intensity over the die surface. There are techniques available which can increase homogeneity of the laser beam: diffractive/refractive lenslet array elements, anti-speckle rotating diffusers and Diffractive Optical Elements (DOEs). As an example, the diffractive microlens-array beam shaper was used in the experiments of the laser-driven metal flyers acceleration, [Tro01]. The roving "hot spots" which their Nd:YAG laser system had, were effectively distributed by the use of a refractive optical element. However, the intensity profile at the focal plane still had a small fraction (2%) in one peak in the center of the beam. Although the fraction was small, the effect of this spike has a deleterious effect on the flyer planarity. Their result confirms the importance of the correct design of the beam homogenizer and showes that even small fraction of the spatial intensity profile could affect the process, responsible for releasing behavior.

In the present work it was decided not to get rid of spikes but to create a special pattern on the die surface which would lead to more uniform heating of the die surface.

## 7.2 Beam shaping

The requirements for the DOE are derived from the pattern of the beams which we need to have at the die surface. For the die size of 300 $\mu$m we considered two options:

- distance between the center-to-center spots is 150 $\mu$m, beam diameter: 150 $\mu$m
- distance between spots: 100 $\mu$m and beam diameter: 100 $\mu$m.

The schematic view of the two possible die illuminations is shown in Figure 7.1.

The square-wave phase two-levels reflective grating was chosen based on calculations using special software package developed by Philips AppTech, [Kla04]. To design DOEs it is necessary to determine their surface profile, the optimal surface structure is obtained through a large amount of numerical calculation which include Fast Fourier

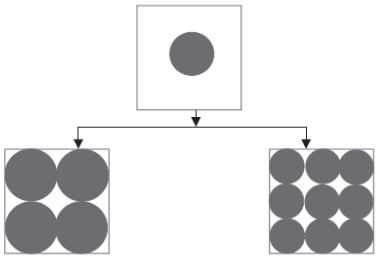

Figure 7.1:
Schematic view of the two designed illuminations of the die surface.

Transform (FFT) calculations and iterative optimization processes. Choosing different phase modulation amplitudes and checking the related power distribution on the diffracted orders for both cases: 4 and 9 diffracted beams respectively with equal power distribution were found.

The incident power is denoted by $P_0$. The distribution of the incident power over various diffraction orders was calculated for two values of the phase modulation amplitudes. In case of the classic phase grating the phase modulation amplitudes $b_x$ and $b_y$ are equal to $\pi/2$ rad. In this case 4 beams on the die area can be created. The distribution of the incident power over various diffraction orders is the following: (0,0), (-1,0), (1,0) (0,-1), and (0,1) orders are zeros. The resulting power in the first orders beams (-1,-1), (-1,1), (1,-1) and (1,1) calculated from: $P_1 = ((2/\pi)\sin(\pi/2))^4 = 0.16\ P_0$. The power in the higher orders is a factor of 1/9 smaller than the power in the first orders. Taking phase modulation amplitudes equal to 1.004 [rad] power in the orders (0,0), (-1,0), (1,0), (0,-1), (0,1), (-1,-1), (-1,1), (1,-1), and (1,1) is equal to $0.083\ P_0$, creating 9 equal beams. The power distribution over the various orders for the mentioned two cases is listed in Table 7.1.

The relation between the phase modulation amplitudes $b_x$ and $b_y$ and the height of the grating is the following $Height = (b_{x,y}/2\pi)\ \lambda$. In Table 7.2 the calculated heights and pitch for 532 nm and 1064 nm wavelengths are represented. An example of the square wave phase grating is represented in Figure 7.2.

Table 7.1: Distribution of the incident power $P_0$ over the various diffraction orders (n,m) for phase modulation amplitudes equal to 1.004 rad and 1.571 rad.

| Number of beams | $P/P_0$ m | n-1 | n0 | n1 |
|---|---|---|---|---|
| 9 | -1 | 0.08317 | 0.08317 | 0.08317 |
| | 0 | 0.08317 | 0.08317 | 0.08317 |
| | 1 | 0.08317 | 0.08317 | 0.08317 |
| 4 | -1 | 0.1643 | 0 | 0.1643 |
| | 0 | 0 | 0 | 0 |
| | 1 | 0.1643 | 0 | 0.1643 |

Table 7.2: The height of grating and Pitch for different light wavelength.

| Wavelength, nm | Number of beams | Height, nm Level 1 | Height, nm Level 2 | Pitch nm |
|---|---|---|---|---|
| 1064 | 9 | 170 | 340 | 154 |
| | 4 | 266 | 532 | 205 |
| 532 | 9 | 85 | 170 | 75 |
| | 4 | 133 | 266 | 102 |

By selecting the lens, different die sizes can be irradiated, see Table 7.3.

Table 7.3: The various die irradiated area obtained by various lenses.

| Number of spots | die size, $\mu m^2$ | f lens, mm |
|---|---|---|
| 9 spots | 300x300 | 58 |
| | 600x600 | 116 |
| | 900x900 | 174 |
| | 1200x1200 | 232 |
| 4 spots | 300x300 | 58 |
| | 600x600 | 116 |
| | 900x900 | 174 |
| | 1200x1200 | 232 |

## 7.3 Discussion

New DOE beam shaping optics, which could deliver 4 or 9 equal spots on the die surface have been designed. The advantage of applying these beams is a relatively equal irradiated die. The disadvantages of the DOEs are the following: the manufacturing of the DOE is expensive, in case of highly inhomogeneous beam the effectiveness of DOE can be limited. Furthermore, any production error will result in more power leaking into the zeroth order. Even at the best positioning and focusing the zeroth order will have slightly more power. From other side, the higher order beams do not have zero power and brings unwanted power (though a relatively small part of incident $P_0$) into the neighboring dies.

The experimental evaluation of the design was not done, because first the demonstrator with the reduced gap has to be tested. This already resulted in increased speed and accuracy, but for future designs with higher speeds the DOE would be necessary.

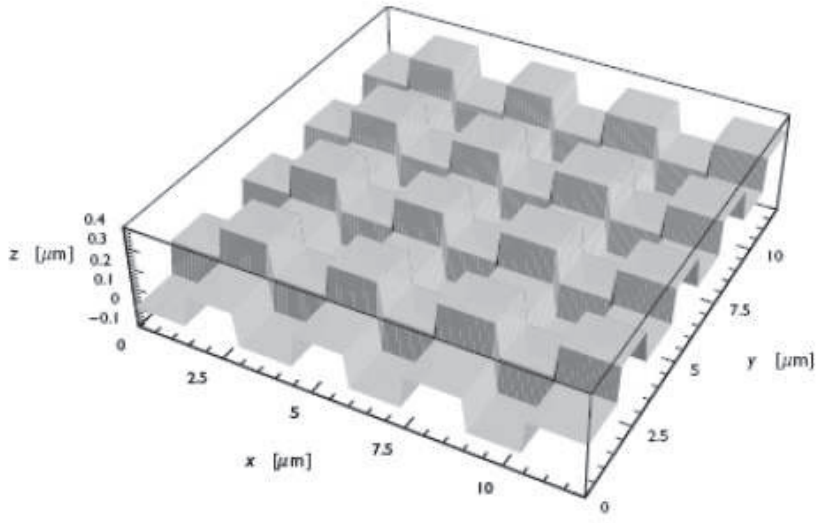


Figure 7.2:
Example of the square-wave grating.

# Chapter 8

# Demonstrator

## 8.1 Introduction

The maximum speed of assembly that can be achieved using Laser Die Transfer is more than 100 dies per second. An unsolved problem so far is the obtained positioning accuracy of the die, see Chapter 5 for details. This could be improved by using the Diffractive Optical Element. Other solutions to increase accuracy are reducing the gap to a few hundred $\mu$m or using a process such as direct die feeding. In approaches such as these, the release of dies from the film frame with the aid of metal needles could be replaced by the release with a laser, which is much faster and more reliable. The latter solution (thermal release approach) has been chosen because it can easily be implemented with existing technology.

In the following sections the result of a prototype development is presented. This work was done in collaboration with Assembléon B.V. in Veldhoven, the Netherlands, the producer of the pick-and-place machines. First, the currently used "Direct Die Feeder" (DDF) is explained. Then, the demonstrator is presented showing the feasibility of the "Laser die transfer" process in an automated environment. The main arguments for the development of a laser-based Direct Die Feeder are:

- The release of the dies from the film frame in the current DDF uses metal needles. Future trends in decreasing die thicknesses increases the risk of damaging the thin dies with the needles. Consequently, the LDT process is embraced in this design.

- The biggest wafer that can be handled in the current feeder has a diameter of 8 inch (203.2 mm), but wafers with a 12 inch (304.8 mm) diameter will become the standard in the near future.

- Transferring of flip chips within the current DDF is not optimal and risky for smaller and thinner components.

- The throughput of the current DDF is not high enough. After each six components there is a dwell time of about one and a half seconds because of design constraints.

- A design is preferred in which it is not necessary to stretch the film frame before it is inserted in the feeder. Stretching is necessary in the current feeder, where needles push the die from the tape, to prevent other dies from coming loose.

## 8.2 Surface Mount Technology and Direct Die Feeding

To date, surface mount technology (SMT) is the common production method within the electronic manufacturing industry. Using SMT, electronic components (capacitors, resistors, IC packages, etc.) are soldered directly onto connection pads on the surface of printed circuit boards (PCBs) or other substrates. SMT production consists of three steps (Figure 8.1). First, solder paste is applied to the pads on the substrate using a screen- or stencil printer. In the second step, the components are placed onto this solder paste by a pick-and-place robot. In the last step, the assembly is transported into an oven where the eutectic solder paste is reflowed, such that the actual interconnection is secured. An example is the Assembléon SMT machine that is constructed by a configurable number of parallel pick-and-place robots (varying from 5 to 20 robots).

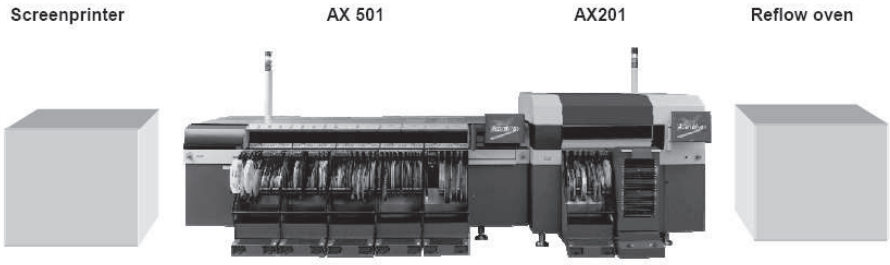


Figure 8.1: SMT process steps.

To supply dies to a pick-and-place machine one at a time, the widely applied method employs "tape and reels" or "surf tapes". These consist of a plastic strip that contains pockets at a constant pitch. These pockets are each filled with a die. The filling of these tapes requires special "wafer-to-tape equipment". A film frame is inserted in these machines and from then die is picked off and placed in one of the pockets of a tape and reel. These tape and reels are situated in so called tape feeders that supply the dies to the placement robot one at a time, see Figure 8.2.

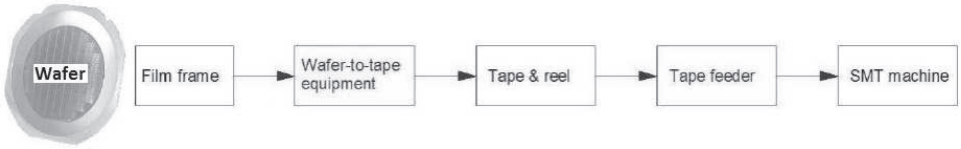


Figure 8.2: Standard process of feeding dies.

This intermediate process of transferring dies from the film frame into a tape and reel is costly. To reduce these costs a Direct Die Feeding was introduced by Hover-Davis, Rochester, USA. Instead of inserting an externally packaged tape into a feeder, a film frame is directly fed into a Direct Die Feeder (DDF) which is situated on the

placement machine eliminating the need for intermediate packaging. This also limits the risk of damage or pollution of the ICs, see Figure 8.3.

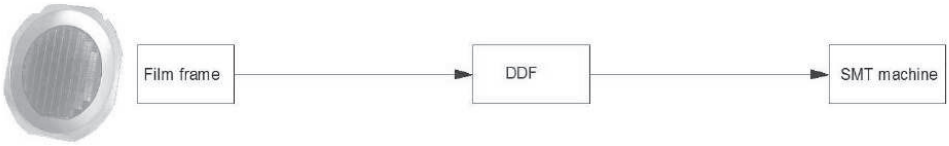


Figure 8.3: Alternative process of feeding dies

An example of a DDF such as this is shown in Figure 8.4. Here the components are extracted from the film frame and transported to the pick-and- place machine. First the film frame is stretched, which increases the distance between the dies. In order to pick a component from the film, a vacuum cup is held against the die at the back side of the tape while at the same time metal ejector pins push the die off the tape. This is done either by pushing through the tape (shown on the left in Figure 8.4) or by only pushing against the tape (shown on the right in Figure 8.4). The vacuum nozzle lifts off and transports the dies.

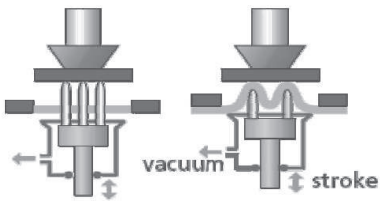


Figure 8.4: Pushing a die from the tape on to the end-effector of the pick-and-place robot.

## 8.3 Prototype 'Laser Die Transfer'

This section describes the development of a prototype to demonstrate the feasibility of the LDT process. The main goal is to automatically empty film frames and acquire an indication of the feasibility and reliability of the process. Figure 8.5 shows the upper part of the demonstrator set-up and Figure 8.6 shows the lower part. The upper part consists of a metal frame, XY-robot, optical head, optical fiber for delivering the laser irradiation, a CCD camera for alignment of the laser beam with the target die and another CCD camera for observation of the released dies, and the wafer.

The lower part of the demonstrator consists of the XY-robot and a shuttle with the vacuum nozzle as shown in Figure 8.6. The gap between the wafer and the nozzle was 0.2 mm.

### 8.3.1 Process changes for LDT

The demonstrator LDT was developed with the following constrains:

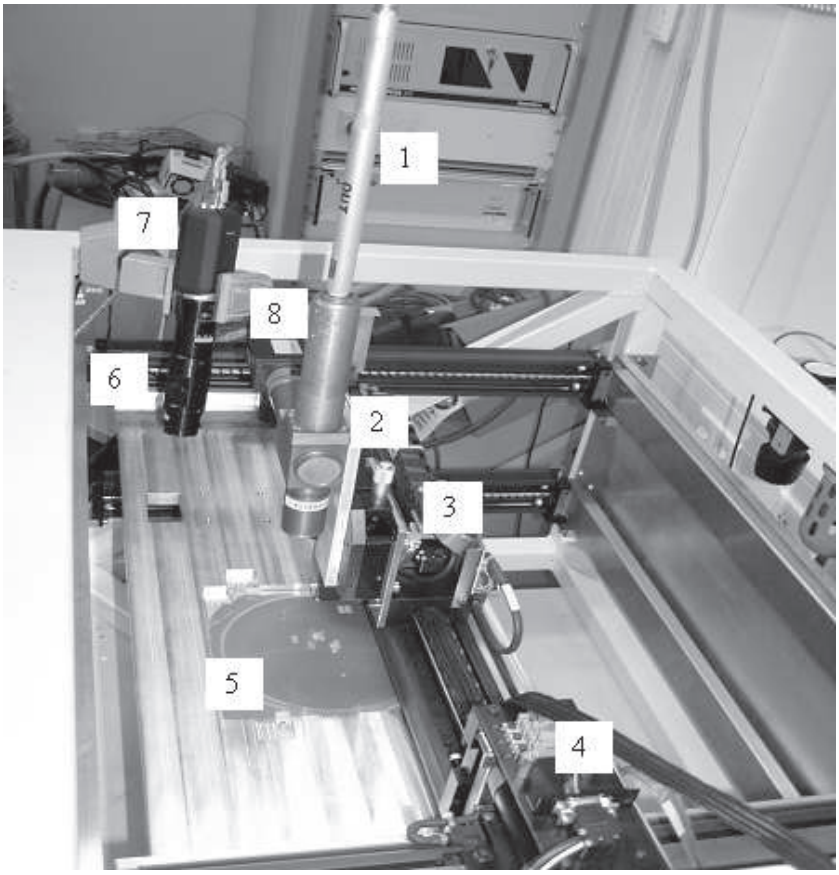


Figure 8.5: Photograph of the demonstrator LDT set-up: 1. fiber; 2. optical head; 3. X-robot; 4. Y-robot; 5. wafer; 6. zooming system; 7. camera for caught dies observation; 8. camera for laser alignment; 9. frame

- The position of the die on the nozzle is measured by a camera and is taken into account. Effects of the release process on the placement accuracy are no longer an issue.
- The research focused on one type and typically the smallest available component, namely 0.3×0.3 mm dies with a thickness of 0.15 mm. Later, the range of dies that have to be released will be extended with a maximum of 5×5 mm dies.

### 8.3.2 Description of the demonstrator

The starting point for the construction of the demonstrator is to exploit two XY-robots. The global structure of this demonstrator is determined by constructing two of these XY-robots with a film frame positioned in between (see Figure 8.7). One robot is equipped with a laser head and the other robot with a vacuum nozzle. The nozzle has an extra degree of freedom in the z-direction in order to approach the

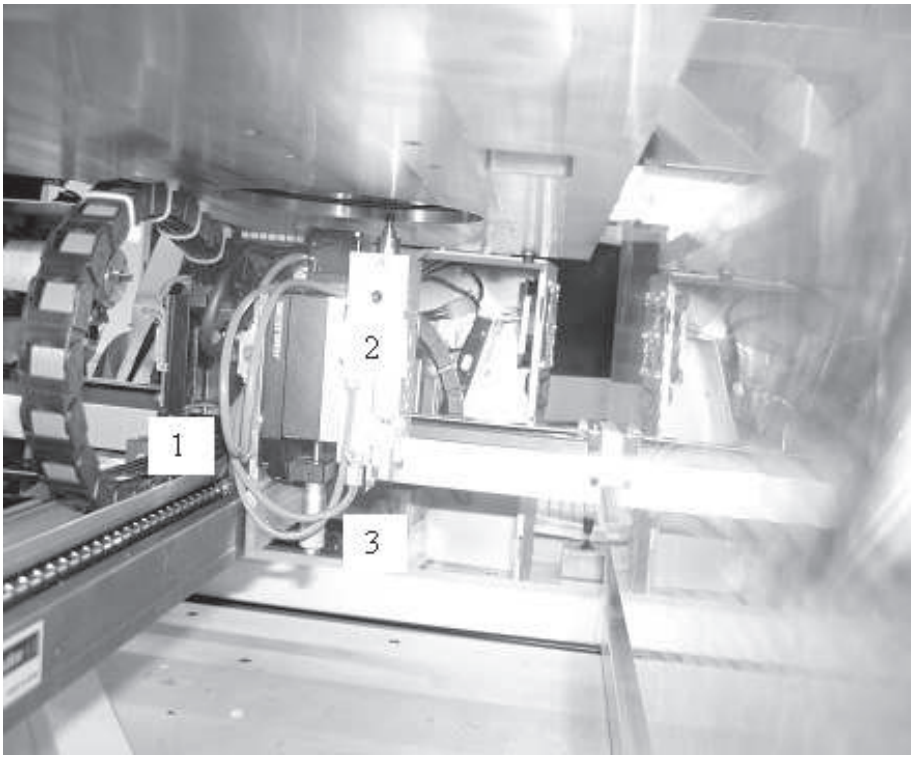


Figure 8.6: Lower part of the demonstrator: 1. X- robot; 2. micropositioner; 3. shuttle.

component that is to be released.

Furthermore, each robot is outfitted with a camera that is used to align the system. The upper camera can also be used to inspect whether or not a die was indeed caught by the nozzle.

### XY-robots

The applied robots are the same ones used for fiducial recognition of PCBs and machine calibration. These robots consist of three spindle driven linear axes. The spindles of the two parallel axes in the x-direction are coupled by a timing belt. In this way the robot is powered by two servomotors. A linear encoder is attached to each linear axis.

### Frame

A stiff frame was constructed in which the two robots were mounted. The point of departure for the total assembly is to adopt existing transport methods and instruments used for building these robots in the current pick-and-place machines. This method proceeds as follows: The robots are aligned in a special fixation tool. Fixing the robot in the tool ensures highly accurate parallelism of the two x-guides. After alignment a jig is attached to ensure that the four ends of the robot remain in position. Once the

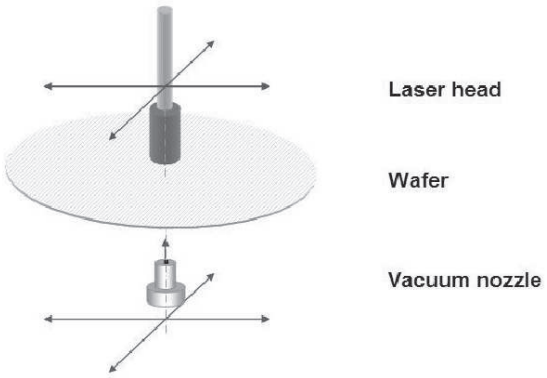


Figure 8.7: Working principle of the demonstrator.

robot is in position, its four end faces are fixed and after that the jig is removed. The main objective for the frame of this set-up is to supply a stiff connection between all eight interfacing points of the robots. The frame composed by a welded torsion-stiff structure and two plates that are attached to the inside of this structure. The combination of these plates together with the torsion stiff structure serves as a rigid frame. The robots are attached to these plates at their four interfacing faces. The robots themselves are constructed so that the robot is mounted statically determined when these four end positions are secured.

### Shuttle

The shuttle shown in Figure 8.8 is attached to the system's lower robot. Its purpose is to hold the dies that are released and transport them to the position where they are to be inspected by the camera on the upper robot. The dies are held by a vacuum nozzle ((1) in Figure 8.8). This nozzle is magnetically attached to an interface (2) for easy interchange of different nozzles. Figure 8.9 illustrates how a vacuum is generated in the nozzle.

This figure shows a cross-section of component (3) from Figure 8.8. The block contains two inlets for compressed-air ((1) and (2)). Air that is blown through the lower inlet flows through a venturi (6)that generates a vacuum in the nozzle holding the die.

Air that is blown through the upper inlet (2) is directly blown into the space indicated by (3), releasing the component from the nozzle. Elements (4) and (5) in Figure 8.9 are restrictions which adjusts the amount of air flow through the channels. The switching between the lower and upper inlet (1) and (2) (and thus between vacuum and pressure) is done by a 3/2-valve. In Figure 8.8 this valve is represented by component (6). Component (4) in Figure 8.8 is a pneumatic axis to make a z-movement in order to avoid obstacles. The switching between an up- and downward movement is done with a 5/2-valve. Component (5) in Figure 8.8 is a board alignment digital camera. This camera is used to locate the PCB in pick-and-place machines. This locating is done by recognition of local and global calibration markers or other typical artwork on the PCB. The camera is linked to a PC by IEEE1394 (Fire Wire).

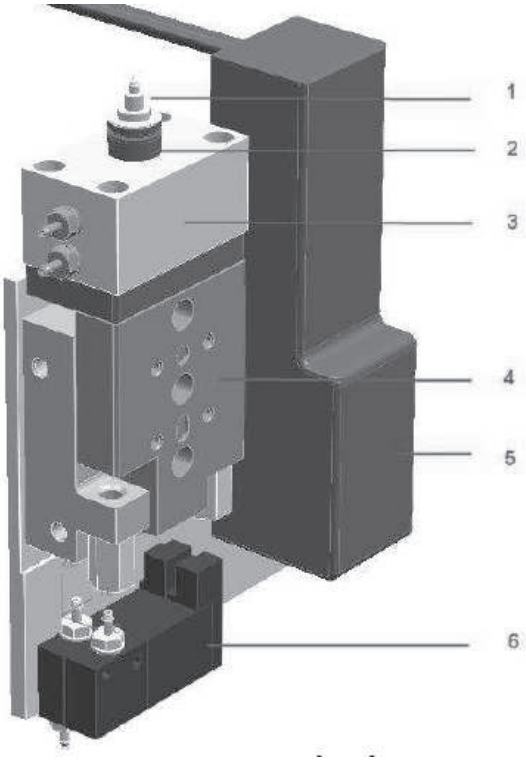


Figure 8.8: Shuttle: (1) vacuum nozzle; (2) magnetic interface; (3) vacuum generation component; (4) pneumatic axis; (5) board alignment digital camera; (6) 3/2 valve.

The camera has internal illumination which can be triggered via the same Fire Wire. In this setup the camera is used to determine the orientation of the dies on the tape and for initial alignment.

### Optical head

To release the dies from the tape, a laser fiber with optics is attached to the upper robot. This optical head is adjusted in the z-direction with a micro-stepper.

### Electronics hardware

To control the movements of the robots, standard available motion controllers were used.

### Synchronizing the robots

To position the nozzle under the laser beam, both robots are generally navigated to different encoder values. If there is a difference in the angle around the z-axis of both robots the offset between the nozzle and the laser might vary over the moving range. Therefore the robots were synchronized by a calibration plate with nine holes which was placed in the setup at the same position where the film frame is placed during

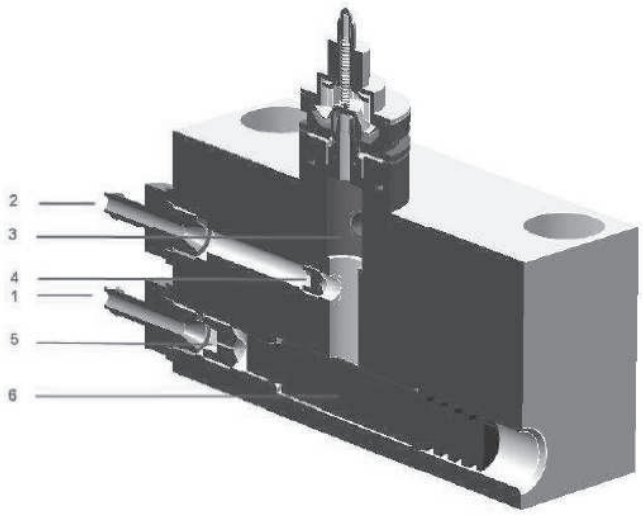


Figure 8.9: Vacuum generation: (1) and (2) are the inlets for compressed air; (3) space for the air; (4) and (5) air restrictions

operation. The holes in this plate could be detected by both upper and lower camera. In this way the camera positions on the robots could be synchronized with respect to each other. From the results it turned out that only a correction in x-direction was needed and performed. After this procedure, the offset between the nozzle and the upper camera was determined, by looking at the nozzle with the camera. The last step is to determine the offset between the laser beam and the upper camera by light sensitive paper on which a spot was created with the laser. With the camera on the upper robot the location of the spot was determined.

### Wafer alignment

The actual position and orientation of the diced wafer itself on the tape is not known. These parameters have to be determined before a tape can be emptied. They are determined with the camera on the upper robot. With this camera the coordinates of two dies at each end of the wafer are determined. Then the actual position and angle of the total diced wafer on the tape are determined. This alignment procedure is done manually. Work is in progress to also automate this procedure.

### Boundary conditions

The boundary conditions for the demonstrator were not very strict because of the following aspects:

- Firstly, for the process itself it is not very relevant whether 0.5 by 0.5 mm dies have to be released or 1 by 1 mm. The main limitations are encountered at

larger components, because there single pulse release might be a limiting factor.

- Secondly, the decision was made to use existing XY-manipulators. These robots have their own accuracy. The choice was made to use only one of the two encoders on the X-axis. Even with a single encoder still the smallest components could be released from a film frame.

Speeds and accelerations are determined by the overall electro-mechanical manipulating system and as such have no influence on the reliability of the process itself.

## 8.4 Results and conclusions

The 1064 nm thermal-induced release process was used to show the feasibility of the demonstrator. The laser source was a Nd:YAG Rofin Sinar 150P laser. Silicon dies of 1x1 $mm^2$ and 0.1 mm thickness were released with the following process settings: a laser power of 50 W, a pulse duration of 0.4 ms and a beam size of 0.8 mm. The pulse duration allows the release of up to 2 500 dies per second. (Reminder: for current pick-and-place machines this rate is 2 dies per second). This shows that the initial requirements that were formulated for the current project (100 components per second) can be easily satisfied.

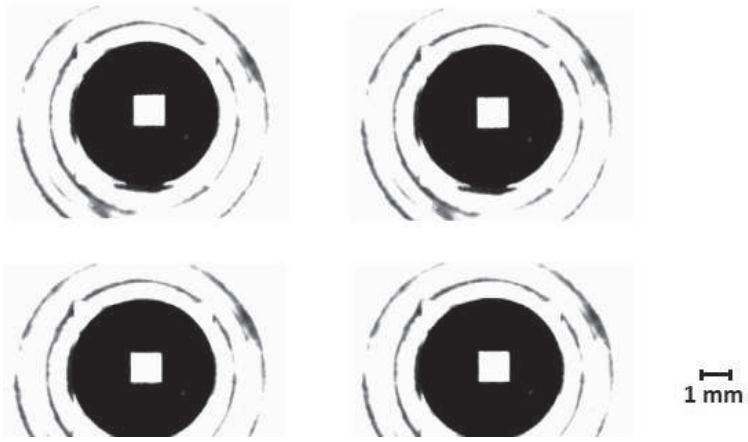


Figure 8.10: Top view of four released dies on the vacuum nozzle.

Matrixes of 10×10 components have been released. The repeatability of releasing and catching components with the nozzle was 100%. Figure 8.10 shows four dies that were consecutively released and caught by the receiving nozzle. The average placement accuracy achieved is better than 50 $\mu$m. This is more than 5 times better than the currently used requirement: placement accuracy of 25% of the dies must be within 250 $\mu$m. Therefore not only release, but also accuracy exceeds the specifications. Because of the short free fly distance of the die, tumbling was not a problem for this application. For that reason the DOE was not used. For direct transfer applications with larger free fly distances such elements have to be integrated. This was not tested so far.

The prototype proved to be quite a success that already has attracted external clients: TNO B.V. in Eindhoven, the Netherlands and NXP Semiconductors, in Nijmegen, the Netherlands (formerly Philips).

## 8.5 Recommendations and future development

The demonstrator shows that the Laser Die Transfer process is capable of releaseing and transferring thin and small components without mechanical damage and within the accuracy requirements. Further automation of the set-up is required: a coupling between the vision software and motion control software is needed. This coupling between the camera and the motion control will automatically align the wafer. Additionally, due to this coupling, the dies can be inspected automatically afterwards. Lastly, task a Graphical User Interface has to be created making overall operation easier. When these tasks are completed, a considerable number of wafers have to be emptied to obtain reliability figures relating to the process. Development of a fast

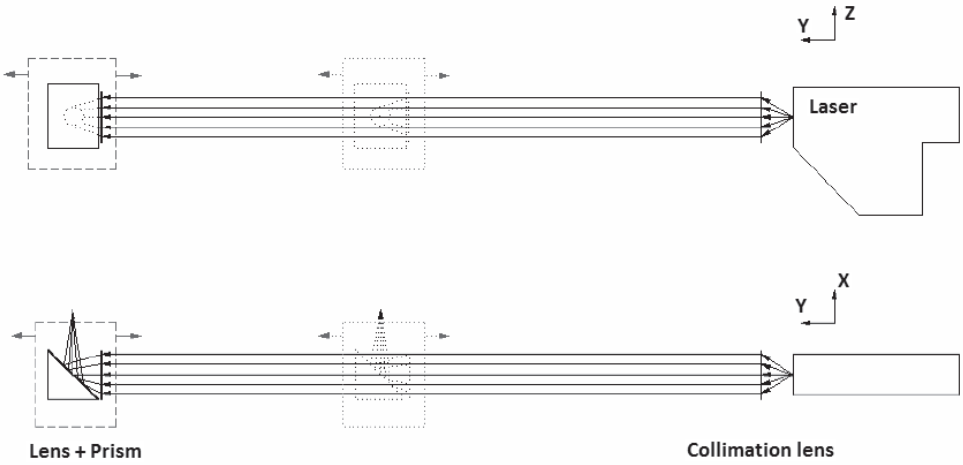


Figure 8.11: Proposal to pilot the laser spot in the y-direction.

mechanical system is needed that can support the high release speed of the LDT process.

The are two main recommendations for the future DDF design: use a more compact and less expensive laser and avoid the moving fiber in the DDF. Such lasers are available on the market but to speed up the development we applied a laser "from the shelf" in this prototype.

A solution to avoid the fiber movement is presented in Figure 8.11. Suppose that the wafer with the components is actuated in the z-direction, then the laser spot needs to be piloted in the y-direction.

The laser diode is attached to the frame of the feeder. Instead of the fiber, a collimation lens should be used delivering an almost parallel bundle that is intercepted by a combination of a focusing lens and a 90 degree mirror or prism. This combination ensures that the parallel bundle, which is directed in the y-direction, is focused on

a die in the x-direction. With this concept, only one optical component has to be moved in the y-direction.

# Chapter 9

# Conclusions

The main benefits of the Laser Die Transfer process are the high assembly speed and the ability to handle small and thin components. In summary, we have demonstrated a new assembly technique using laser-induced transferring.

The efficiency of the laser-induced release process in energy terms is relatively low for all studied release approaches. First, ablative release using highly intense IR laser pulses resulted in a high-speed but unstable release dynamic leading to low placement accuracy. This effect became more pronounced at higher fluence levels. The process takes places at high temperatures (near the evaporation temperature of the silicon). The thermal damage of the irradiated die proved to have only "cosmetic" effect since the opposite side, where the active scheme is situated, does not overheat. Q-switched lasers usually give a first pulse with higher energy than the following pulses, even with first pulse suppression optimization. This resulted in the different release of the first components and their overheating. All problems could be solved except for the high die velocity, which complicates the assembly process.

The lower velocity thermal release approach makes the process more controllable. However, the achieved placement accuracy (50 micrometers) was not enough for standard assembly. Experimental results show that the placement accuracy largely depends on laser pulse duration. Furthermore, for shorter pulses better placement accuracy is obtained with infrared and green thermal release approaches. Another factor responsible for smooth releasing is the spatial profile of the laser spot. Also the nonlinear absorption process in the silicon under low intensity infrared laser irradiation could be considered a cause for problems with process stability. A strongly improved component flying dynamics was achieved using a frequency doubled Nd:YAG laser, with low intensity pulses. The nonlinearity of absorption with this approach is decreased due to the much higher, hence localized, absorption in silicon. This approach with the green laser wavelength was proved to be the best for safe and stable release of the components.

Simulation models are developed for both approaches that describe major features of the system's response: the light absorption, time evolution of the temperature distribution in a three-layer structure irradiated with a laser beam, and how the absorbed energy is transformed into kinetic energy of the die. These models show how different phenomena influence the process. They also give the process limitations.

As was shown, the major factor responsible for improving the release behavior is the better quality of the laser spot, without local peaks causing "hot spots". It is quite difficult to overcome these peaks. A Diffractive Optical Element as designed in this research will create a balanced pattern of the laser irradiation on the die surface, which will improve the release.

The objective of this work was to investigate the laser-induced die transfer technique as a possible application for the assembly of microcomponents. The developed

process can already be applied in different fields of the microelectronics industry.

# Summary

A key feature of semiconductor manufacturing over the past 30 years has been its ability to produce very small chips, the current state-of-the-art in production being around 0.25 mm in size. Conventional assembly is based on the handling of individual components by pick-and-place robots. This technology is unsuitable for many microsystems due to the difficulty of handling small (less than 1 millimeter) and thin (less than 100 micrometers) components and of scaling up these techniques for mass production.

Thus, micro-assembly of miniature electronics demands processes that are able to accurately handle components with dimensions of several tens of micrometers with high assembly rates onto a broad range of substrates. Nowadays, three ways of solving this problem are under investigation:

- Development of new processes based on mechanical handling of the micro-components;
- Improvement of the conventional pick-and-place equipment;
- Development of laser-induced transferring processes.

This work presents a study on a new technique based on the laser-induced release of the micro-component from its carrier, its transfer towards the interconnecting substrate and its landing.

This technique provides a very high assembly speed of over 100 components per second, compared to 2 components per second using the conventional pick-and-place method. In some specific areas, this approach can already be applied.

This work summarizes the experimental study of the component detachment process, release dynamics and placement accuracy for different laser sources and process parameters. Examples are given to show the possibility of controlling and manipulating the kinetic and dynamic behavior of the released component. Major attention is paid to factors responsible for the placement accuracy. Important issues presented are: the role of the spatial intensity profile of the laser beam and possibilities to improve its homogeneity, control of the component's release speed and heating up of the components by the laser pulse.

One of the applications to which the Laser Die Transfer process is ready to be applied

is the touchless release of thin components from the carrier tape. Based on the experimental results and theoretical insight gained in the current research, a demonstrator was built and successfully tested.

# Samenvatting

Eén van de belangrijkste eigenschappen van de halfgeleider productie gedurende de afgelopen 30 jaar is de mogelijkheid tot het produceren van zeer kleine chips, ongeveer 0.25mm tegenwoordig met de meest geavanceerde technologieën. Conventionele assemblage is gebaseerd op het verwerken van individuele componenten met pick-and-place robots. Deze technologie is echter ongeschikt voor veel microsystemen vanwege de problemen met het hanteren van kleine (kleiner dan 1 millimeter) en dun-ne (dunner dan 100 micrometer) componenten en problemen in het opschalen van de-ze technieken voor massaproductie.

Microassemblage van miniatuur elektronica vereist daarom processen die in staat zijn om componenten met afmetingen van enkele tientallen micrometers nauwkeurig te plaatsen met hoge assemblagesnelheden op een verscheidenheid aan substraten. Op dit moment worden er drie methoden onderzocht om dit probleem op te lossen:

- Ontwikkeling van nieuwe processen gebaseerd op mechanische plaatsing van micro componenten,
- Verbetering van conventionele pick-and-place apparatuur,
- Ontwikkeling van lasergebaseerde plaatsingsprocessen.

In dit proefschrift wordt het onderzoek naar een nieuwe techniek gebaseerd op lasergeïnduceerde verwijdering van een component van zijn drager, de overdracht naar het substraat en de landing daarop gepresenteerd.

Deze techniek levert een zeer hoge assemblage snelheid, tot 100 componenten per se-conde, vergeleken met 2 componenten per seconde voor conventionele pick-and-place methoden. In enkele specifieke toepassingen kan deze techniek nu al toegepast wor-den.

Dit boek geeft een samenvatting van de experimentele studie naar het proces van het overdragen van de component, het dynamisch gedrag en de plaatsingsnauwkeurigheid voor verschillende laser bronnen en procesparameters. Voorbeelden laten de mogelijkheden om het kinetische en dynamische gedrag van de over te dragen component te beïnvloeden zien. Speciale aandacht wordt geschonken aan de factoren die verantwoordelijk zijn voor de plaatsingsnauwkeurigheid. Belangrijke punten die worden gepresenteerd zijn: de rol van het bundelprofiel van de laser en de mogelijkheden om de homogeniteit hiervan te verbeteren, het beheersen van de snelheid van de component bij de overdracht en verhitting van de component door de laserpuls.

Eén van de applicaties waarvoor het Laser Die Transfer proces voldoende is ontwikkeld om te worden toegepast is het contactloos losmaken van dunne componenten van een dragertape. Gebaseerd op de experimentele resultaten van het huidige onderzoek is er een demonstratie opstelling gebouwd en getest.

# Bibliography


[All95] M. von Allmen, *Laser-beam interactions with materials*, 2nd edition, Springer, 1995.

[Arn04] M. Arneson, "Pica - low-cost, high-volume rfid tag production", *White Paper*, vol. www.matrics.com, 2004.

[Asa90] J. R. Asay, T. G. Trucano and R. S. Hawke, "The use of hypervelocity launchers to explore previously inaccessible states of matter", *International Journal of Impact Engineering*, vol. 10, no. 1-4, pp. 51–66, 1990.

[Boh86] J. Bohandy, B. Kim and F. Adrian, "Metal deposition from a supported metal film using an excimer laser.", *J. Appl. Phys.*, vol. 60, no. 4, pp. 1538–9, 1986.

[Boh98] K. Bohringer, K. Goldberg, M. Cohn, R. Howe and A. Pisano, "Parallel microassembly with electrostatic force fields", *IEEE International Conference on Robotics and Automation (ICRA)*, pp. 1204–1211, 1998.

[Can80] C. Cantor and P. Schimmel, *Biophysicac Chemistry: Part 3: The behaviour of biological macromolecules*, San Francisco: W.H. Freeman, 1980.

[Chr94] D. Chrisey and G. H. (Eds.), *Pulsed laser deposition of thin films*, Wiley Interscience New York, 1994.

[Coh91] M. Cohn, C. Kim and A. Pisano, "Self-assembling electrical networks: an application of micromachining technology", *Transducers'91 International Conference on Solid-State Sensors and Actuators, Diget of Technical Papers,*, pp. 490–493, 1991.

[Coh94] M. Cohn, "Method and apparatus for the assembly of microfabricated devices", *US Patent nr. 5 355 577*, 1994.

[Coh98] M. Cohn, K. Bohringer and J. Nowoeolski, "Microassembly technologies for mems", *Proc. SPIE Microfluid. Devices Conf*, vol. 3515, pp. 2–16, 1998.

[Dan97] G. Danuser, I. Pappas and B. Vgeli, "Manipulation of microscopic objects with nanometer precision: potentials and limitations in nano-robot design", *International Journal of Robotics Research*, 1997.

[Den08] N. Denko, *http://www.nitto.com/*, 2008.

[Dre79] R. Drew, F. Schmidt and T. J. Vanduynhoven, "Laser deposition of metal upon transparent materials, patent.", *T988007*, vol. IMB, 1979.

[Eas07] R. Eason, *Pulsed laser deposition of thin films: applications-led growth of functional materials*, John Wiley and Sons Inc., Hoboken, New Jersey, 2007.

[Ern03] H. Erne, "Microassembly automation: what are the critical success factors?", *Proceedings of the international precision assembly seminar, Bad Hofgastein, Austria, March 2003*, , no. ISBN 0-85358-117-7, 2003.

[Fea95] R. Fearing, "Survey of sticking effects for micro parts handling", *IEEE/RSJ Int. Conf. on Intelligent Robots and Systems,*, vol. 2, pp. 212–217, 1995.

[Gre04] M. Greenaway and J. Field, "The development of a laser-driven flyer system", *Proceedings of the conference of the American Physical Society topical group on Shock Compression of Condensed Matter*, vol. 706, pp. 1389–1392, 2004.

[Hol98] A. Holmes and S. Saidam, "Sacrificial layer process with laser-driven release for batch assembly operations", *Microelectromechanical Systems, Journal of*, vol. 7, no. 4, pp. 416–422, 1998.

[Jac02] H. Jacobs, A. Tao, A. Schwartz and D. Gracias, "Fabrication of a cylindrical display by patterned assembly", *Science*, vol. 296, pp. 323–325, 2002.

[Jel84] G. Jellison, *Semiconductors and Semimetals*, Academic Press New York, 1984.

[JFG02] B. R. J. Fitz-Gerald, P. D. Rack and H.D.Wu, *Matrix Assisted Pulsed Laser Evaporation-Direct Method to Rapidly Prototype Organic and Inorganic Materials*, Academic Press a Division of Harcourt Inc., 2002.

[Kan72] A. Kantrowitz, "Propulsion to orbit by ground based lasers", *Astronautics and Aeronautics*, vol. 10, no. 5, pp. 74–76, 1972.

[Kat04] H. Katsurayama, M. Ushio and K. Komurasaki, "Analytical study on flight performance of an air-breathing rp laser launcher", *AIAA/ASME/SAE/ASEE Joint Propulsion Conference and Exhibit, 40th, Florida*, vol. AIAA 2004-3585, 2004.

[Kla04] R. Klaver, "Grating", *CTB 55604, Philips internal document*, pp. 51–62, 2004.

[Kom02] K. Komurasaki, Y. Arakawa, S. Hosoda, H. Katsurayama and K. Mori, "Fundamental researches on laser powered propulsion", *33rd Plasmadynamics and Lasers Conference, Maui, Hawaii*, vol. AIAA-2002-2200, 2002.

[Lan04] C. Landesberger, *Innovative fertigungsverfahren fur neue produkte auf der basis dunner silizium-bauelemente (InnoSi)*, Fraunhofer IRB Verlag, 2004.

[Lie82] A. Lietoila and J. Gibbons, *J. Appl. Phys. Rev.*, vol. 53, pp. 3207–3213, 1982.

[Log91] Logman, *Logman Dictionary of the English Language*, 2nd edition ed., Logman Group UK Limited, 1991.

[Mat06] S. Mathews, R. Auyeung and A. Pique, "Use of laser direct-write in microelectronics assembly", *Online proceedings of the 4th international congress of laser advanced material processing*, vol. http://www.jlps.gr.jp/en/proc/lamp/06/, 2006.

[Mea98] J. Mead, L. Myrabo and D. Messitt, "Flight and ground tests of a laser-boosted vehicle", *AIAA/ASME/SAE/ASEE Joint Propulsion Conference and Exhibit, 34th, Cleveland,*, vol. AIAA 983735, 1998.

[Myr98] L. Myrabo, D. Messitt and F. Mead, "Ground and flight tests of a laser propelled vehicle", *Aerospace Sciences Meeting and Exhibit, 36th, Reno, Nevada*, vol. AIAA 981001, 1998.

[Pai91] D. Paisley, R. Warnes and R. Kopp, "Laser-driven flat plate impacts to 100 gpa with sub-nanosecond pulse duration and resolution for material property studies", *American Physical Society Conference on Shock Compression of Condensed Matter, Williamsburg, 1991*, pp. 17–20, 1991.

[Phi88] C. R. Phipps, T. P. Harrison and R. F. York, "Impulse coupling to targets in vacuum by krf and co2 single-pulse lasers", *Journal of Applied Physics*, vol. 64, pp. 1083–1096, 1988.

[Piq02] A. Piqué and D. Chrisey, *Direct-write technologies for rapid prototyping applications*, Academic Press, 2002.

[Pir72] A. Pirri, D. Northam and R. Schlier, "Momentum transfer and plasma formation above a surface with a high-power $co_2$ laser", *Applied Physics Letters*, vol. 21, pp. 79–81, 1972.

[Qua96] A. Quaid and R. Hollis, "Cooperative 2-dof robots for precision assembly", *IEEE Int. Conf. on Robotics and Automation*, vol. 3, pp. 2188–2193, 1996.

[Roy95] R. Roybal, C. Sterin, C. Miglionico and J. Shively, "Laboratory simulation of hypervelocity debris", *International Journal of Impact Engineering*, vol. 17, no. 4-6, pp. 707–718, 1995.

[Sch05] A. Schoonderbeek, *Laser drilling of metals with a XeCl excimer laser*, isbn 90-365-2126-2 ed., Printed by Print Partners Ipskamp, Enschede, 2005.

[SM07] K. M. S.A. Mathews, N.A. Charipar and A. Piqué, "Manufacturing microelectronics using lase-and-place", *Photonics Specta*, vol. 41, no. 10, pp. 70–74, 2007.

[Smi98] J. Smith and H. Yeh, US Patent 5 824 186, 1998.

[Sri01] U. Srinivasan, R. T. Howe and D. Liepmann, "Microstructure to substrate self-assembly using capillary forces", *Microelectromechanical Systems, Journal of*, vol. 10, no. 1, pp. 17–24, 2001.

[Sva79] K. Svantesson, "Determination of the temperature dependence of the free carrier and interband absorption in silicon at 1.06 $\mu$m", *J. Phys. C: Solid State Phys*, , no. 12, pp. 3837–38, 1979.

[Tro89] W. Trott and K. Meek, "Acceleration of thin foil targets using fiber-coupled optical pulses", *Meeting Abstracts*, pp. 14–17, 1989.

[Tro92] W. Trott, "Studies of laser-driven flyer acceleration using fibre optic coupling", *Shock Compression of Condenced Matter*, pp. 829–832, 1992.

[Tro96] W. Trott, "High-speed optical studies of the driving plasma in laser acceleration of flyer plates", *Proceedings of the conference of the American Physical Society topical group on shock compression of condensed matter*, vol. 370, pp. 921–924, 1996.

[Tro01] W. Trott, R. Setchell, J. Castaneda and D. Berry, "Evaluation of a diffractive, microlens-assay beam shaper for use in acceleration of laser-friven flyers", *Proc. of SPIE*, vol. 4443, pp. 166–177, 2001.

[Ugl81] A. Uglov, *Physics and Chemistry*, , no. 4, p. 29, 1981.

[Usa99] M. Usami, "Thin silicon chips and acf connection technology for contactless ic cards", *Proceedings of IMAPS 32nd International Symposium on Microelectronics*, pp. 309–312, 1999.

[Usa04] M. Usami, "An ultra-small rfid chip: mu-chip", *IEEE Radiofrequency Integrated Circuits Symposium*, pp. 241–244, 2004.

[Wat00] S. Watson, M. J. Gifford and J. E. Field, "The initiation of fine grain pentaerythritol tetranitrate by laser-driven flyer plates", *Journal of Applied Physics*, vol. 88, no. 1, pp. 65–69, 2000.

[Yeh94] H. Yeh and J. S. Smith, "Fluidic self-assembly for the integration of gaas light-emitting diodes on si substrates", *IEEE Photonics Technology Letters*, vol. 6, pp. 706–708, 1994.

[Yoo00] J. Yoo, S. Jeong, R. Greif and R. Russo, "Explosive change in crater properties during high power nanosecond laser ablation of silicon", *Journal of Applied Physics*, vol. 88, no. 3, pp. 1638–1649, 2000.

[Zha04] N. Zhang, Y. Zhao and X. Zhu, "Light propulsion of microbeads with femtosecond laser pulses", *Optics Express*, vol. 12, no. 15, pp. 3590–3598, 2004.

[Zhe06] W. Zheng and H. Jacobs, "Self-assembly process to integrate and connect semiconductor dies on surface with songle-angular orientation and contact-pad registration", *Advanced Materials*, , no. 18, pp. 1387–1392, 2006.

# About the Author

Natallia Karlitskaya was born on December 24, 1975 in Orscha, in the Soviet Union (now Republic of Belarus). She received her secondary education at the Lyceum of the Belarusian State University (Minsk, Belarus) and graduated in 1993. From 1993 onwards, she studied at the Belarusian State University (Minsk, Belarus) at the Radiophysics and Electronics department and she received her Master's degree in 1998. In 1997 she started an additional study of Economical Cybernetics (mathematical methods in economics), which she completed in 1998. In April 2003 she became a PhD student under the supervision of prof. dr. ir. J. Meijer at the University of Twente, Faculty of Engineering Technology, Chair of Applied Laser Technology in Enschede, the Netherlands. In her research she investigated the laser-based technique named "Laser Die Transfer" in an industry environment, at Philips Applied Technologies (Apptech), Eindhoven, the Netherlands. In 2007 she started working as a Design Engineer at ASML B.V., Veldhoven, the Netherlands, a position she currently still holds.